Winter 2006

Femtosecond Laser Ablation with Single and Two-Photon Excitation for MEMS

Mohamed Abdelfattah Kottb Ahmad Elbandrawy
Old Dominion University

FEMTOSECOND LASER ABLATION WITH SINGLE AND TWO-PHOTON EXCITATION FOR MEMS

by

MOHAMED ABDELFATTAH KOTTB AHMAD ELBANDRAWY
B.Sc. May 1991, Cairo University, Egypt
M.Sc. March 1997, Cairo University, Egypt

A Dissertation Submitted to the Faculty of
Old Dominion University in Partial Fulfillment of the
Requirement for the Degree of

DOCTOR OF PHILOSOPHY

ELECTRICAL ENGINEERING

OLD DOMINION UNIVERSITY
December 2006

Approved by:

Amin Dharamsi (Director)

Aleksey Bugayev (Member)

Linda L. Vahala (Member)

Michael J. Kelley (Member)

ABSTRACT

FEMTOSECOND LASER ABLATION WITH SINGLE AND TWO-PHOTON EXCITATION FOR MEMS

Mohamed Abdelfattah Kottb Ahmad Elbandrawy
Old Dominion University, 2006
Director: Dr. Amin Dharamsi

There is an increasing interest in femtosecond laser micromachining of materials because of the femtosecond laser's unique high peak power, ultrashort pulse width, negligible heat conductivity process during the laser pulse, and the minimal heat affected zone, which is in the same order of magnitude of the ablated submicron spot. There are some obstacles in reaching optimal and reliable micromachining parameters. One of these obstacles is the lack of understanding of the nature of the interaction and related physical processes. These processes include amorphization, melting, re-crystallization, nucleated-vaporization, and ablation.

The focus of this Dissertation was to study the laser-matter interaction with single and two-photon excitation for optical micro-electro-mechanical system (OMEMS) applications. The laser pulse interaction mechanism was studied by performing a series of experiments including self-imaging experiments, two-photon absorption measurements, and micromachining processes characterizations.

As a result of the self-imaging experiment, it was found for both Si and GaP that the material surface reflectivity increased twice as much during the action of the laser pulse. The generation of electron-hole plasma of $10^{22}cm^{-3}$ density was assigned to be responsible for the reflectivity jump. The Drude damping time of the generated plasma

was determined to be 0.35 fs for silicon and 0.27 fs for gallium phosphate.

Additionally, a precise measurement of the two-photon absorption (TPA) coefficient (β) was done. The TPA coefficient was found to be 0.2 cm/GW. Experimental results were in good agreement with the theoretical expectations up to a point at which the ablation started kicking off and the plasma absorption took place.

In case of a single pulse interaction with silicon, self-assembled nano-filaments of a few tens of microns' length and about 100 *nm* width were observed for the first time with the femtosecond single pulse interaction. The filaments were characterized using atomic force microscopy (AFM) and scanning electron microscopy (SEM).

Femtosecond micromachining parameters of silicon were then characterized. The laser beam was first cleaned up using two optical techniques: spatial filtering and expanding. Both cleaning-up techniques gave a clean beam profile; however, with spatial filtering, it was hard to maintain the laser beam quality for a long time as the pinhole in the telescope was destroyed in a matter of hours, so the second technique was used instead.

One- and two-dimensional amplitude gratings were written on the Si surface using the characterized micromachining parameters.

The properties of one-dimensional machined grating depended on laser polarization orientation with respect to laser scanning direction and pulse energy. 1-D diffraction patterns were obtained from parallel machined samples, while 2-D diffraction patterns were obtained from a perpendicular machined sample at laser energy density < 0.6 J/cm^2.

The 2-D diffraction patterns resulted from secondary periodical ripples along the

polarization direction. During parallel writing directions, these ripples smoothed out; in perpendicular directions, they remained and gave rise to 2-D diffraction pattern. These ripples had large periods (3-5 microns) and were perpendicular to the small periods that have been reported.

The investigations presented in this Dissertation increase the understanding of the ablation mechanism under a single laser pulse, the semiconductor materials' behavior on the femtosecond time scale, and the associated self-assemble structure process. The feasibility of short-pulse laser micromachining of semiconductor materials for the micro-electro-mechanical systems (MEMS) was also shown along with the process characterization, which provided guidelines that could help in explaining and advancing the currently existing laser materials processes.

THIS DISSERTATION IS DEDICATED TO MY FATHER, MY MOTHER,

AND MY LOVING WIFE AND LOVELY SONS, OMAR AND SUHAIB

ACKNOWLEDGMENTS

I would like to sincerely thank all of those who contributed to the completion of this Dissertation. A special thanks for Dr. Mool C. Gupta for his guidance, direction, and support in good and bad times and for his invaluable research ideas.

I would like also to thank my academic advisor, Dr. Amin Dharamsi for his support, fruitful and stimulating discussions and for all of his effort in reviewing and commenting on this Dissertation. Special thanks goes to my research advisor, Dr. Aleksey Bugayev for his scientific thoughts, constructive ideas, for his tremendous support.

I would like to thank Dr. Hani Elsayed Ali for his support, beneficial discussions and invaluable comments. I would like to thank my committee members Dr. Linda Vahala and Dr. Mike Kelly for their time, and support.

I sincerely thank my father and mother for their substantial priceless support and prayers. I gratefully acknowledge that I owe them all of my accomplishments. I cannot thank them enough for all what they did for me. Thanks Omar and Suhaib, my lovely sons, who kept me smiling when I strongly needed to change my mood.

Finally I would like to express my deepest thanks and appreciation for my lovely wife for all of her tremendous effort, and support for the sake of the completion of this Dissertation. I also thank her for the most important and appreciated role she played as a weekday single mother when I was busy doing my research.

I would like to thank Kim Kindrew from Jefferson Lab. Information Center for her help in proofreading this Dissertation.

TABLE OF CONTENTS

LIST OF FIGURES

CHAPTER 1

OBJECTIVES

The objectives of this Dissertation were to study laser micromachining processes for micro-electro-mechanical systems, especially as they relate to single and multiple pulses ablation of semiconductors. More specifically, this Dissertation was to develop a better understanding of the phenomena involved in the laser ablation processes, than what is currently available. This development was to include the investigation of the ablation mechanism associated with single and two-photon excitation processes using an ultrafast self-imaging technique, to characterize the two-photon interaction process and to determine the two-photon absorption coefficient of gallium phosphate material, and finally, to utilize the gained information in characterizing the laser micromachining process for optical micro-electro-mechanical systems and then fabricate and test a simple OMEMS device.

CHAPTER 2

INTRODUCTION

Since it was invented, lasers in general and ultrashort lasers in particular have become increasingly more interesting because of their unique properties compared with more conventional machining tools. Femtosecond lasers have been widely used in processing different materials, such as metals [1-7], polymers [8-11], semiconductors [2, 12-15], ultrahard materials [16-18], and transparent materials [6, 19] for various applications.

In section 2.1, an overview of the ultrashort laser pulse ablation challenges is presented. Then, section 2.2 is devoted to discussing the methodology followed in this Dissertation. Finally, in section 2.3, the Dissertation organization is presented.

2.1. OVERVIEW

Laser material processing is a wide field that can be categorized according to the material properties (electrical or mechanical) or according to the used laser beam. As for the target material, almost all materials, metals to insulators, hard to soft tissue, organic to non-organic, can be machined using ultrashort pulses. Lasers as micromachining tools can be also categorized according to power, wavelength or pulse width. However, the investigations contained in this Dissertation were devoted to the interaction of material with ultrashort pulse lasers.

The mechanisms and the main factors governing the laser processing remain controversial and need further theoretical and experimental studies in order to describe

the thermal field, thermal-mechanical stress and deformation, fluid dynamics of the molten material, plasma shielding, and thermal prehistory of the processing. The complexity of the problem is mainly due to the different contributions and the significance of the above mentioned processes and depend on the external parameters like pulse duration, pulse energy, and pulse repetition rate. The most important parameters are the ratios of pulse duration to the carrier's cooling time and to the lattice heating time, which determine different mechanisms involved in light-matter interaction. This difference manifests itself with increasing accuracy in laser micromachining when the pulse duration changes from nanosecond to femtosecond time region.

For a single nanosecond laser pulse interaction with matter, a number of theories were proposed to explain laser ablation process. A simple one-dimensional model was developed based on the theory that the material exposed to the laser beam is removed via evaporation [20]. The alternative mechanism for material removal suggested that surface evaporation in the area exposed to laser irradiance induced recoil pressure [21], which ejects molten material. A more sophisticated model included accurate calculation of the melt front dynamics, which was usually treated in terms of the 'problem of Stefan' [22]. This model was based on the assumption that no melt motion occurs. The assumption seemed to be valid if the intensity of laser pulse was sufficiently high so that the material evaporated faster than it moved, and/or the interaction time was short enough that noticeable melt displacement could not occur. In addition to thermal consideration, it was also suggested that laser-induced plasma could significantly affect the absorption of laser pulse energy. A fundamental plasma-based model for the laser energy transfer was proposed in which the dominant energy transport process was found to be the release of

kinetic and ionization energy of charged particles being absorbed and then recombining at the wall [23].

As for femtosecond laser pulses which produced high and accurate micromachining, theoretical and experimental investigations of the ablation process were still in progress [24-35]. The main difficulties resulted from the need for the electron kinetic theory to be employed to account for the electron-phonon interaction, since the Fourier theory was no longer accurate due to omission of high-order terms in the presentation of temperature gradient. Nevertheless, the two-temperature model for electron and phonon subsystems was developed based upon the assumption that the ablation process could be considered as a direct solid-vapor transition. In this case, the lattice was heated on a picosecond time scale, which resulted in the creation of vapor and plasma phases followed by a rapid expansion in vacuum. During all these processes, thermal conduction into the target was neglected. The model was still under experimental verification and received only partial support. The opposite viewpoint was proposed in the model of ultrafast thermal melting of laser-excited solids by homogeneous nucleation. This model was based on the classical nucleation theory, which showed that for sufficient superheating of the solid phase, the dynamics of melting was mainly determined by the electron-lattice equilibration rather than by nucleation kinetics. Complete melting should occur within a few picoseconds. This time scale lays between the longer time scale for heterogeneous melting and the shorter time scale for possibly nonthermal melting mechanisms.

None of the theories above could have been directly applied to the description of periodically pulsed regime of light-matter interaction, in which temporal evolution of the

average temperature came to play a significant role.

This Dissertation was devoted to investigate the interaction of the ultrashort pulse laser and semiconductor material, namely Si and GaP.

2.2. METHODOLOGY

In order to investigate the nature of the ultrashort laser pulse ablation mechanism of semiconductors, an experimental approach was utilized.

A chirped femtosecond laser was used in conducting the experiments. The laser beam had the following parameters: wavelength (λ) of 800 *nm*, adjustable repetition rate from 1 to 1 *kHz*, pulse width of 110 *fs*, and pulse energy of 1 *mJ*. The laser power was controlled using either a half wave plate and a rotating polarizer or a set of neutral density filters. The laser power stability was continuously monitored using a fast-rising time photodiode (1 *ns*). A computer controlled electro-mechanical shutter was used to run the experiment in single pulse mode as well as control the exposure time in the multiple pulses exposure mode.

The target materials, silicon and gallium phosphate, were cleaned with methyl alcohol. Then, the experiments were done in air under atmospheric pressure.

The exposed samples were examined using the optical microscopy, Atomic Force Microscopy (AFM), and Scanning Electron Microscopy (SEM).

The self-imaging experiment's results were analyzed to determine the material status under a single pulse excitation in both cases of silicon and gallium phosphate samples.

Pump and probe experiments were conducted on gallium phosphate to study the

material temporal change of the optical characteristics at fixed laser power. Further investigation was carried out to determine the numerical characteristics of the self-absorption measurements. The transmission as a function of laser power was studied to determine the two-photon absorption coefficient. Experimental findings and theoretical calculations were compared and the observed deviation was explained.

Single and multiple pulses ablation experiments were performed on silicon for MEMS fabrication. The micromachining process was characterized. The optimal parameters were used to fabricate an OMEMS device. The device's surface morphology was characterized then its diffraction characteristics were optically examined using a linearly polarized He-Ne laser provided a 5 mW optical power at 632 nm wavelength.

2.3. ORGANIZATION

The Dissertation is organized into seven chapters. Chapter 1 presents the objectives of this Dissertation. Chapter 2 gives an introduction to this Dissertation.
The introduction chapter includes an overview of laser ablation processes, descriptions of the methodologies used, and the overall organization of this Dissertation. Chapter 3 gives the literature review for the investigations of femtosecond laser interaction with semiconductors followed with the corresponding micromachining applications. Theoretical analyses are presented in Chapter 4, starting with the Maxwell equations and going through the wave equation, ending with the energy excitation and relaxation mechanisms. The experimental setup is discussed in Chapter 5. Four main setups are presented. First, the self-interaction imaging experiment, the two-photon absorption characterization, pump and probe measurement, and finally, the micromachining

application for MEMS. The experimental results and detailed discussion are presented in Chapter 6. In addition, a comparison between the experimental results and the theoretical expectations are given in this chapter. Chapter 7 is devoted for the conclusions of the investigations conducted in this Dissertation along with the proposed future work. Furthermore, references are included at the end of this Dissertation as supporting material.

CHAPTER 3

LITERATURE REVIEW

For decades, precisely ablated semiconductors have been a critical issue for the success of the semiconductor industry. Traditionally, wet chemical etching was utilized to remove layers of the material, but in the pursuit of fabricating photonics devices on a single chip, other technical methods became promising to try. This demand of the industry generated interest in finding a non-wet, non-contact, arbitrarily shaped ablating and reshaping technique for semiconductors.

3.1. LASER INDUCED PHASE TRANSITION

Short pulse inducing phase transition in semiconductors has been an interesting subject of study since early 1980's [36-40]. The thermal model assumes that the emission of the longitudinal phonon is a result of the rapid relaxation of the photoexcited electrons to the lattice vibrational modes [41]. Accordingly, the melting process occurs when the material temperature is raised to the melting temperature after absorbing enough heat [42], suggesting that the phonon emission will cool down the carriers and heat up the lattice in few ps time regimes. Then, the lattice will melt afterwards.

In the case of femtosecond laser pulses, depositing energy into electron-hole pairs sub-system in a time shorter than that required for phonon emission would cause an electronic excitation. Consequently, this excitation would be the reason for the lattice disorder while the lattice remains relatively cold [43].

Shank et. al. [24] reported melting status in silicon after being irradiated with femtosecond laser pulses. Melting was defined as an associated event with the target reflectivity change from solid reflectivity to liquid reflectivity. A femtosecond laser with a 90-femtosecond pulse width was divided into two parts to conduct a pump and probe experiment. The probe pulse was first focused on D_2O to generate a continuum white light for probing the effect of the pump beam at wavelengths of 1000, 620, and 440 *nm*. They suggested that the melt occurred in the front layer and then moved toward a dense region of electron hole plasma. According to their experimental results, the reflectivity jumped and then saturation started to take place about 1.5 picoseconds after the exciting pulse. The reflectivity change was referred to the effect of the dense electron-hole pair created on the surface and the consecutive melting state. They suggested that the melt started in the thin front layer and could reach to the bulk material in the case of high energy laser pulse. The reflectivity of the irradiated material was reflecting a competition between the penetration depth of the probe pulse and the penetrated depth of the melted front. When the penetrated depth of the melted front was deeper than the probe pulse, the melt state reflectivity was dominant.

N. Fabricius et. al. in 1986 [44] utilized the time of the flight mass spectroscopy technique to obtain the velocity distribution of the ablated particles and consequently to determine the ablated material status. Picosecond laser with a 25 *ps* pulse width and nanosecond laser with a 10 *ns* pulse width were used to study the phase transition of the gallium arsenide target. For nanosecond laser pulses, the transition temperature of the solid liquid phase transitions was in agreement with the equilibrium melting temperature, while in the case of the picosecond pulses, the target surface was superheated by several

hundred degrees. The experiment did not reveal details about the ablation mechanism associated with the short pulse interaction.

Second harmonic generation reflection from media with inversion symmetry was proposed by Bloembergen et. al. [45] to be the experiment that might reveal detailed information about the material structure.

In improvement of the second harmonic generation experiment, Tom et. al. [46] reported a loss of cubic order in crystalline Si 150 *fs* after being pumped with a 100 *fs* laser pulse.

P. Saeta et. al. [43] reported an electronic phase transformation of GaAs after pumping the sample with 100 femtosecond laser pulses with a fluence higher than 0.1 J/cm^2. The reflectivity increased within 200 *fs* of the pump pulse. They estimated that more than 50% of the valance electrons were ionized, thus reaching a metallic molten phase. The results suggested that the lattice was driven into a state of disorder directly by high electronic excitation while remaining relatively cold.

P. Stampfli et. al. [47, 48] used a tight-bonding model [49] to study the instability of Si crystal after being irradiated with intense ultrashort laser pulses. They suggested that the reason behind the instability of the diamond structure of silicon crystal was mainly due to the dense electron hole plasma created as a result of ultrashort laser pulses. They suggested that the transverse acoustic phonons reached instability after exciting 8% of the valance electrons to conduction band. Moreover, when about 15% of valance electrons became excited, an atomic displacement of about 1 A occurred in a time interval 100-200 femtoseconds after the exciting laser pulse with a kinetic energy of 0.4 eV. As a result of the high kinetic energy of the atoms, the diamond structure experienced

disorder and melting started on a time scale much shorter than that of thermal melting. Due to the laser induced instability, the energy exchange between the electron subsystem and the lattice was in a form of mechanical work.

K. Sokolowski et. al. [50] investigated the reflectivity change of some semiconductors such as silicon and gallium after performing a femtosecond laser excitation using pump and probe technique. For gallium arsenide, two different phase transformations were suggested according to the exciting laser fluence. The first type of phase transformation happened when the laser fluence was up to 1.5 times the threshold fluence. In this type, a slow phase transition similar to that associated with thermal melting induced by picosecond pulses or longer was expected. The second type of phase transformation was expected when the laser fluence was higher than 2 times the threshold fluence. The transition in this case was of the ultrafast transition nature.

K. Sokolowski et. al. [51] arranged a more detailed pump and probe experiment on silicon and gallium arsenide. The optical reflectivity and reflected SH signal was measured. The suggested two-step model to describe the ultrashort laser induced phase transition obtained results. The excitation stage happened during the femtosecond exciting pulse. In this stage the optical constants and the nonlinear susceptibility of the material were determined by the generation and relaxation of the photo-excited electron-hole plasma. The phase transition from a crystalline solid to a metallic liquid occurred in the second stage with a characteristic time dependent on the exciting laser fluence. For laser fluence about 3 times the threshold fluence, the duration time of this stage was about 300 *fs* with a plasma density in excess of 10^{22} cm^{-3}. It was also suggested that a nonthermal electronic excitation mechanism was responsible for the transformation from

covalent crystalline bonds to metallic liquid state.

P. L. Silverstrelli et. al. [52] presented the molecular dynamic simulation results of heated silicon with laser pulses. They suggested that the high density laser induced electron-hole pairs changed the ineratomic forces by weakening the covalent bonds of the crystal. The simulation suggested that the silicon crystal went into a metallic liquid phase with properties different from those of liquid silicon. The interaction mechanism was considered an intermediate state between modes of plasma annealing, which was triggered by weakening the covalent bonds and ordinary thermal melting, which was associated with an increase in temperature similar to ionic temperature in this process. They suggested that the energy transfer mechanism is different from being direct transfer process.

D. von der Linde et. al. [53] used a high temporal and spatial resolution of time resolved femtosecond pump and probe technique companied with optical microscopy to investigate the laser induced optical breakdown of transparent solids. They investigated the plasma formation due to the interaction of femtosecond laser pulses with transparent material such as glass, magnesium fluoride, sapphire and fused silica. It was shown that the plasma was formed on the surface. The breakdown was observed with a threshold power density in the range of 10^{13} W/cm^2. The breakdown mechanism was attributed to the extrinsic surface properties of the material. Attempts to damage bulk material and produced plasma were unsuccessful because of the strong beam's self-defocusing. They suggested that the self-defocusing occurs due to the effect of the underdeveloping plasma on decreasing the refractive index, which could be very large as the plasma density approached the critical density.

D. von der Linde et. al. [29] used the pump probe imaging technique to investigate the change of surface reflectivity during and after receiving an intense femtosecond laser pulse. The experimental technique allowed recording of a series of photographs at different delay times with high temporal and spatial resolution in the order of 130 *fs* and few microns, respectively. Femtosecond pulses of 130 *fs* and pulse energy few times of the ablation threshold energy were used to study the interaction with materials such as silicon, glass, and gallium arsenide.

The reflectivity variations were observed in a wide dynamic range from of 4% up to 60%. The big change in reflectivity was explained as a result of the optical breakdown of the material and the fully ionization state, which produced high-dense plasma. The ejected ionized material left the material surface with the same speed of plasma expansion in the order of 10^7 cm/s. Direct ablation was the only ablation mechanism suggested with laser pulses much shorter than the plasma expansion time so that no screening effect could exist.

The results of time resolved measurements of silicon and gallium arsenide were similar in the early stages but different in the final surface structures. Similar measurements were performed on aluminum metal film. The time resolved results were similar to those of the semiconductor materials used in the experiment with the only difference being that the ablated area of semiconductor material was uniform; in the case of metal films, the ablated area was non-uniform.

K. Sokolowski-Tinten et. al. [54] arranged an ultrafast time resolved microscopy experiment [31] to study the short laser pulse ablation of semiconductor and metal. Since the nature of the ablation process depended mainly on both the nature of the target

material and laser characteristics such as laser intensity, wavelength, pulse width and number of pulses, they used a well-defined single laser pulse to identify the fundamental physical mechanism of the ablation process. The laser pulse energy was adjusted to be close to the ablation threshold energy and before the onset of the plasma formation. The pump pulse incident had an angle of 45 degrees while the probe beam illuminated the sample and was detected with a high resolution optical microscope. A slight increase of the reflectivity was observed at about 200 *fs*, which they referred to as the creation of the electron–hole plasma induced by the strong electric field of the incident laser pulse. In about a 1 ps time delay from the exciting pulse, a very bright area was observed as a sign of a molten silicon brought by the very strong electronic excitation of the semiconductors. At a much later time ~900 ps, separated and concentric rings appeared around the center of the monitored spot. Finally, in tens of ns, the resolidified material appeared, associated with decreasing of the reflectivity level to that of solid silicon.

The same behavior was observed for other different materials such as GaAs, Au, Ti, Al, and Mg. They considered the existence of the dark rings as a sign of ablation. They concluded by stressing the idea that the short laser ablation was either a thermal or a non-thermal process according the exciting pulse energy. They did not check the situation of high energy laser pulses.

K. Sokolowski-Tinten et. al. [31] studied the thermal and non-thermal melting of gallium arsenide by applying the pump and probe technique combined with high resolution microscopy [54]. Ultrafast electronic melting was observed in sub-picoseconds with pulse energy of 150 mJ/cm^2. The recorded microscopic graphs showed a sharp boundary between two areas. One was experiencing a non-thermal melting as the incident

energy exceeded the energy threshold and the other with heterogeneous thermal melting under overheating condition and lasted for about 100 *ps*. That explained the expansion in bright areas with increasing the time delays.

In reference to Fig. 2 [31], a reflectivity flat top profile was observed with a time delay >1 ps, which could not have been related to the generation of electron hole plasma; however, it could have been related to a melting state reflectivity of GaAs as it was comparable with the tabulated reflectivity value of liquid GaAs. That liquid state observation indicated a molten layer thicker than the penetration depth of the probe beam, which was in the order of 30 *nm*.

As for non-thermal processes, it was believed that once the energy was above the threshold energy, the nonthermal melting occurred as a result of the instability caused by the laser induced dense electron–hole plasma once the plasma density reached to 8-10% of the populated valance electron of the material. The melting process was then occurring homogenously.

A. Cavalleri [55] used the time of flight mass spectroscopy to investigate the melting and ablation process of GaAs after being irradiated with *fs* laser pulses. The nature of the interaction process and the corresponding surface temperature was one of the main goals of their study. The experiment was done on surfaces of GaAs, Si <111> and Si <100> in ultra-high vacuum 10^{-10} torr. Femtosecond laser with a 100 *fs* laser pulse, 620 *nm* wavelength, and 4 *mJ* pulse energy interacted with the material surface at an incident angle of 45 degrees. Energy density ranged from 50 to 500 mJ/cm^2 and was used in conducting the experiment. The results could be divided into four stages of interaction according to the applied laser energy density.

Stage I existed when the laser energy was below the melting threshold. In this case, the hot electrons relax through electron–electron and electron–phonon scattering. The hot carrier relaxation time was in the scale of several picoseconds. The surface temperature was found to be about 1850 K for silicon with estimated activation energy of 0.34 eV which is way below the activation energy for adsorption of single atom, which was about 4.6 eV. It was suggested that this discrepancy in activation energy's value may have been caused by superheating of the solid surface or non-thermal ablation similar to photophysical ablation of polymer.

Stage II was obtained when introducing laser energy that increases the lattice temperature to the melting temperature. Nucleation took place at the surface and a layer of molten material expanded to the bulk. A change in the surface activation energy of silicon was observed indicating that there was an evaporation process initiated in the surface.

Stage III was obtained when the laser energy was less than double of the melting threshold, and non-thermal melting took place. The dense electron–hole plasma created by the laser pulse destabilized the lattice and the energy transfer was faster to the lattice. Surface temperature of silicon was found to be between 3000 and 4000 K, which was significantly below the estimated surface temperature of 5160 K. The surface activation energy remains the same as that observed at lower surface temperature. It was suggested that the results of this stage showed that semiconductors thermalized rapidly after nonthermal melting with no indication of nonthermal contribution to the desorption process.

Stage IV was obtained when energy of the laser pulse slightly exceeded the ablation threshold's energy. Macroscopic parts of the material were ejected in this stage and the surface was textured. Time of flight was not giving reliable information about that interaction regime. Optical measurements were done at different laser energy in order to be compared with the time of flight results. The ring structure disappeared in the case of silicon and gallium arsenide at laser fluence equal to 2.5, and 1.8 ablation fluence, respectively. The time of flight measurements showed a behavior of an ideal gas with average fluence exceeding 2.5 of the ablation fluence, which meant that the majority of the ejected particles underwent supercritical expansion.

D. von der Linde et. al. [32] studied the ablation mechanism of metals and semiconductors using time resolved microscopy. P polarized, Pico and femtosecond laser pulses were introduced to the target material at 55 degrees incident angle. The weak probe beam illuminated the sample and recorded pictures of structure modification taken at different time delays. The laser fluence was kept under the plasma formation threshold. Both the pump and probe beam were of 620 *nm* wavelength and pulse width of 120 *fs* and 5 *ps*. The change in reflectivity of the pumped surface was observed at pulse energy of 0.47 J/cm^2. In the first few hundred femtoseconds, a significant increase in the reflectivity was observed due to the effect of the photo excited electron hole plasma. Higher reflectivity was obtained at a time delay of about 2 *ps* as a result of the silicon metallic liquid state. Melting was believed to have started in less then 1 picosecond as a result of the very strong electronic excitation of the semiconductors. The observation of the ring structure indicated that two sharp interfaces must have been created during the expansion of the ablated material. That interference pattern was possibly created between the

reflected light from front and back side of the ablating layer. At a time delay of infinity, a sharp black ring appeared in the microscopic pictures marking the boundary of the ablated area. Two possible reasons were expected to be the initiators of the observed interference pattern. First was the existence of the bubble structure with layer thinner than the optical penetration depth of the probe beam, which was in order of 10 *nm*. Second, the interference effect might have been produced from an ablation area that was transparent, having high uniform density and a high refractive index.

Molecular dynamic studies [56, 57] suggested three different mechanisms might have been responsible for femtosecond laser ablation of materials, depending on the laser pulse energy. With laser fluence above the ablation threshold, the three ablation mechanisms were active. The three mechanisms were homogeneous nucleation, vaporization, and fragmentation. Homogeneous nucleation and vaporization were photothermal processes, while fragmentation was a photomechanical process. The three mechanisms were effective in different regimes of the target [29].

In the regime where the ablation was not a photothermal process, where fragmentation was the main process, the constant heating of the target induced a thermoelastic stress. The relaxation of the thermoelastic stress extremely speeds up the material expansion. The energy injection in this case varied strong and that caused a spatially non-uniform strain rate.

The elastic energy stored in the liquid layer grew rapidly and the gradient speed of the expansion would have been large and would have inhibited diffusion mechanisms that balanced out the density inhomogeneties. The inhomogeneties would have then lead to the creation of internal surfaces and then would have enabled relaxation of some of the

internal stress. When enough surfaces were created, the initial homogeneous liquid would have agglomerated in clusters and ablation would have started.

B. Rethfeld et. al. [58] described a possible rapid melting of solids being irradiated with femtosecond laser pulses. It was suggested that for sufficient laser pulse energy, a superheating of the material could be obtained. Then, the dynamic of melting was mainly determined by the electron lattice equilibrium rather than by nucleation kinetics. It was expected that the complete melting of the excited material volume took a few picoseconds. For the heterogeneous melting, the melt started at the surface and grew to the solid form with a melt front speed limited by the speed of sound. The melt process in this case was completed in about 100 ps time scale for a layer material in the order of 100 *nm*. The fast homogeneous nucleation melting mentioned above had a characteristic time scale shorter than the heterogeneous melting characteristic time scale and longer than the nonthermal melting characteristic time scale.

B. Rethfeld et. al. [34] expanded on their work in [58] with a theoretical and experimental work in bulk tellurium. Femtosecond time resolved along with polarization microscopy was used to conduct the experiment. It was proven that the boundary between thermal and nonthermal melting was determined by the applied laser energy density. Homogeneous melting of the material was observed to be associated with superheating of material. The time characteristic of that process was in the order of several picoseconds after the exciting laser pulse. The total melting time of the crystal by homogeneous nucleation was determined by the lattice heating time.

3.2. MICROMACHINING OF SEMICONDUCTORS FOR MEMS DEVICES

As for micromachining, the interaction of silicon with ultrashort laser pulses has been studied extensively because of important applications in the semiconductor industry such as Micro-Electro-Mechanical Systems (MEMS) and Optical Micro-Electro Mechanical Systems (OMEMS) [29]. Direct writing on silicon increased the ease of processing by eliminating lithography.

Chao et. al. [59] utilized the fourth harmonic generation of a Nd-YAG laser in an interference setup to write gratings on silicon with periods ranging from 180 *nm* to 550 *nm*. After laser exposure, the samples were etched with hydrofluoric acid (HF) of 10% concentration, and then examined with an atomic force microscope (AFM). The grating lines from the long pulse laser appeared non-uniform, despite a good absorption of the UV wavelength with the target.

Ngoi et. al. [13] used a frequency doubled 150 *fs* Ti-sapphire laser in a vacuum chamber to obtain sub-micron structures on silicon wafers. They reported machined lines of 500 *nm* width and 100 *nm* depth, but the lines were discontinuous and the edges irregular.

Ngoi et. al. [60] studied the machining of <111> silicon wafers with a 400 *nm* second harmonic Ti-sapphire laser using a 300 *fs* pulse width. The energy of the laser pulses was varied from 50 to 100 nJ. A linear relation was found between the machining quality and the laser energy. Yet, the micromachining process was subject to a trial and error procedure and not investigated in a detailed, consistent way. In this Dissertation, we utilized the learned information about the short pulse ablation mechanism of semiconductor to illustrate and test a high quality micromachined a silicon optical device.

J. Bonse et. al. [29] studied the modification of silicon with femtosecond laser pulses of variable pulse width ranging from 5 to 400 *fs*. Single and multiple pulse experiments were performed. Laser pulse energy of ½ *mJ* was used to conduct the experiment. The pulse width was varied by inserting dispersive glass plates in the beam path. For the single pulse experiment and energy density of 1.5 J/cm^2, three different modification processes were observed using optical microscopy. Going from higher to lower energy across the spatial profile of the Gaussian pulse, ablation region was observed first followed by bubble formation due to the boiling beneath the surface, followed by the region of recrystallization and amorphization, and, finally, the oxidation region. The ablation with multiple laser pulses was studied. The multiple pulses ablation threshold was determined to be 0.21 J/cm^2. With laser energy 5 times the ablation threshold, ripple formation was observed. Increasing the laser energy to 10 times the ablation fluence, conical structure was observed. At laser energy of 20 times the ablation threshold, volcano-like structure was observed on the ablated region.

The spike formation of multiple femtosecond laser exposure was observed in etching gas environment such as Cl_2 or SF_6 by Tsing-Hua Her et al. [61]. The spikes were conical in shape with 40 microns tall and 1 micron diameter. Irradiating the sample in N_2, He or in vacuum did not construct the conical spikes.

Having a good quality machining laser beam has been one of the big concerns in micromachining process. Spatial filtering technique was introduced to the micromachining experiment with different pulse widths (nanoseconds [60, 14], femtoseconds [13, 62, 63]) to improve the beam quality and consequently the micromachining quality. The setup consisted of two identical convex lenses and a pinhole

placed exactly in the focus plan. The laser beam was first focused by the first lens through the pinhole and then recollimated by the second lens. Many challenges, such as the deterioration of the pinhole and the reduction of the laser power, were the main drawbacks of the technique especially when the filter was used in air.

S. Juodkazis et. al. [64] studied the hole drilling of silicon using femtosecond laser of 80 *fs* pulse width at the fundamental wavelength (800 *nm*). The study was done at 5 torr of ambient air pressure. It was found that the low air pressure helped in improving the micromachining quality in terms minimizing the debris around the machined area. They refer the improvement in machining quality to decreasing the air breakdown at the used ambient air pressure.

C. Y. Chien et. al. [65] studied the pulse width effect on the micromachining quality of silicon. Ti-sapphire femtosecond laser of 2 *mJ* maximum pulse energy, 800 nm fundamental wavelength, and up to 1 *kHz* adjustable repetition rate was used in conducting the experiment. The pulse width was varied from 110 fs up to 10 *ps*. The pulse width boundary that introduce melting was found to be 5 *ps*. Parameters such as incident laser polarization with respect to the machining direction, laser contrast, ambient machining gas were found to be essential parameters that need to be optimized to ensure a high quality micromachining. However, the micromachined features in this experiment were in the order of few hundred microns, which in not applicable in many MEMES applications that required microns and submicron features. Optimal condition for micromachining applications were not introduced as a result of the experiment.

E. Coyne et. al. [66] studied the structural change due to micromachining of wafer grade silicon. Femtosecond laser of 150 *fs* pulse width, 775 *nm* wavelength and 1 k Hz

repetition rate. The laser energy density was varied from 0.43 J /cm ^{2} to 14 J/cm^2. Scanning transmission electron microscopy was used to investigate the thermal and mechanical damage in the samples. It was shown that, minimal heat affected zone features can be obtained by using femtosecond micromachining techniques; however, lattice damage is created by mechanical stresses and the deposition of the ablated material limits the extent to which this feature can be obtained. The mechanical damage observed at the above mentioned maximum energy density was in the range of 4 μm.

3.1. SUMMARY

The field of laser-induced phase transitions in semiconductors dates back to the discovery in the 1970's that semiconductor crystals could be 'annealed' by irradiation with a short intense laser pulse. Two models were proposed to explain the structural change because of the laser excitation. The first is the thermal model, which describes the structural change as a thermal melting process. In this model it is assumed that the hot electrons rapidly equilibrate with the lattice through phonon emission. The laser energy deposited to the material is converted instantly to heat. According to the incident intensity of the laser pulses, lattice temperature will heat up until it reaches to melting and vaporization state. The second model is the plasma model. This model attributes the structural change to destabilization of the covalent bonds resulting directly from the electronic excitation. In this model, it is assumed that the rate of phonon emission by the excited electronic system is slow compared to the energy deposition time (*i.e.*, the laser pulse width). According to this model, the structural change is driven directly by the excited electronic system. When the excited electronic system reaches 8 – 10% of the

valence electrons, the crystal becomes unstable, and a structural phase transition occurs. For nanosecond and picosecond pulses the phase transition from solid to liquid is purely thermal as the pulse width is either in the same ranger or higher than the lattice relaxation time.

In Femtosecond laser excitation case, highly nonequilibrium dynamic is observed. Reflectivity and second-harmonic generation studies of femtosecond laser excited semiconductors show evidence of rapid changes in the material (within a few hundred femtoseconds) following the excitation. The studies were performed at low or moderate energy densities. Different techniques were used to assure the results, mainly imaging pump and probe technique.

At high energy regime, ten times more than the ablation threshold, some speculations ranged between thermal melting, non-thermal melting, or phase explosion. No experimental study was done to verify the material behavior during the femtosecond excitation at that energy density regime.

As for micromachining application, it is proven that ultrashort laser pulses are a promising micromachining tool for MEMS fabrication; yet, reaching a reliable and efficient micromachining process required that many scientific and technical problems have to be investigated. Basic investigation of single and multiple pulses material removal need to be performed systematically. Characterization of the governing micromachining parameters such as laser energy density, ambient gas, laser scanning direction with respect to the incident polarization orientation, pulse contrast, and the effect of beam spatial reshaping, need to be performed for the best utilization of femtosecond laser unique features.

CHAPTER 4

THEORETICAL ANALYSIS

The interaction between laser and matter depends on the optical properties of the material and the behavior of the incident pulses on the surface and inside the material.

In this chapter, theoretical analysis dealing with semiconductor will be reviewed: starting with the Maxwell equation to describe the nature of the light wave, and then going through the wave equation and the change in the refractive index of the material being irradiated with laser pulses. The energy diagrams of the semiconductors will be illustrated. The semiconductor material turns to a metallic nature in the case of melting. The energy transferee mechanism will be studied in the case of femtosecond laser irradiation. Finally, the ablation mechanism will be studied.

4.1 LIGHT MATTER INTERACTION

4.1.1 MAXWELL EQUATIONS

Material optical properties depend on the propagation nature of the light inside the material. Propagation of light inside solid material is well described by the Maxwell equations. We will consider the four Maxwell equations without any modifications that would customize them for the case of conducting and non-conducting materials. The two material classifications will cover the semiconductor in non-melting and melting states, respectively. Note that throughout the equations of this Dissertation, bold italic letters will represent vectors. The differential Maxwell equation can be written as following:

$$\nabla \times \boldsymbol{E} = -\frac{\partial \boldsymbol{B}}{\partial t} \tag{4.1}$$

$$\nabla \times \boldsymbol{H} = \frac{\partial \boldsymbol{D}}{\partial t} + \boldsymbol{J} \tag{4.2}$$

$$\nabla \cdot \boldsymbol{D} = \rho \tag{4.3}$$

$$\nabla \cdot \boldsymbol{B} = 0 \tag{4.4}$$

where $\boldsymbol{E}$ is the electric field vector; $\boldsymbol{H}$ is the magnetic field vector; $\boldsymbol{D}$ and $\boldsymbol{B}$ are the corresponding displacement vectors of the electric and magnetic fields, respectively; ρ is the charge density; and $\boldsymbol{J}$ is the current density.

The response of the conduction electrons to the electric field is given by Ohm's law $\boldsymbol{J} = \sigma \boldsymbol{E}$ (4.5)

where σ is the conductivity.

The response of the bound electrons to the propagated fields inside the material is represented in the displacement vectors $\boldsymbol{D}$ and magnetic induction $\boldsymbol{B}$. $\boldsymbol{B}$ and $\boldsymbol{D}$ are described by the following relations for non-magnetic material:

$$\boldsymbol{D} = \varepsilon_o \boldsymbol{E} + \boldsymbol{P} \tag{4.6}$$

$$\boldsymbol{B} = \mu \boldsymbol{H} = \mu_o \boldsymbol{H} + \boldsymbol{M} \tag{4.7}$$

where ε_o is the permittivity in vacuum, μ_o is the permeability in vacuum, μ is the permeability of the materials, $\boldsymbol{M}$ is the magnetization, and $\boldsymbol{P}$ is the induced electrical polarization.

Alternately, the response of the bound electron can be written as:

$$\boldsymbol{P} = (\varepsilon - \varepsilon_o)\boldsymbol{E} = \chi \varepsilon_o \boldsymbol{E} \tag{4.8}$$

where $\chi = \varepsilon/\varepsilon_o - 1$ is the electric susceptibility.

Susceptibility χ is a scalar quantity in the case of isotropic material, while in non-isotropic material, χ is a vector quantity. In this case, the magnitude of the induced

polarization varies with the direction of the applied field and χ is expressed, then, in tensor, which describes most of the material optical properties.

4.1.2 WAVE EQUATION

The differential Maxwell equations described above (4.1- 4.4) can be manipulated to obtain the wave equation. In our case, we will consider a non-magnetic and electrically neutral material: M and ρ equal to zero. Substituting equation (4.7) into (4.1) and dividing both sides by μ and applying the curl operator will give the following equation:

$$\nabla\times(\frac{1}{\mu}\nabla\times\boldsymbol{E})+\frac{\partial}{\partial t}\nabla\times\boldsymbol{H}=0 \tag{4.9}$$

Differentiating equation (4.2), with respect to time, then using (4.6) and substituting into (4.9):

$$\nabla\times(\frac{1}{\mu}\nabla\times\boldsymbol{E})+\varepsilon\frac{\partial^2\boldsymbol{E}}{\partial t^2}=0 \tag{4.10}$$

Using the following vector identities:

$$\nabla\times(\frac{1}{\mu}\nabla\times\boldsymbol{E})=\frac{1}{\mu}\nabla\times(\nabla\times\boldsymbol{E})+(\nabla\frac{1}{\mu})\times(\nabla\times\boldsymbol{E}) \tag{4.11}$$

$$\nabla\times(\nabla\times\boldsymbol{E})=\nabla\cdot(\nabla\cdot\boldsymbol{E})-\nabla^2\boldsymbol{E} \tag{4.12}$$

Equation (4.10) will be

$$\nabla^2\boldsymbol{E}-\mu\varepsilon\frac{\partial^2\boldsymbol{E}}{\partial t^2}+(\nabla\log\mu)\times(\nabla\times\boldsymbol{E})-\nabla(\nabla\cdot\boldsymbol{E})=0 \tag{4.13}$$

Substituting from (4.6) into (4.3) and using the vector identity

$$\nabla\cdot(\varepsilon\boldsymbol{E})=\varepsilon\nabla\cdot\boldsymbol{E}+\boldsymbol{E}\cdot\nabla\varepsilon \tag{4.14}$$

Equation (4.13) will be

$$\nabla^2 \boldsymbol{E} - \mu\varepsilon \frac{\partial^2 \boldsymbol{E}}{\partial t^2} + (\nabla \log \mu) \times (\nabla \times \boldsymbol{E}) + \nabla (\boldsymbol{E} \cdot \nabla \log \varepsilon) = 0 \qquad (4.15)$$

Considering homogeneous and isotropic mediums, the gradient term of μ and ε goes to unity and the wave equation takes the following forms:

$$\nabla^2 \boldsymbol{E} - \varepsilon\mu \frac{\partial^2 \boldsymbol{E}}{\partial t^2} = 0 \qquad (4.16)$$

The solution will be in the form

$$\boldsymbol{E} = \boldsymbol{E}_0 exp(i\omega t - \boldsymbol{k}r) \qquad (4.17)$$

where ω is the angular frequency and $\boldsymbol{k}$ is the wave vector related by the equation $|\boldsymbol{k}| = \omega\sqrt{\mu\varepsilon}$.

4.1.3 LASER WAVE PROPAGATION

When applying a high intensity laser beam, a nonlinear response of the atoms and molecule of the material is expected. In the presence of an electric field, the polarization increases by increasing the polarized atoms. Although the laser induced polarization of the material and is not proportional to the laser electric field, it can be expressed in a Taylor series expansion as:

$$\begin{aligned} \boldsymbol{P}_i &= \varepsilon_o \chi_{ij}^{(1)} \boldsymbol{E}_j + \chi_{ijk}^{(2)} \boldsymbol{E}_j \boldsymbol{E}_k + \chi^{(3)} \boldsymbol{E}_j \boldsymbol{E}_k \boldsymbol{E}_l + \ldots = \\ &= \boldsymbol{P}^{(1)} + \boldsymbol{P}^{(2)} + \ldots + \boldsymbol{P}^{(n)} \end{aligned} \qquad (4.18)$$

where χ is the material optical susceptibility and P is the polarization. The first term in (4.18) represents the linear polarization, then increases the order to the n^{th} term. For the second order polarization to be considered, the applied electric field should in the order of atomic field strength E_{at}.

For monochromatic laser beams of angular frequency ω_o and propagating in the z-direction, consider the laser field taking the following form:

$$E(z,t) = Re(E_i(\omega_o, z))exp(i\omega_o t) = \frac{1}{2}\left[E(\omega_o, z).exp\{i(\omega_o t - kz)\} + c.c.\right] \quad (4.19)$$

The polarization will be rewritten as:

$$P^{(3)}(z,t) = \frac{1}{2}\left[P^{(3)}(\omega_o, z).exp\{-i(\omega_o t)\} + c.c.\right] \quad (4.20)$$

Now we return to the Maxwell equations and look closely at the polarization.

Substituting from (4.6) into (4.2)

$$\nabla \times H = \frac{\partial D}{\partial t} + J = \frac{\partial(\varepsilon_o E + P)}{\partial t} + J \quad (4.21)$$

Now the material polarization can be considered as a summation of linear and nonlinear components

$$P = \varepsilon_o \chi_L E + P_{NL} \quad (4.22)$$

Equation (4.21) will be rewritten as

$$\frac{\partial}{\partial t}(\nabla \times \mathbf{H}) = \sigma \frac{\partial E}{\partial t} + \varepsilon_o \frac{\partial^2 E}{\partial t^2} + \frac{\partial^2 P_{NL}}{\partial t^2} \quad (4.23)$$

$$\nabla \times E = -\frac{\partial B}{\partial t} = -\frac{\partial}{\partial t}(\mu_o H) \quad (4.24)$$

where $\varepsilon = \varepsilon_o(1+\chi_L)$.

Taking curl of (4.24), then substituting for the right-hand-side from (4.23) and using the vector identity (4.12), we get

$$\nabla^2 E = \mu_o \sigma \frac{\partial E}{\partial t} + \mu_o \varepsilon_o \frac{\partial^2 E}{\partial t^2} + \mu_o \frac{\partial^2 P_{NL}}{\partial t^2} \quad (4.25)$$

Now we substitute from (4.19) and (4.20) into (4.25):

$$-i\left[\frac{2\omega_o n}{c}\right]\frac{dE_i(\omega_o,z)}{dz}+\frac{\omega_o{}^2K^2}{c^2}E_i(\omega_o,z)-\frac{i2nK\omega_o{}^2}{c^2}E_i(\omega_o,z)$$
$$=\frac{i2nK\omega_o{}^2}{c^2(n+iK)^2}P_i^{(3)}(\omega_o,z) \qquad (4.26)$$

where n is the refractive index and K is the extension:

$$\varepsilon(\omega)=[\,n(\omega)+iK(\omega)]^2 \qquad (4.27)$$

Expressing the amplitude E and the phase Φ of the electric field:

$$E_i(z)=\left|E(z)\right|_i.exp\{i\Phi(z)\} \qquad (4.28)$$

i is the i^{th} component of the electric field amplitude.

Assuming the following algebraic connection between the susceptibility and polarization

$$P_i^{(3)}=\varepsilon(\omega_o)\chi_{ijkl}^{(3)}(\omega_o)E_jE_kE_l \qquad (4.29)$$

From (4.28) into (4.26) and substituting for the polarization by (4.29) then separating real and imaginary parts results in two equations of amplitude E and phase Φ of the electric field.

$$\frac{d\left|E(z,t)\right|_i}{dz}=-\frac{\omega_o K}{c^2}\left|E(z,t)\right|_i-\frac{2\pi\omega_o}{nc}\left[Im\chi^{(3)}(\omega_o)\right]_{ijkl}.\left|E(z,t)\right|_j.\left|E(z,t)\right|_k.\left|E(z,t)\right|_l$$
$$\left|E(z)\right|_i.\frac{d\Phi(z,t)}{dz}=-\frac{\omega_o{}^2K^2}{2nc}\left|E(z,t)\right|_i+\frac{2\pi\omega_o}{nc}\left[Re\chi^{(3)}(\omega_o)\right]_{ijkl}.\left|E(z,t)\right|_j.\left|E(z)\right|_k.\left|E(z,t)\right|_l$$

(4.30)

where $K=\frac{c}{2\omega_o}[\alpha+\sigma_{eh}N]$, N is the density, σ_{eh} is the carrier cross-section and α is the linear absorption coefficient.

Finally, multiply (4.30) by $\left|E\ (z,t)\right|_i$ and summing up all repeated indices, we obtain the equation for intensity $I(\omega_o,z)=(\frac{cn}{8\pi})\left|E(z,t)\right|^2$ (4.31) and phase of the pulse as the following:

$$\begin{aligned}\frac{dI(z,t)}{dz} &= -\alpha I(z,t)-\sigma_{eh}N(z,t)I(z,t)-\beta I^2(z,t)\\ \frac{d\Phi(z)}{dz} &= -aN(z,t)+bI(z,t)\end{aligned} \tag{4.34}$$

$$\beta=\frac{32\pi^2\omega_o}{n^2c^2}F(\theta(Im\chi^{(3)}(\omega_o))) \tag{4.35}$$

where F is a function of the incident angle θ and the imaginary part of the 3rd order susceptibility, a and b are constants, which are described by the next equations:

$$a=\frac{e^2}{2nm_{eh}\omega_o} \tag{4.36}$$

$$b=\frac{16\pi^2\omega_o}{n^2c^2}F(\theta(Re\chi^{(3)}(\omega_o))) \tag{4.37}$$

Equation (4.33) has to be supplemented with a kinetic equation, which is

$$\frac{dN(z,t)}{dt}=\frac{\alpha I(z,t)}{\hbar\omega_o}+\frac{\beta I^2(z,t)}{2\hbar\omega_o}+D\nabla^2N(z,t)-\frac{N(z,t)}{\tau_{eh}} \tag{4.38}$$

where D is the diffusion coefficient of electron-hole pairs, and τ_{eh} is the electron–hole pair recombination's lifetime. The system equation (4.34 - 4.38) represents both the intensity and the phase variation of the light pulse propagating in the medium with the 3rd order nonlinear polarization.

4.1.4 MODIFIED OPTICAL PROPERTIES

The material response to the electric field depends on whether that electric field strength perturbs the state of the electrons and atoms of the material or not. In the case of a non-perturbing electric field, typical optical properties of the material are expected. In the case of a perturbing electric field, the optical properties of the material may be altered. This section is devoted to illustrating some of the phenomena associated with applying an intense electric field.

4.1.4.1 ELECTRON-HOLE PLASMA GENERATION

The laser excitation of semiconductors can be done through linear or nonlinear absorption according to the laser photon energy with respect to the material band gap. If the photon energy is equal to or higher than the material band gap, the incident photon will ionize the irradiated atom through a linear absorption process. In the case of lower photon energy than the material band gap, more than one photon with summation energy equal to the energy band gap is required to ionize the atom through a nonlinear absorption process.

For intrinsic semiconductors, the equilibrium free carrier density at temperature T is given by [67]

$$\overline{N}_{eh} = 2\left[\frac{k_B T}{2\pi\hbar^2}\right]^{3/2} (m_e m_h)^{3/2} exp\left[-\frac{E_g}{2k_B T}\right] \qquad (4.39)$$

where m_e, m_h are the electron and hole effective masses, respectively, and k_B is the Boltzmann constant.

The total absorption coefficient of a semiconductor material can be described by the following equation:

$$\alpha_{total} = \alpha + N_{eh}\sigma_{eh} \tag{4.40}$$

where N_{eh} = N_e= N_h is the density of carrier pairs and α_0 is the linear absorption coefficient.

The absorption cross section of the electron-hole pairs, $\Sigma$is defined as the following:

$$\sigma_{eh} = \frac{e^2}{\varepsilon_0 n_1 c\omega^2}\left[\frac{1}{m_e\tau_e} + \frac{1}{m_h\tau_h}\right] \tag{4.41}$$

where τ_e, τ_h are the collision time for electrons and holes, respectively.

4.1.5 OPTICAL PROPERTIES OF HIGH INTENSITY LASER IRRADIATED SEMICONDUCTORS

In the case of the high intensity laser excited semiconductors, high dense electron-hole plasma in the order of 10^{22} cm^{-3} or higher is expected. Because of the fast carrier-carrier scattering, the initial distribution of the excited plasma thermalizes in a few tens of femtoseconds, leaving the initial carrier temperature >10^4 K in non-degenerate plasma [68-70].

There are three physical effects that might be responsible for the changes of excited e-h plasma's linear optical properties, namely, (a) state and band filling [71-72] (b) band structure renormalization [73], and (c) free carrier response. Assuming that each of these physical processes contributes independently to the material's dielectric constant, [74] the change can be presented as

$$\varepsilon^* = \varepsilon_g + \Delta\varepsilon_{pop} + \Delta\varepsilon_{bgs} + \Delta\varepsilon_{fcr} \tag{4.42}$$

where ε_g is the dielectric constant of the unexcited material, and $\Delta\varepsilon_{pop}$, $\Delta\varepsilon_{bgs}$, and $\Delta\varepsilon_{fcr}$ are the changes of the dielectric material due to three physical processes mentioned above, respectively.

4.1.5.1 STATE AND BAND FILLING

The estimation of the state and band filling on the change of the dielectric constant acquires detailed information about the carriers distributions in both valance and conduction bands; however, due to the presence of high-temperature carriers, a uniform distribution over the Brillouin zone is assumed. The magnitude of $\Delta\varepsilon_{pop}$ is estimated from the ratio between the excited carriers' density and the total valance band density as shown in the following equation [75]:

$$\Delta\varepsilon_{pop} = -(\varepsilon_g - 1)\frac{N_{eh}}{N_0} \tag{4.43}$$

where N_{eh} is the excited carriers density and N_0 is the total valance band density.

4.1.5.2 BAND STRUCTURE RENORMALIZATION

The changes of the single particle energy due to the many body interactions, in the surface plasma can be described by the band structure renormalization. A shift in the band gap structure with a shrinkage proportional to the cubic root of the plasma density is assumed [73-76], however, due to the temperature dependence of the band gap, a deviation from the cubic root proportionality is expected and the change in optical properties is estimated from the corresponded shift in the optical spectra [77]. The optical change is described by the following equation [74]:

$$\Delta\varepsilon_{bgs} = \varepsilon_g(\hbar\omega + \Delta E_{gab}) - \varepsilon_g(\hbar\omega) \tag{4.44}$$

4.1.5.3 FREE CARRIER RESPONSE

The response of the free carriers on the optical properties can be described from the Drude model by the following equation [73]:

$$\Delta\varepsilon_{fcr} = -\frac{Ne^2}{\varepsilon_0 m^*_{opt} m_e \omega^2}\frac{1}{1+i\frac{1}{\omega\tau_D}} = \left[\frac{\omega_p}{\omega}\right]^2 \frac{1}{1+i\frac{1}{\omega\tau_D}} \tag{4.45}$$

where $m^*_{opt} = (1/m_e + 1/m_h)^{-1}$ is the optical effective mass of the carriers, τ_D is the Drude damping time, and ω_p is the plasma frequency.

Both the optical effective mass and the Drude damping time depend on the plasma density and temperature. Among the three physical processes, at high density plasma of 10^{22} cm^{-3} or more, the free carrier response was suggested to be the dominant process that affected the dielectric constant of the material [78].

4.1.6 LASER ENERGY TRANSFER MECHANISMS

4.1.6.1 OPTICAL EXCITATION

In direct band semiconductors, optical excitation mechanisms could be a direct excitation process in which one or more photons create an electron-hole pair and excite the carrier to higher energy levels as shown in Fig. 4.1.-a,b. Other excitation processes require creating or absorbing photons for the sake of momentum conservation, as shown in Fig. 4.1-c. The last excitation process is an impact ionization, in which a carrier of higher energy excites another carrier in the valance band.

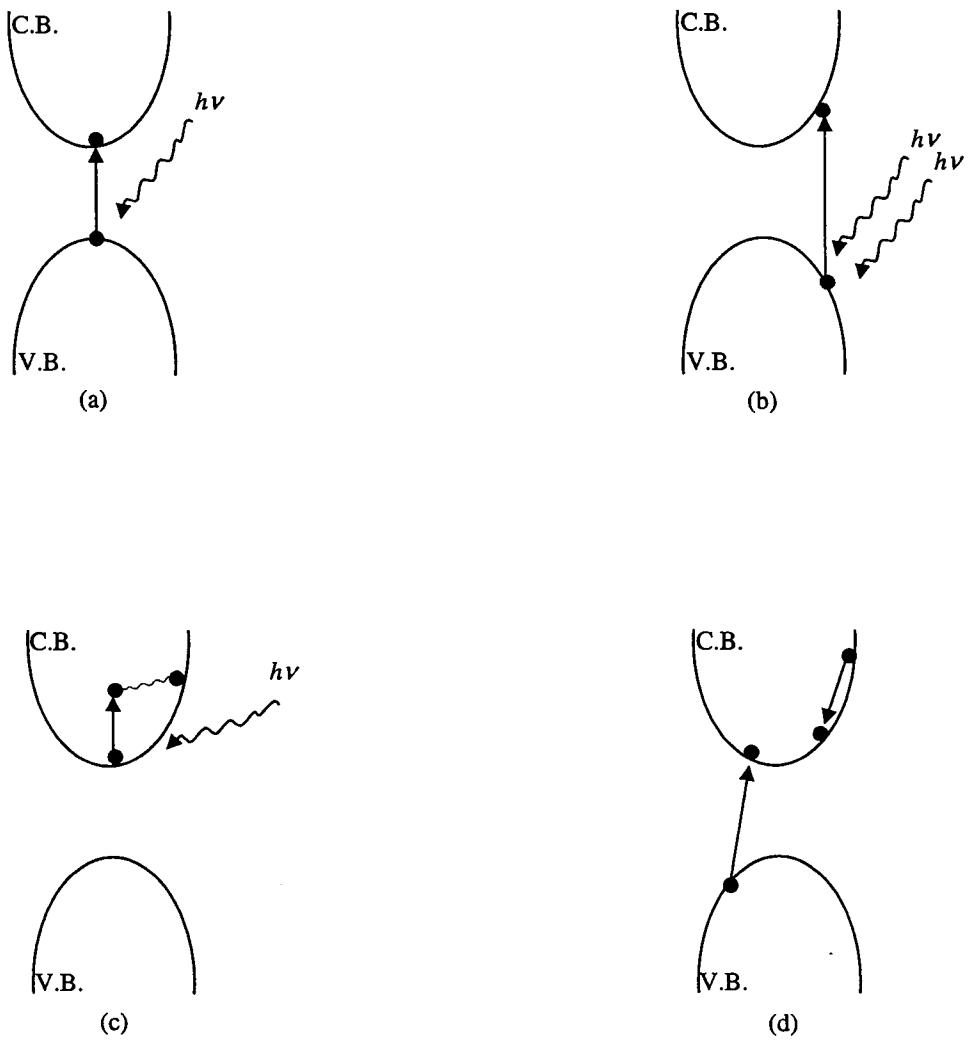

Fig. 4.1.: Optical excitation mechanisms in semiconductors.

(V.B. is the valance band, C.B. is the conduction band)

a) Single photon excitation

b) Multiphoton excitation

c) Conduction band Excitation

d) Avalanche Ionization

4.1.6.1.1 SINGLE AND MULTIPHOTON EXCITATION

When a photon of energy equal to or higher than the material band gap interacts with the material, an electron-hole pair is created. In indirect band gap semiconductors, an additional photon is needed to conserve the momentum. The carrier density can be estimated knowing the absorption depth, the material reflectivity, and the laser fluence as shown in the following equation:

$$N = \frac{(1-R)F\alpha}{h\upsilon} \tag{4.46}$$

where N is the carrier density, R is the material reflectivity, F is the laser fluence, h *is* Planck's constant, ν is the photon frequency, and α is the absorption coefficient.

However, the density of the available states and band filling limits the carrier's density that could be achieved through single-photon absorption process. Multi-photon absorption is another excitation process that requires more than one photon to be absorbed simultaneously to create the electron-hole pairs. Fig. 4.1-b is a schematic diagram of the multi-photon process. Since more than one photon produces an electron-hole pair, the multi-photon absorption process is less efficient than the single-photon absorption process; however, this process populates different states so it does not alternate single-photon processes and consequently helps overcome the band filling. The probability of a multi-photon process is much less than a single-photon process, but it directly proportions with the laser intensity and can be described as the following:

$$\frac{dN}{dt} = \sigma_m I^m N \tag{4.47}$$

where N is the electron density, σ_m is the multiphoton absorption coefficient, I is the laser intensity, and m is the number of multiphoton process.

For a detailed formula of the two-photon absorption, equations (4.34) and (4.38) should be solved together with some assumptions. For a femtosecond pulse we may neglect both terms of diffusion and recombination and the transmission T of semiconductor sample can be written as [79]:

$$T(I_0) = \frac{2(1-R)}{d_0 \beta I_0 \pi^{1/2}} \int_0^{\infty} ln(1 + \beta I_0 (1-R) d_0 exp(-x^2)) dx \qquad (4.48)$$

where R is the reflectivity coefficient, d_0 is the sample thickness, and β is the two-photon absorption coefficient.

4.1.6.1.2 CONDUCTION BAND EXCITATION

Carriers in the conduction band will absorb photons and go to a higher energy level- resonance situation- otherwise; the free electron absorption will be a three-particle process with an emission or absorption of a phonon or a scattering of another electron. The process will not increase the carriers' density but will increase the carriers' energy. The imaginary part of the dielectric constant represents the interaction between photons and free carriers with an absorption depth given by

$$\alpha = \frac{\omega_p^2}{Nc} \frac{\gamma}{\omega^2 + \gamma^2} \qquad (4.49)$$

where N is the free carrier density, ω is the photons frequency, ω_p is the resonant plasma frequency, and γ is the damping force of the free electron under the influence of the E field.

The excitation process leads to ionization when the incoming photon energy is higher than the ionization energy of the electron.

4.1.6.1.3 AVALANCHE IONIZATION

Avalanche ionization is a process that involves free carriers' absorption followed by an impact ionization process, as shown in Fig. 4.1-d. An electron in a conduction band absorbs incoming photon energy and is either excited to a higher level in the conduction band or ionized. The excited electrons will eventually be ionized and then, via collisions with other electrons in the valance band, the number of carriers will be multiplied. As long as the laser field exists, the carriers' density in the conduction band is described as the following:

$$\left(\frac{d\rho}{dt}\right)_{Avalanche} = \eta(E)\rho \qquad (4.50)$$

where η is the avalanche ionization rate.

The excitation optical process with ultrashort laser pulses can be summarized as following: the photon excitation will be due to a single- or multi-photon absorption creating an electron-hole pair. For high intensity laser pulses, due to the band filling, the single-photon excitation process will saturate. However, the multi-photon absorption process and the free carriers' absorption will create more energetic carriers. The newly created carriers will multiply the number of the created carries through impact ionization process.

4.1.6.2 RELAXATION PROCESS

After the laser pulse elevates the number of the free electrons in the conduction band, the carriers tend to relax quickly through number of relaxation mechanisms, as shown in Fig. 4.2.-a-d.

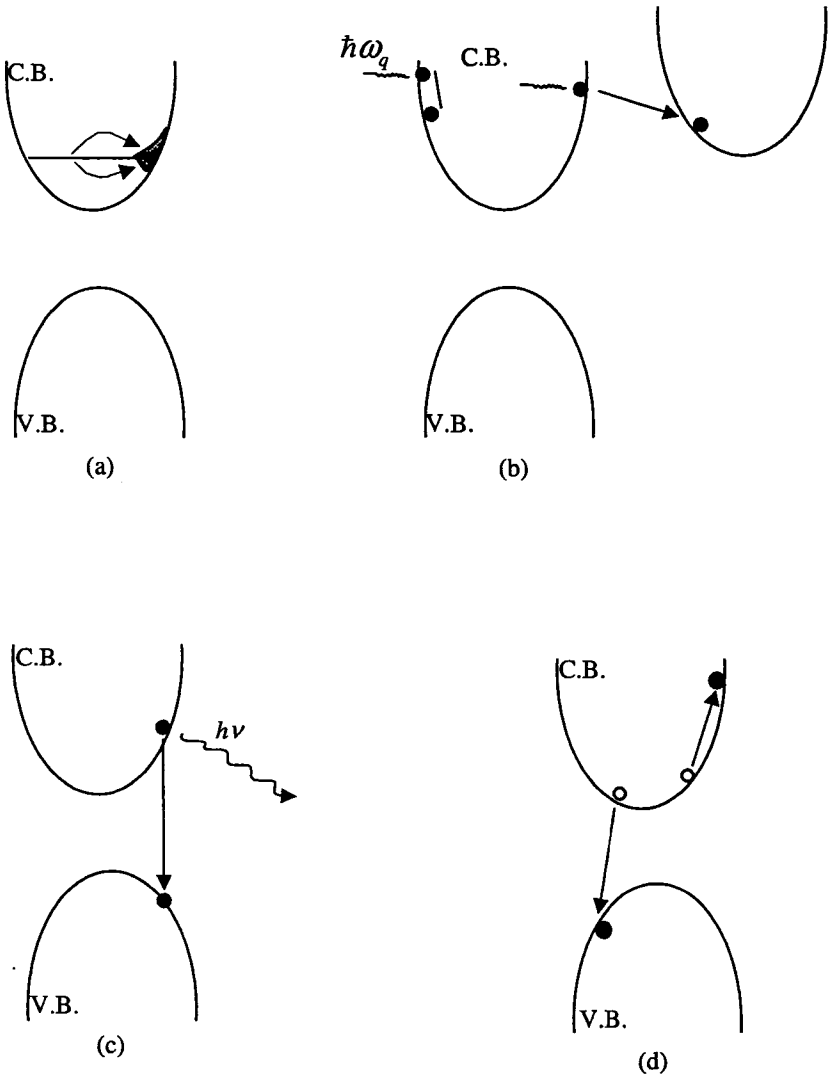

Fig. 4.2.: Relaxation mechanisms in semiconductors

(V.B. is the valance band, C.B. is the conduction band)

a) Thermalization through carrier-carrier scattering

b) Carrier-phonon inelastic scattering

c) Radiative electron-hole recombination

d) Non-radiative electron-hole recombination

4.1.6.2.1 CARRIER-CARRIER SCATTERING

Carrier-carrier scattering is the first relaxation mechanism shown in Fig. 4.2.-a. This relaxation process introduces a thermalization of the non-equilibrium carrier distribution introduced by the laser pulses in a time regime of a few femtoseconds. The carrier-carrier scattering does not affect the carrier density nor the carrier's total energy; however, if introduced, a new distribution of the carrier over the bands consequently helps in overcoming the band filling effect in the excitation process.

4.1.6.2.2 CARRIER-PHONON INELASTIC SCATTERING

Carrier-phonon inelastic scattering is shown in Fig. 4.2.-b. as the second relation mechanism of the excited semiconductor. In this process, the highly excited free carrier emits a phonon that reduces the carrier energy and heats the lattice at the same time. The process time scale is in the range of 100 fs; however, the energy of the longitudinal optical phonon is a lot smaller than the excess energy of the excited carrier, which means tens of phonons are required to get rid of the excited carrier excess energy.

4.1.6.2.3 RADIATIVE AND NON-RADIATIVE CARRIER RECOMBINATION

Free electrons and holes are combined in a two recombination processes, radiative and non-radiative recombination as shown in Fig. 4.2.-c and d, respectively. In the radiative recombination process, an electron recombines with a hole both are of the same wave vector emitting a photon of energy equal to the excess energy. The process takes place in a time scale of 1 *ns* and decreases both the free carrier energy and density. On the other hand, the non-radiative recombination process is the inverse of the impact

ionization and is also called Auger recombination. In this process, an electron and hole recombine and transfer momentum and energy to a third carrier. The process is proportional to the cubic value of the carrier density and therefore it is significant at the high density of the femtosecond laser excitation.

4.1.6.2.4 CARRIER DIFFUSION

The last mechanism to affect the free carrier density in the localized laser excited material is the carrier diffusion out of the laser affected area. The carrier density varies in the normal direction of the sample surface when the laser spot size on the sample is much bigger than the laser absorption depth. The carrier density in this case is described as the following:

$$N(z) = N(0)e^{-z/\delta} \tag{4.51}$$

where δ is the optical absorption depth and is equal to the inverse of the absorption coefficient α.

The diffusion τ_{diff} is given by [80]

$$\tau_{diff} = \delta^2 / D_a \tag{4.52}$$

where D_a is the ambipolar constant and is related to the excited electron temperature by the following equation [80, 41]:

$$D_a = k_B T_e \mu_a / e \tag{4.53}$$

where k_B is the Boltzmann constant, μ_a is the reduced carrier mobility for conduction electrons and valance holes and e is the electron charge.

Diffusion D_a varies with the change of the electron temperature during and after the ultrashort pulses. It is expected that by increasing the electron temperature, the

diffusion process will speed up; however, in case of the femtosecond laser excitation the diffusion process is slowed down. The diffusion slowing down comes because of the carrier confinement that happens with the gradient carrier density being introduced by the gradient intensity of the exciting laser pulse [41].

4.2 LASER MATERIAL REMOVAL

The interaction between femtosecond laser pulses and material occurs within the femtosecond pulse width and, consequently, processes such as heating, melting and evaporation take place on the laser-irradiated area before the heat transfers to the lattice. Electron-hole pairs generated in semiconductor material can exist before the laser pulse because of environmental temperature affecting or absorbing the photons of the background light. The free carriers absorb the laser energy and then thermalize within the electron-hole plasma. The excited carriers then relax and transfer the energy to the lattice through interaction with phonons.

The dynamic of the heat transfer mechanism can be described with the help of the two-temperature model under the assumption that the carriers experience fast thermalization so the carrier temperature is defined. The phenomenon is described by the following system of equations:

$$C_{e-h}(T_{e-h})\frac{\partial T_{e-h}}{\partial t} = \nabla(K_{e-h}\nabla T_{e-h}) - g(T_{e-h} - T_l) + S(z,t) \qquad (4.54)$$

$$C_l \frac{\partial T_l}{\partial t} = \nabla(K_l \nabla T_l) + g(T_{e-h} - T_l) \qquad (4.55)$$

where C_e, k_e, C_l, k_l, $T_{e\text{-}h}$, T_l, g, and S (z, t) are the heat capacity, the carriers' subsystem thermal conductivity, carriers' subsystem temperature, lattice temperature, carrier-phonon coupling constant, source term and represents the absorbed energy, respectively.

The coupling term $(T_{e\text{-}h}\text{-}T_i)$, in the case of ultrashort pulses, is positive while in the case of laser pulses longer than tens of picoseconds, it goes to zero.

Ablation occurs when the temperature of the laser spot area increases significantly in a faster time scale than required for the lattice. A high temperature gradient exists and repulsion pressure removes the material from the localized spot without affecting the neighboring area. If the laser pulse width is longer than a few picoseconds or the laser energy is between the melting and ablation's threshold, consecutive processes of heating, melting, and vaporizing take place.

CHAPTER 5

EXPERIMENTAL SETUPS

This chapter is devoted to outlining the experimental setups and procedures. The experimental work is divided into two main parts: investigation of single-pulse laser interaction mechanisms with semiconductors and micromachining application for MEMS. The first experimental part includes self-imaging measurements, two-photon absorption measurements and pump-and-probe measurements. The second part contains beam clean-up techniques, and micromachining setups.

The Ti-sapphire femtosecond laser (Spitfire from Spectra Physics) was used to conduct the experimental work of this dissertation. The laser system consisted of a seeding laser and regenerative amplifier. Both lasers were pumped with a 5 *W* frequency doubled diode laser and 20 *W* frequency doubled YAG laser respectively. The output of the femtosecond laser system provided pulses with the following specifications: 800 *nm* wavelength, 110 femtosecond pulse width, 2 mJ pulse energy and a repetition rate ranged from 1 to 1000 *Hz*. Unless differently mentioned in the experimental setup, the laser was used at 800 *nm* wavelength.

Optically polished silicon and gallium phosphate wafers were used in conducting the experimental work. The samples basic properties are illustrated in table 1.

Table 1: Basic properties of the experimentally used samples; Si and GaP [78, 81-84].

Material	Silicon (Si)	Gallium Phosphate (GaP)
Crystal structure	Diamond	Zinc Blende

Lattice constant A	5.431	5.4505
Melting point (°C)	1412	1457
Orientation	100	100
Type	n-type	n-type
Density (g cm^{-3})	2.33	4.13
Resistibility	<0.005 Ω/cm	<0.5 Ω/cm
Surface	Front side polish – back side etched	Front side polish – back side etched
Thickness (μm)	500	500
Band gap (eV)	1.124	2.26
Dielectric constant @ 800 nm	13.5 + i 0.028	9.11
Refractive index @ 800nm	3.675	3.02
Auger recombination coefficient	2.8 x 10^{-31} cm^6 sec^{-1}	~ 10^{-31} cm^6 sec^{-1}
Optical effective mass	0.12 m_e	0.22 m_e
Optical phonon energy (eV)	0.063	0.051
Electron affinity (eV)	4.05	3.8

5.1 FEMTOSECOND SELF-IMAGING

The material status during the interaction of single femtosecond laser pulses was studied by implementing a novel imaging technique. A fast electro-mechanical shutter (Uniblitz model VS14, Vincent Association) was used to control the number of laser pulses. For single pulse experiment, since the minimum exposure time of the shutter was

1.5 ms, the repetition rate of the laser was adjusted to make sure that only one single pulse was injected to the optical setup. The laser repetition rate adjusted to 10 *Hz* to insure stability of pulse energy and by adjusting the exposure time to 100 *msec*, the pulse selector enabled the usage of a single laser pulse in the experiment. A schematic diagram of the self-interaction imaging setup is shown in Fig. 5.1. The setup was based on monitoring the reflectivity change of the target surface during the pump pulse. The pump pulse was injected into the optical scheme, focused onto the sample surface then reflected back, and directed to the detector (Beam profiler system with Chou camera model 4615 from Spiricon), which was video-triggered as the intensity of the background increased by 5% or more. The pulse energies were continuously monitored by deflecting a fraction of the laser power to a fast rising detector (model DET110 from Thorlabs). An absorptive neutral density filter set (from CVI lasers) with variable transmission values was used in two positions of the setup alternatively to ensure that the detector would not respond to any intensity changes unless the optical properties of the sample surface changed due to the interaction with the pump pulse. The use of the neutral density filters made the detector sensitivity independent from the pump energy.

The neutral density filters were used first to attenuate the pump beam and to record reference intensity through the reflection of the beam from a non-perturbed sample surface. The filters were moved in order from the attenuation position to the second position in front of the detector and then by injecting another laser pulse and recording the reflected intensity. A computer controlled nano-mover X-Y stage of 10 *nm* resolution, +/- 1 μm accuracy and 2.5 *mm* /sec maximum speed (from Melles Griot) was used to ensure a fresh sample area for each laser exposure. Samples of n-type silicon wafer

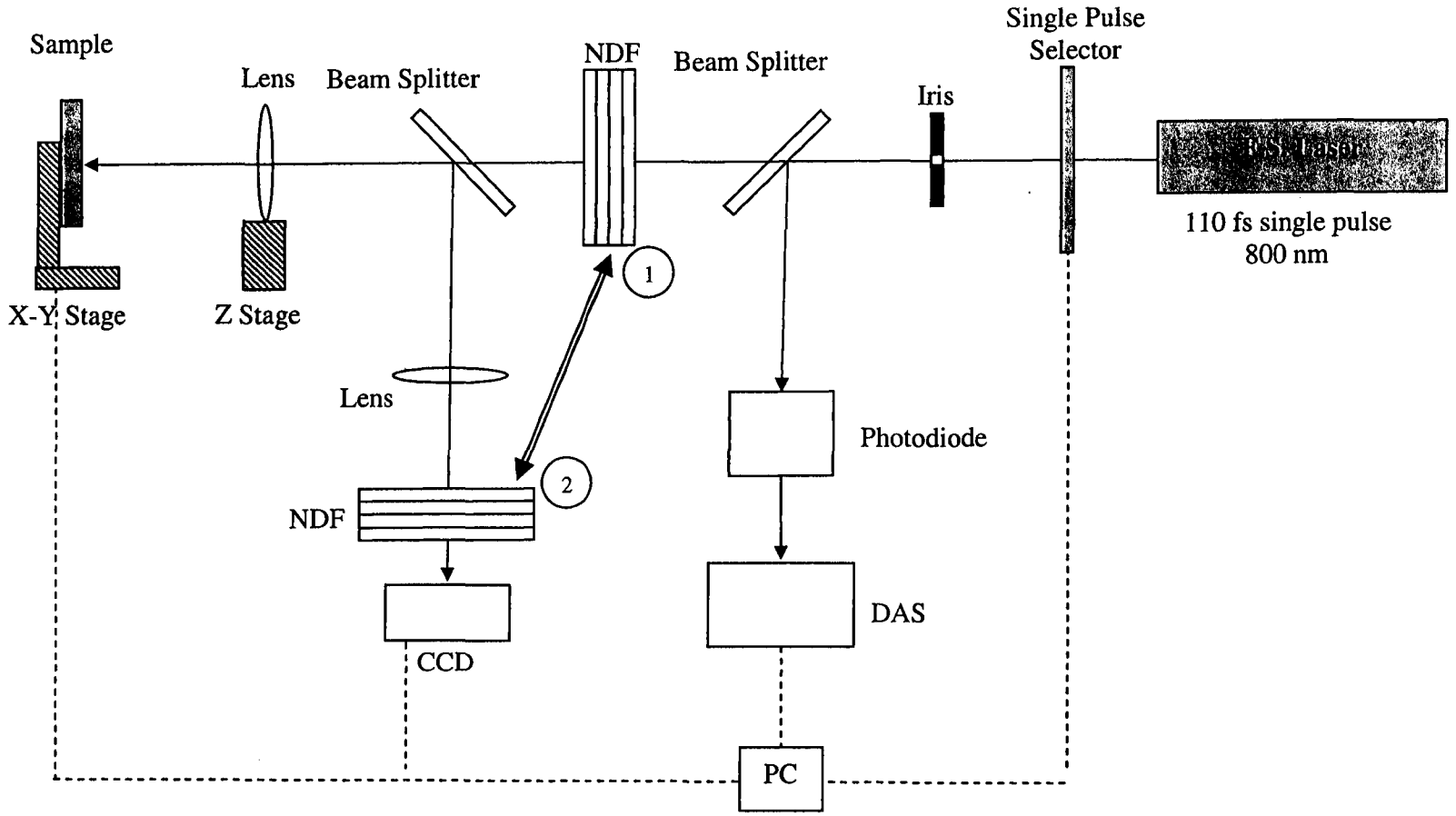

Figure 5.1: Femtosecond laser self-imaging experimental setup.

<100>, and gallium phosphate of 500 μm thicknesses and optically polished surfaces were used in the experiment. The samples were first cleaned using methyl alcohol and then attached to an optical flat substrate using silver paint. The setups alignment were checked and readjusted with every new sample.

A series of profile measurements that corresponded to different pulse energies were obtained. The intensity profiles were extracted using the camera software and were plotted using Micro-lab Origin software.

The dependence between the intensity profile changes and the pump laser pulse energy were obtained. The laser-exposed samples were checked with optical, electron and atomic force microscopy to observe the changes in the surface morphology, which corresponded with each laser pump energies.

5.2 TWO-PHOTON ABSORPTION

The dynamics of the two-photon absorption process were studied in the following two experiments. The first experiment investigated the temporal behavior of the material at a fixed laser excitation level using the pump and probe technique. The second experiment was devoted to investigate the material response at variable excitation levels as well as precise experimental determination of the two-photon absorption coefficient of gallium phosphate sample.

5.2.1 PUMP-AND-PROBE TECHNIQUE

Experimental studies of ultrafast two-photon interaction with gallium phosphate in the femtosecond time domain were performed. The laser was used in a single-pulse

mode in the optical arrangements shown in Fig. 5.2. The input laser power density was kept at 10^{11} W/cm^2. The probe beam represented 2% of the pump beam. In alignment mode, temporal overlap between the pump and probe beam was achieved by having equal intensities pump and probe beams, then overlapping the two beams focus spots on a frequency doubling crystal (LBO). Maximizing the second harmonic generation the LBO crystal was a sign of reaching the temporal overlap of the two beams. The BBO crystal was of 250-μm thickness and was cut at 28 degree. After adjusting the temporal overlap, at the same power ratio of pump and probe beams, the spatial overlap was achieved by carefully adjusting the steering mirrors on the probe arm.

A photo detector of 1 *ns* rising time (DET210 from Thorlabs) was used to measure the transmitted probe signal at different delay time after electronically triggered by the pulse selector controller.

Fresh sample areas were always achieved by moving the sample in the focal plane a few times the expected laser focus' spot. The detected signal was processed by the data acquisition system; then, the collected data was plotted as a function of delay time.

5.2.2 TWO-PHOTON ABSORPTION COEFFICIENT MEASUREMENTS

The single-pulse experimental setup was arranged, as shown in Fig. 5.3., to study the mechanism of the two-photon absorption process and to measure the two-photon absorption coefficient of gallium phosphate. An optically polished gallium phosphate sample of 500 microns thickness was used in conducting the experiment. Absorptive neutral density filters of transition values ranging between 1 to 90% were used. Using a fast computer-controlled pulse selector enabled performing the experiment in a single-

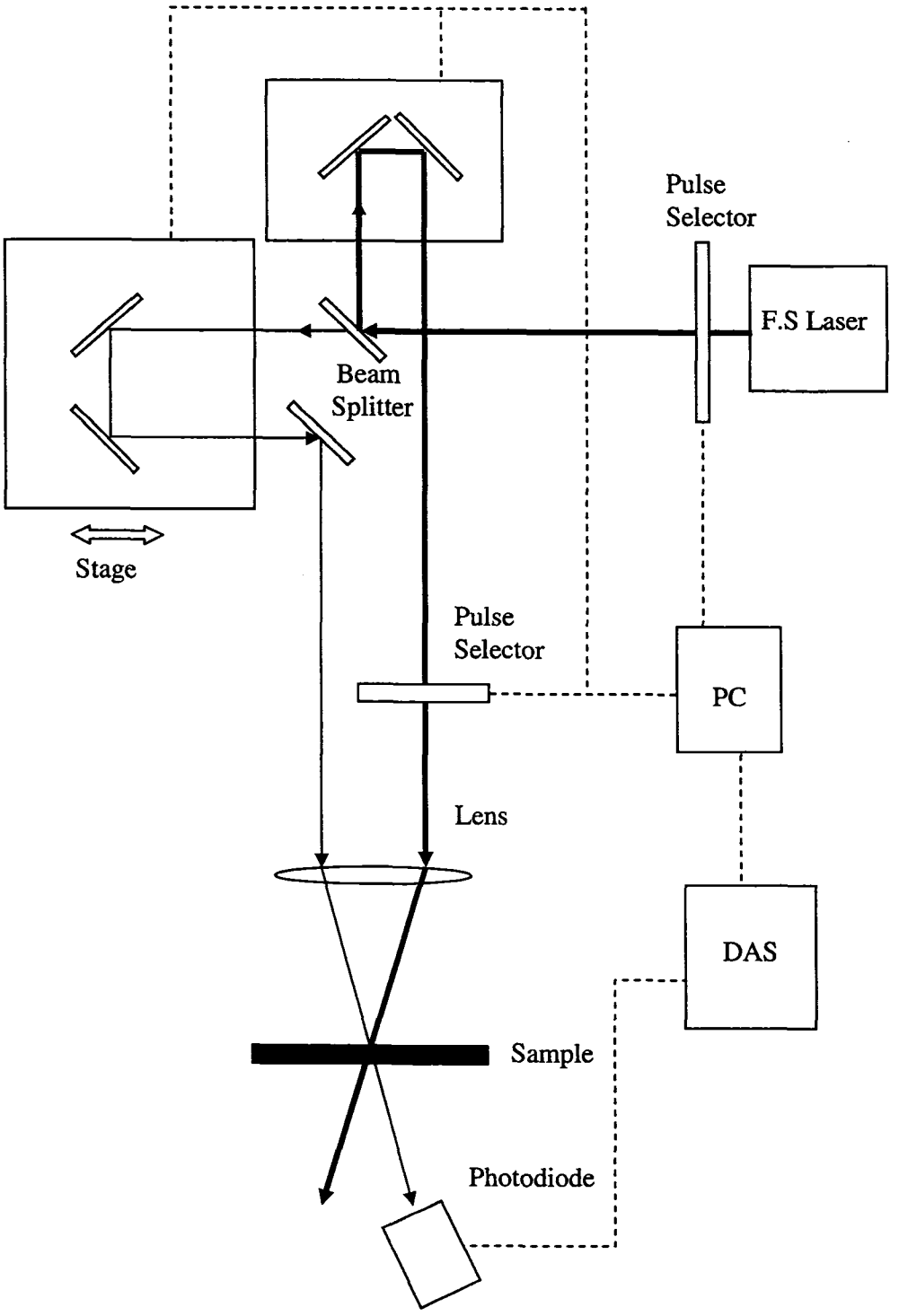

Figure 5.2: Pump and probe measurements experimental setup.

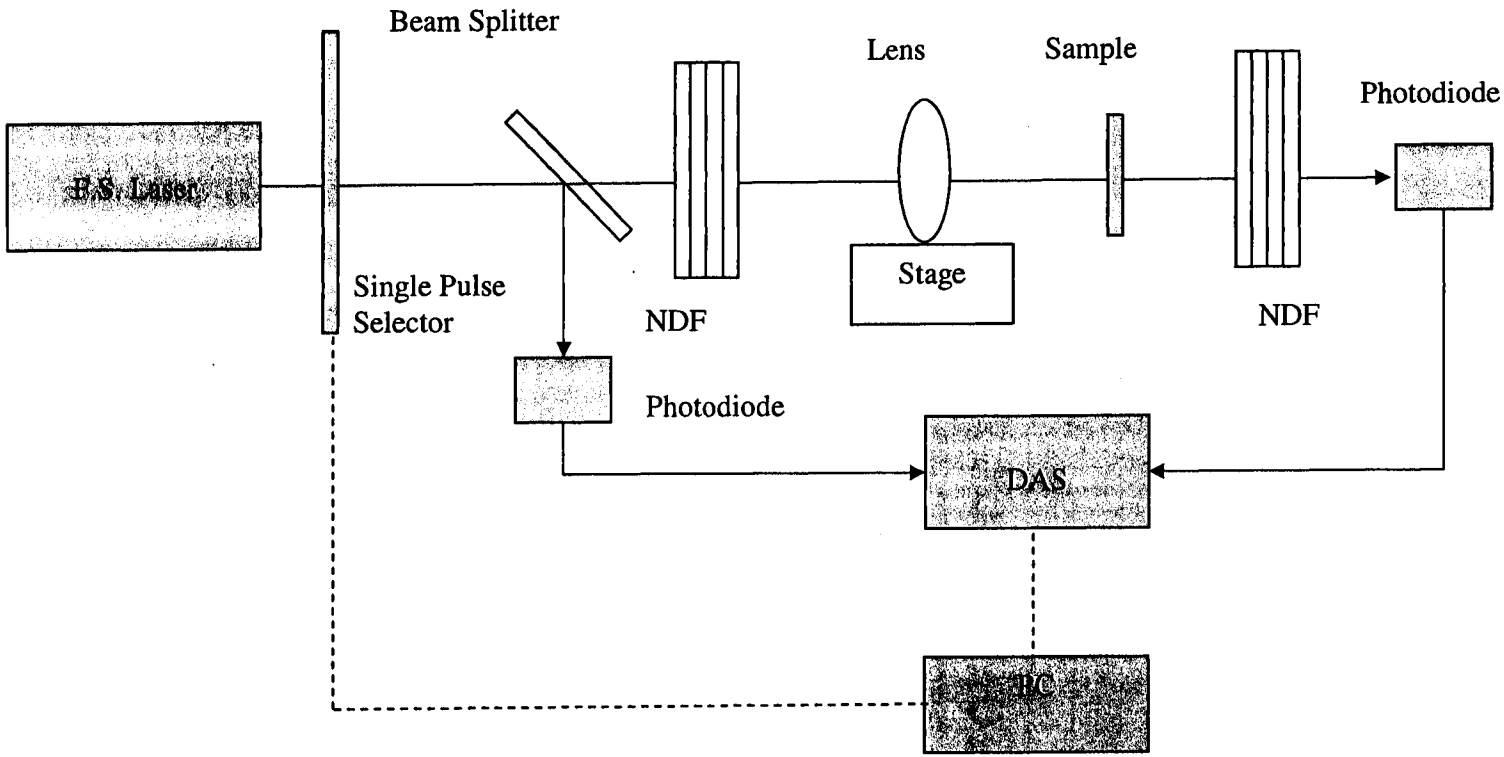

Figure 5.3: Two-photon absorption measurements experimental setup.

pulse mode. The pulse energy was continuously monitored using a fast-rising photodiode of 1 ns rising time. Two identical photodiodes were placed before and after the sample. The first photodiode monitored the input laser pulse energy while the second monitored the transmitted signal. The two photodiode sensors were kept at fixed position from the sample. A neutral density set was placed alternatively before and after the sample so that the detector after the sample sensed the real decrease in the pulse energy due to the sample absorption as a function of the laser pulse energy. The two photodiodes were connected to a data acquisition system (DAS from National Instrument). The first photodiode triggered the second photodiode to sense the response of the incident laser pulse. A convex lens of 100 mm was fixed on a micro-stage and was used to focus the laser beam on the sample surface. A fresh surface was always used when exposing the sample by moving the sample stage a few times of the expected focus spot to avoid any heat treatment history of the exposed spot. The ratio between the input and transmitted laser pulse energy was registered into a defined data file.

5.3 APPLICATION

Femtosecond laser fabrication of micro-electro mechanical systems was considered a direct application in this Dissertation. The application section was divided into two main parts; the first dealt with the laser beam profile treatments while the second dealt mainly with the direct micromachining. The micromachining setup was used to characterize the input laser beam and to run the experiment in different modes, namely, single and consecutive pulse modes.

5.3.1 LASER BEAM SPATIALLY RESHAPING

As the second part of the experimental setup dealt mainly with the application of femtosecond ablation in a MEMS fabrication field, it was very important to illustrate the setup used for cleaning up the laser beam profile. Two techniques were used to obtain a clean beam profile, as shown in Fig. 5.4. The first technique was based on spatially filtering the higher frequencies. In this technique, the beam was focused and re-collimated using two identical convex lenses of 40 cm focal lens. A pinhole made of copper was placed in the exact focal plane of the two telescopic lenses previously mentioned. The pinhole was fixed on an X-Y-Z stage for accurate adjustment of the pinhole position. Various pinholes of 50, 100, and 200 microns diameters were tested to optimize the laser output power and the spatial intensity profile. The beam profile corresponded with each of the previously mentioned pinholes and was observed with a CCD camera (model Chou 6415 from Spiricon). The CCD camera had a resolution of 5 μm.

An alternative cleaning-up technique was used by expanding the laser beam, using a 10X expander and then selecting an 8 mm diameter area to be the input of the machining experiment. The selectivity process was done while using the beam profiler for getting the best flat-top laser profile with no fluctuations or hot spots. The cleaning-up procedures were done after frequency doubled the laser beam to 400 *nm*. The laser beam power was controlled using neutral density filters for adjusting the experiment in the alignment mode.

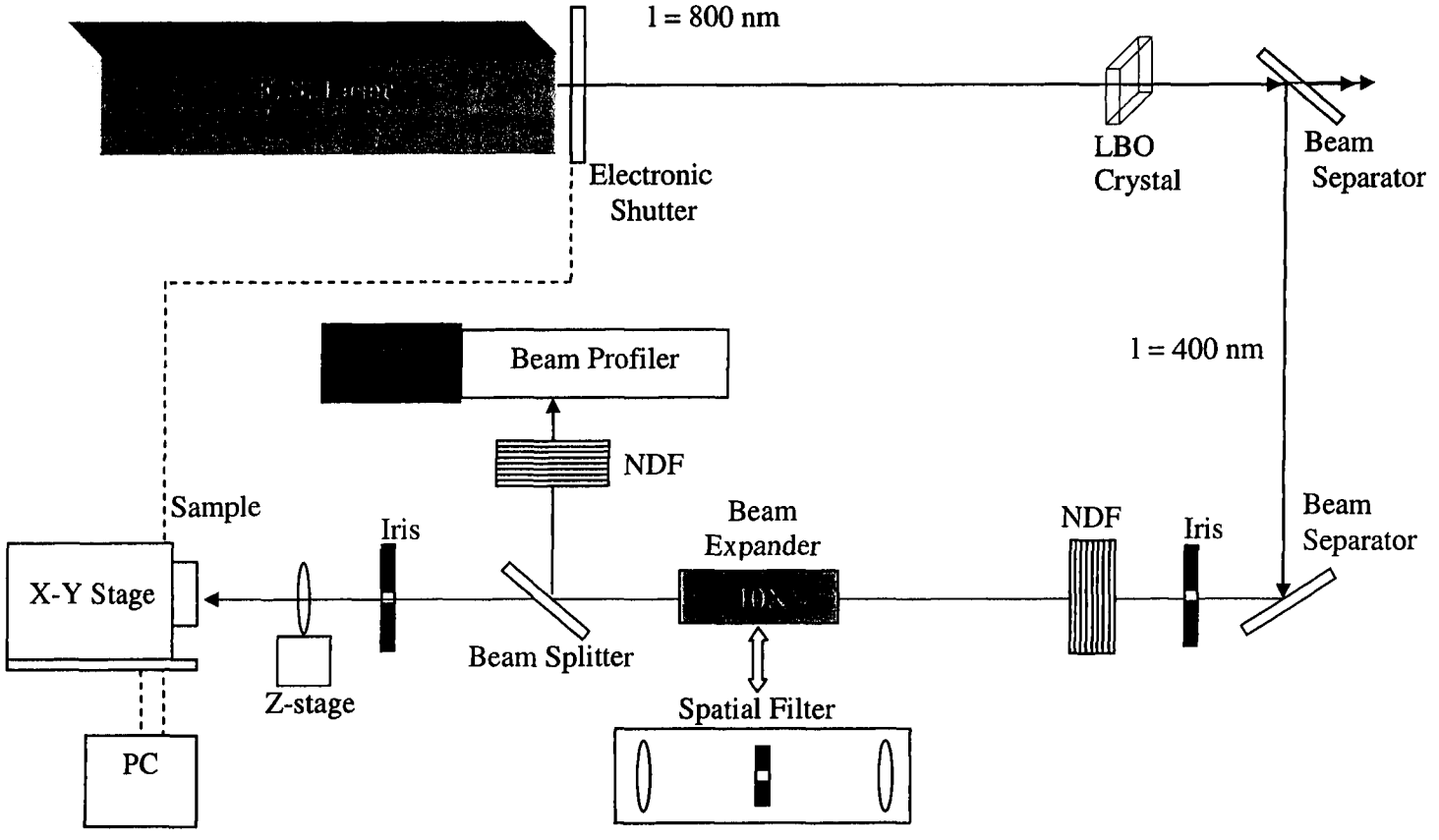

Figure 5.4: Beam clean-up techniques.

5.3.2 SINGLE PULSE ABLATION

Single-pulse ablation experiments were performed using the fundamental and doubled frequency femtosecond laser pulses. The experimental setup is shown in Fig. 5.5. Variable laser pulse energy was achieved using set of absorptive neutral density filters. Adjusting the exposure time of the pulse selector and the laser repetition rater enabled the experiment in the single-pulse mode. An F-theta lens of 100 mm focal lens was used to focus the laser beam on the sample surface at normal incident angle. A fresh sample area was used in each laser exposure. The experiment was done in air. The sample was pre-cleaned using methyl alcohol. No post-cleaning was required. The ablated spots were tested using different types of microscopy, such as atomic force, electron scanning and optical microscopy.

5.3.3 MULTIPLE PULSES ABLATION

The setup shown in Fig. 5.5. was used to perform a multiple-pulse ablation on silicon and gallium phosphate wafers with a thickness of 500 microns on an optically polished surface. The laser was focused on the sample using a 100 mm cylindrical lens. The laser energy density was 0.75 J/cm^2.

Multiple pulses were delivered to the sample using a computer-controlled fast electronic pulse selector. The sample was moved after each exposure to ensure a fresh area for the next exposure. The sample was examined using ESM.

5.3.4 SILICON MICROMACHINING FOR OMEMS

Laser micromachining of silicon for MEMS devices was studied using the setup

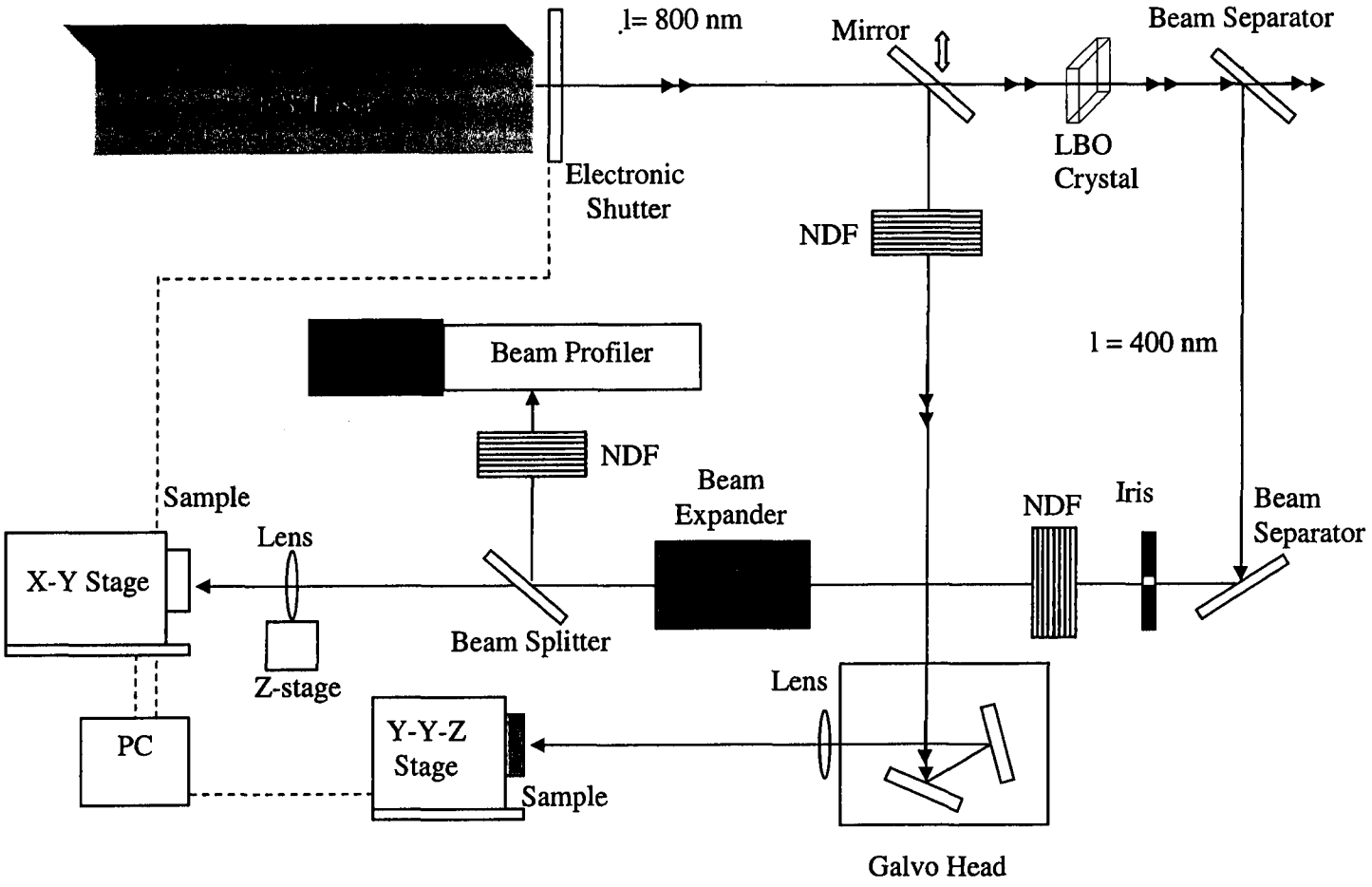

Figure 5.5: Micromachining setup.

shown in Fig. 5.5. A frequency doubling crystal (LBO Lithium Triborate -LiB_3O_5) of 250 μm thickness was used to double the fundamental frequency of the 800 *nm* femtosecond laser pulses. Fundamental and second harmonic beams were separated using a beam separator having 95% reflectivity at 400 *nm* and 1% reflectivity at 800 *nm*. The use of two beam separators decreased the ratio between the fundamental and second harmonic beams to $\sim 10^{-3}$, avoiding damage to the sample surface. Beam power was controlled using neutral density filters. The incident beam was expanded using a 10X beam expander and was focused using a 0.65 NA objective lens. The lens was mounted on a Z translation stage of μm resolution and was moved along the optical axis of the laser beam. A 500 μm thick <100> n-type silicon wafer was mounted on a computer-controlled X-Y stage capable of a 10 *nm* resolution. The sample scanning speed was fixed at 100 μm/sec to ensure that the overlapping of the beams was approximately 85%. A beam splitter was placed before the objective lens to continuously sample the laser beam profile. The laser-micromachined samples were cleaned ultrasonically for 30 minutes. An optical microscope capable of 500X magnification was used to evaluate the width and the edge quality of the micromachined lines. To achieve higher precision, an AFM was used to evaluate line quality, depth, and width of lines. A He-Ne laser was used to characterize the diffraction properties of the micromachined periodical structures, as shown in Fig. 5.6.

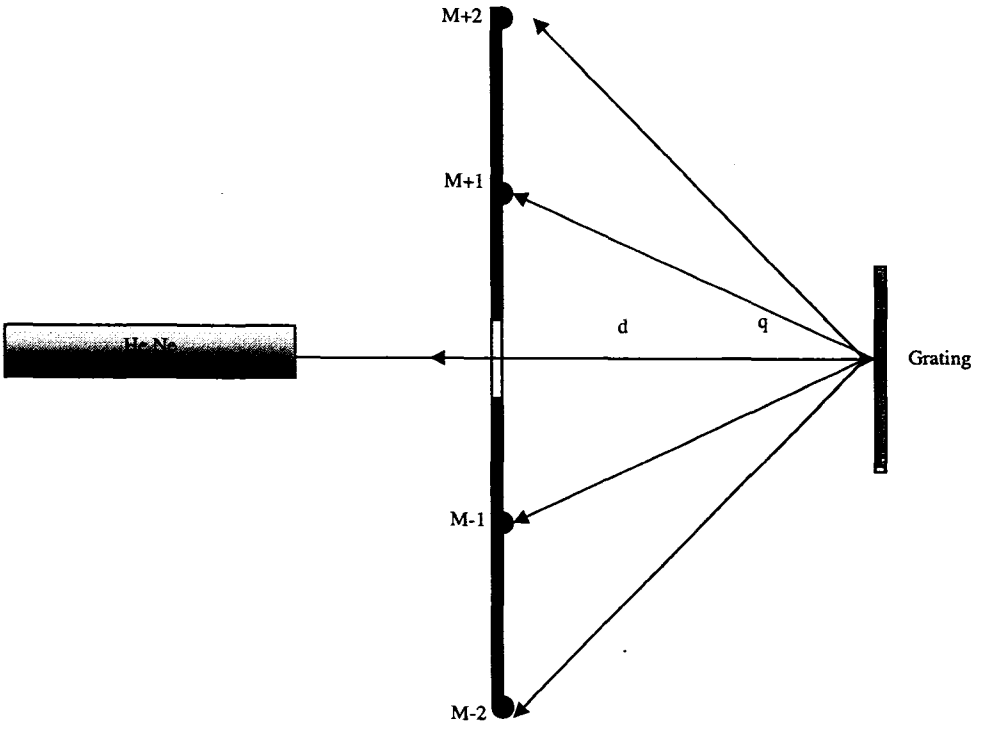

Figure 5.6: Optical testing for OMEMS machined devices.

CHAPTER 6

RESULTS AND DISCUSSIONS

6.1 SELF-IMAGING MEASUREMENTS

The material status during the interaction with single femtosecond laser pulse was theoretically predicted, and then experimentally investigated. The experimental results were compared with the theoretical predictions.

When a laser pulse interacts with matter, one would expect that if the ablation process were taking place during the incident laser pulse, the ablation would be observed either through the scattered light in the focal plane or a decrease in the reflectivity of the material as the ejected micro-particles increase the material absorption. The light intensity transmitted through the cloud is given by

$$I_t = I_0 \exp[-2\sigma_{ext}(\lambda)NL] \tag{6.1}$$

where I_0 is the incident intensity, N is the density of the spherical particles, L is the thickness of the absorbing region, σ_{ext} is the extinction cross-section.

According to Mie scattering theory, the optical density of the cloud of silicon droplets (conductive, absorbing spheres) can be written as

$$2\sigma_{ext}(\lambda)NL = \frac{4\pi l}{\lambda}\left[-3\pi \,\mathrm{Im}\frac{m^2-1}{m^2+2} + 2\left(\frac{2\pi a}{\lambda}\right)^3\left|\frac{m^2-1}{m^2+2}\right|\right]^2 \tag{6.2}$$

where $m = n + ik$ is the complex index of refraction of micro-particles, a is the micro-particle radii, l is the depth of material removed from the surface. Nevertheless, there was no evidence of absorption during the interaction of the laser pulse with both silicon and

gallium phosphate. On the other hand, reflectivity went up twice its value of fresh surface as will be discussed later in this chapter.

The absence of absorption in addition to the reflectivity jump might be related to a free carrier generation phenomena. The dielectric constant at frequency ω for *e-h* plasma density N is described by Drude model [84]:

$$\varepsilon = \varepsilon_0^{'} + i\varepsilon_0^{''} - \frac{Nq^2}{\mu(\omega^2 + i\omega/\tau_D)} = (n+ik)^2 \tag{6.3}$$

where τ_D is the Drude damping time, N is the plasma density, q is the electron charge, $\varepsilon_0^{'} + i\varepsilon_0^{''}$ is the dielectric constant at frequency ω, and μ is the effective mass.

For silicon, all the above parameters (except for Drude time) are approximately known even for high-density plasma. Dividing the real and imaginary parts of (6.3) gives the following two equations:

$$\varepsilon_0^{'} - \frac{N \cdot q^2}{\mu \cdot \left(\omega^2 + \frac{1}{\tau_D^2}\right)} = (n^2 - k^2) \tag{6.4}$$

$$\varepsilon_0^{''} + \frac{N \cdot q^2}{\mu \cdot \tau \cdot \left(\omega^3 + \frac{\omega}{\tau_D^2}\right)} = 2 \cdot n \cdot k \tag{6.5}$$

Solving (6.4), (6.5) yield to real and imaginary parts of the refractive index as following:

$$n^2 = \frac{(a-b) + \sqrt{(a-b)^2 + (c+d)^2}}{2} \tag{6.6}$$

$$n = \sqrt{\frac{(a-b) + \sqrt{(a-b)^2 + (c+d)^2}}{2}} \tag{6.7}$$

$$k^2 = -a + b + \frac{(a-b) + \sqrt{(a-b)^2 + (c+d)^2}}{2} \tag{6.8}$$

where $a=\varepsilon_0^{'}$, $b=\dfrac{N\cdot q^2}{\mu\left(\omega^2+\dfrac{1}{\tau_D^2}\right)}$, $c=\varepsilon_0^{''}$, $d=\dfrac{N\cdot q^2}{\mu\cdot\tau\cdot\left(\omega^3+\dfrac{\omega}{\tau_D^2}\right)}$

Reflectivity can be written in terms of the refractive index and the extinction coefficient as following

$$R=\frac{(n-1)^2+k^2}{(n+1)^2+k^2} \tag{6.9}$$

Substituting from (6.6), (6.8) into (6.9)

$$R=\frac{\left[\dfrac{(a-b)+\sqrt{(a-b)^2+(c+d)^2}}{2}-1\right]^2+\left[-a+b+\dfrac{(a-b)+\sqrt{(a-b)^2+(c+d)^2}}{2}\right]^2}{\left[\dfrac{(a-b)+\sqrt{(a-b)^2+(c+d)^2}}{2}+1\right]^2+\left[-a+b+\dfrac{(a-b)+\sqrt{(a-b)^2+(c+d)^2}}{2}\right]^2} \tag{6.10}$$

Reflectivity as a function of free carrier density could be plotted using (6.10) at various Drude damping times for both silicon and gallium phosphate as shown in Figs 6.1 and 6.2. Both graphs 6.1 and 6.2 exhibit similar behavior with a slight shift in the plasma resonance value. The plasma resonance appears at the excitation of 15 % and 20% of the valance electrons in case of silicon and gallium phosphate respectively.

The experimental study of the problem was performed at various laser pulse energies with maximum energy density of 5 J/cm^2. The selected range of energy density was not explored in previous publications concerned with this physical problem.

The reflectivity was probed during the incident laser pulses at various energies. The differences in reflectivity before and during the femtosecond laser pulses corresponded to the changes of the material status.

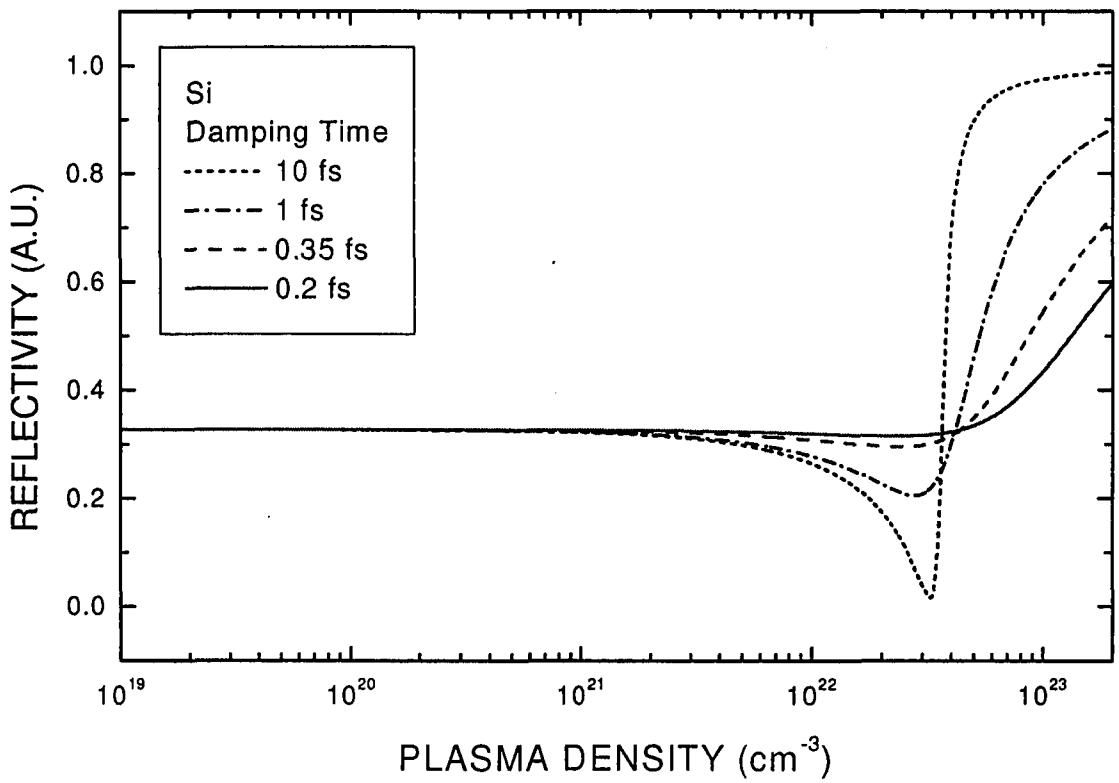

Fig 6.1: Theoretical expectation for reflectivity of silicon as a function of generated electron-hole plasma density at various damping times. $\lambda = 800$ nm, $m_{opt} = 0.12\ m_e$ [84], $\varepsilon_0' = 13.5$, $\varepsilon_0'' = 0.028$ [81].

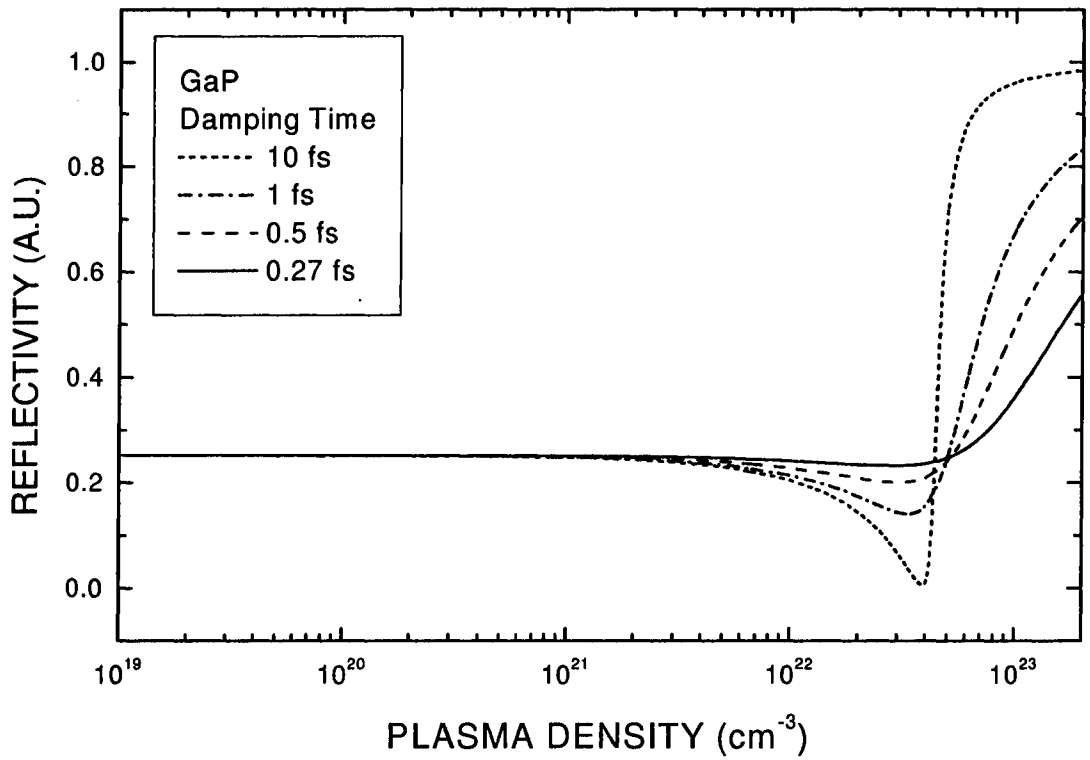

Fig 6.2: Theoretical expectation for reflectivity of gallium phosphate as a function of generated electron-hole plasma density at various damping times. $\lambda = 800$ nm, $m_{opt} = 0.22\ m_e$, $\varepsilon'_0 = 9.11$, $\varepsilon_0'' = 0$ [82].

A non-perturbing single laser pulse hit the sample surface, and then reflected to a detector for intensity measurement. An optical scheme was arranged in such way that the intensity detector would not record any intensity changes of the reflected beam, despite the incident laser energy density, unless the sample surface had a change of its optical properties during the injected laser pulse.

Intensity distributions of reflected laser pulses at various energy densities in case of silicon and gallium phosphate samples are shown in Figs. 6.3 and 6.4, respectively.

The measured intensity profile of the reflected laser pulse in both silicon and gallium phosphate cases were directly proportional with the incident laser energy density. The peak amplitudes were extracted from Figs 6.3 and 6.4 and then plotted against the corresponding incident pulse energy density for both silicon and gallium phosphate as shown in Fig. 6.5 and 6.6 respectively. The material optical response in Fig 6.5 and 6.6 can be divided into three regions. The first region represented a constant function. At this region the reflectivity of both silicon and gallium phosphate were equal to their reflectivities at the solid state form of the material. This region ended at maximum laser energy densities of 1.15 J/cm^2 for silicon and 0.4 J/cm^2 for gallium phosphate. The second region was a fast rising reflectivity directly proportional with the laser energy density, followed by a saturation region. The turning energy density points from rising regime to the saturation regime were 2.8 J/cm^2, 1.7 J/cm^2 for both silicon and gallium phosphate respectively.

There was no observation for any absorption during the femtosecond pulse in silicon or in gallium phosphate cases. On the other hand, the reflectivity increased twice the starting value of the samples, which was connected with free carrier generation.

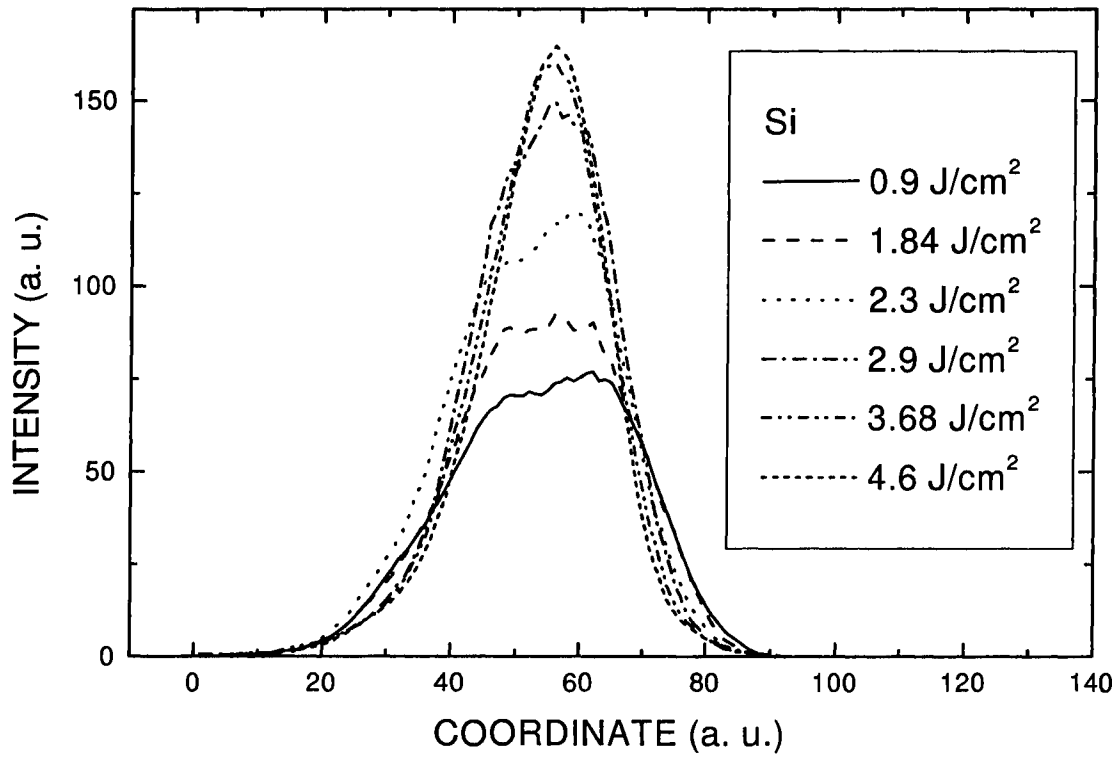

Fig 6.3 : Intensity cross-section of reflected single laser pulse from optically polished silicon surface <100> at six different laser fluencies. Self-imaging technique (zero delay). Pulse width = 110 fs, λ = 800 nm.

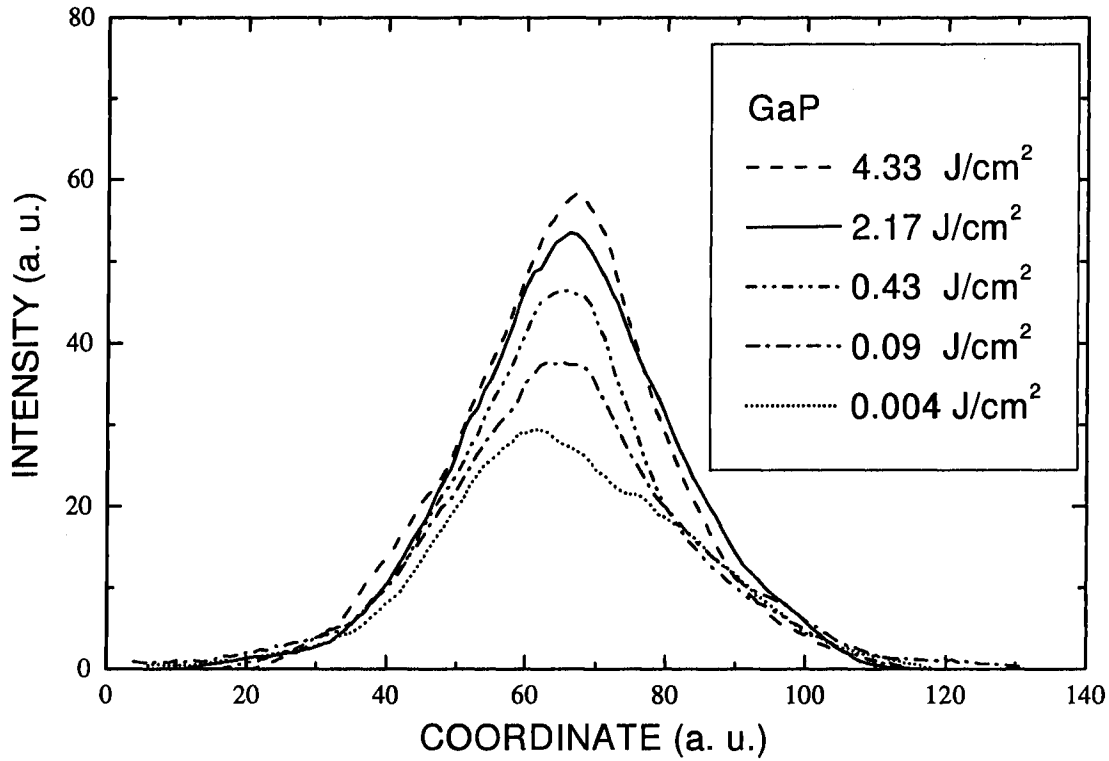

Fig 6.4: Intensity cross-section of reflected single laser pulse from optically polished gallium phosphate surface at six different laser fluencies. Self-imaging technique (zero delay) Pulse width = 110 fs, $\lambda = 800$ nm.

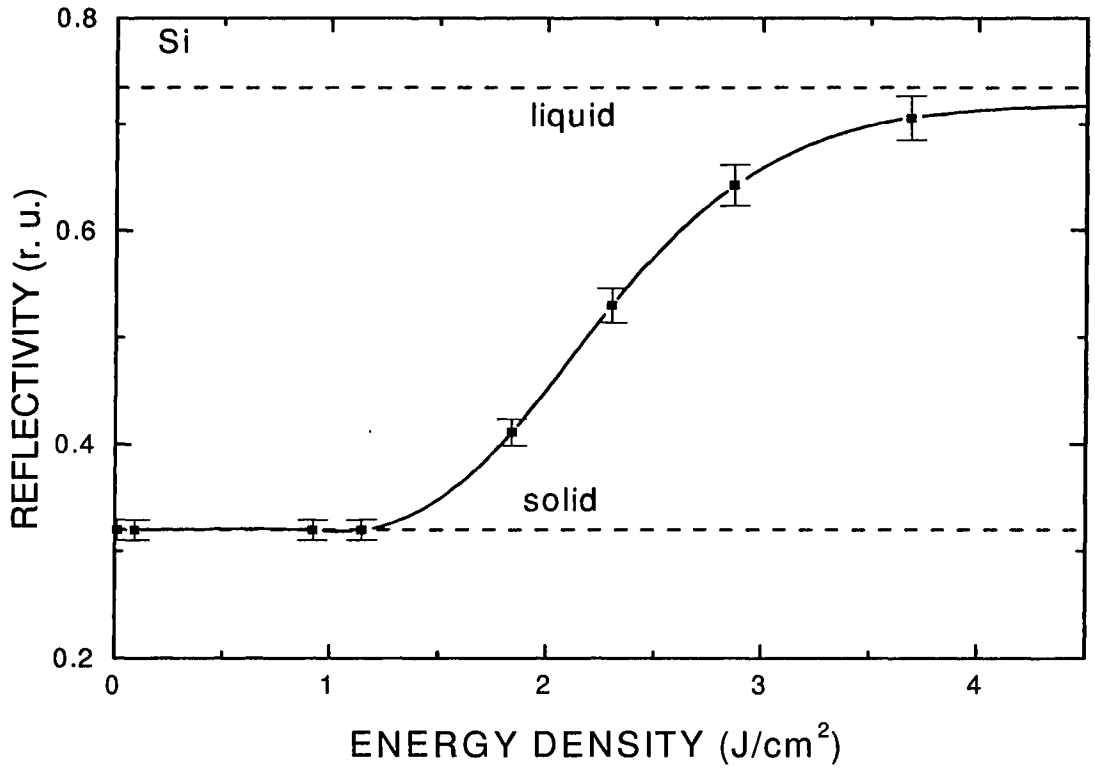

Fig 6.5: Reflectivity of silicon as a function of laser energy density. Single pulse measurements with no delay time. Pulse width = 110 fs, λ = 800 nm. Solid squares are the experimental data, while the solid curve is the best fit. The upper and lower dashed lines represent the reflectivities of liquid and solid silicon, respectively.

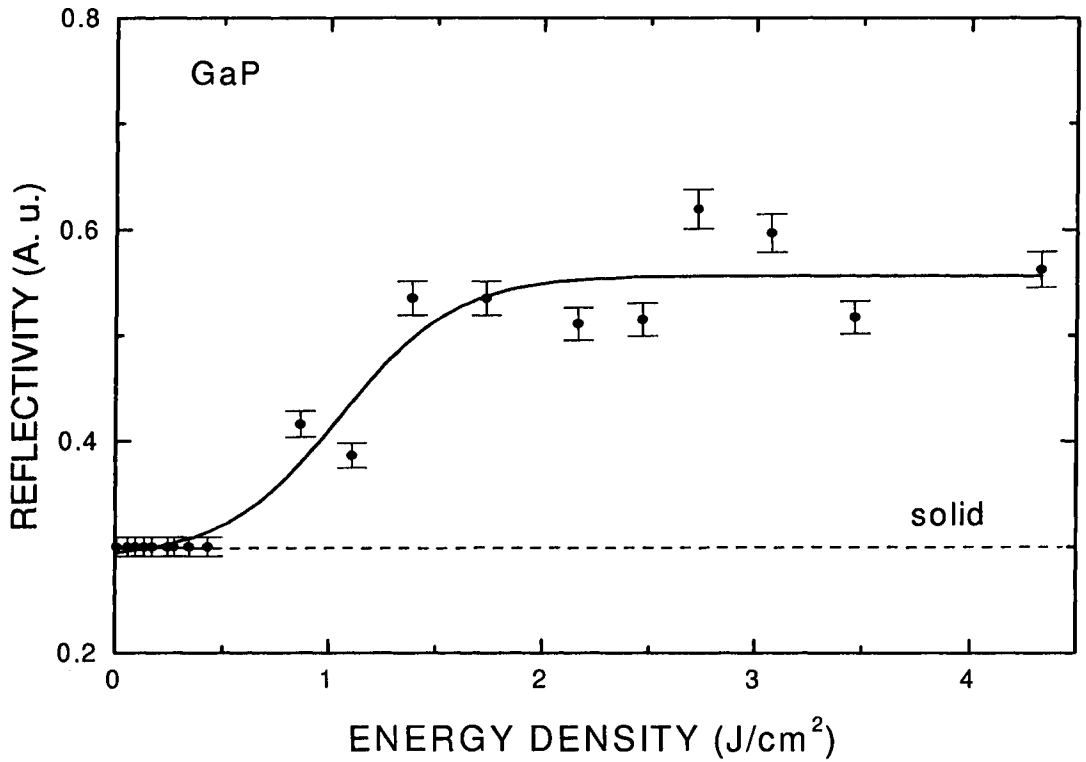

Fig 6.6: Reflectivity of gallium phosphate as a function of laser energy density. Single pulse measurements with no delay time, pulse width = 110 fs, λ = 800 nm. Solid squares are the experimental data, while the solid curve is sigmodial fit. The upper and lower dashed lines represent the reflectivities of liquid and solid gallium phosphate, respectively.

Auger recombination process is an effective mechanism that prevents reaching high density generated plasma. Calculating Auger recombination time (τ_A) for plasma density in the range of 10^{21} cm^{-3} was straight forward as the recombination coefficient is known at this density (2.8 x 10^{-31} cm^6 s^{-1} for Si, and 10^{-31} cm^6 s^{-1} for GaP). Knowing that $\tau_A = (CN^2)^{-1}$ where C is the Auger recombination coefficient and N is the plasma density, one could calculate τ_A. At N = 10^{21} cm^{-3}. τ_A = 3.5 *ps* for silicon and 10 *ps* for gallium phosphate. Calculation of Auger time at higher plasma densities ($N \geq 10^{22}$ cm^{-3}) gives inaccurate values as the reported values for C does not apply [84].

At plasma density > 10^{22} cm^{-3}, the laser pulses tend to have a shallow absorption depth in the range of few hundred angstroms, and consequently much higher plasma density could be reached with much longer effective Auger recombination time than low density case [84].

The previously mentioned experimental observation means two things; firstly, Auger recombination time was much longer than the laser pulse, secondly, the generated electron-hole pairs did not move during the pulse width.

The theoretical predictions in Figs 6.1, 6.2 confirmed the obtained experimental results presented in Figs 6.5 and 6.6 for both silicon and gallium phosphate respectively. Comparing the theoretical and the experimental data suggested that, the Drude damping time equal to (0.35 x 10^{-15} *s*) for silicon and (0.27 x 10^{-15} *s*) for gallium phosphate. The obtained Drude damping time is a good match with the results reported in [74, 78, 84].

The excitation of semiconductor samples, either silicon or gallium phosphate, can be understood as follows: the laser leading edge of the pulse hits the fresh sample, creating dense electron-hole plasma in a narrow penetration depth (~ 15 μm for silicon

and few hundred microns for gallium phosphate see Figs 6.7, 6.8). The generated plasma exhibits an exponential distribution profile over the absorption depth. With the pulse still irradiating the material, the absorption depth gets narrower and the plasma density gets higher until reaching the plasma resonance. At plasma resonance, the real part of the dielectric constant turns to a negative value and the pulse is absorbed in a narrow absorption depth of the range of hundreds of angstrom. The plasma density that is generated grows higher than the plasma resonance, very close to the material surface and the reflectivity of the material increases as for metals, perhaps twice as much its value for fresh surface.

Consider that the lattice relaxation occurs through two different relaxation mechanisms; the first is the collision between plasma carriers themselves, while the second is due to the collisions between the carriers and the atoms of the lattice. The first mechanism occurs in the time domain of 10^{-16} s while the second occurs in the time domain of 10^{-11}-10^{-13} s depends of the material. The electron-electron collision or hole-hole collisions in the first relaxation process does not result any damping and conserve the momentum of the two electrons or the two holes. The damping results from collisions between the electrons and the holes of the plasma. The electron-hole damping time is expected to be inversely proportional with the plasma density.

The effective relaxation time could be written as the follows:

$$\frac{1}{\tau} = \frac{1}{\tau_{ph}} + \frac{1}{\tau_{eh}} \qquad (6.11)$$

Where τ_{eh} is the electron-hole relaxation time and τ_{ep} is the electron-phonon relaxation time. For $\tau_{eh} = 10^{-16}$ s, $\tau_{eh} = 10^{-13}$ s the effective relaxation time ~ 10^{-16} s. This is perfectly

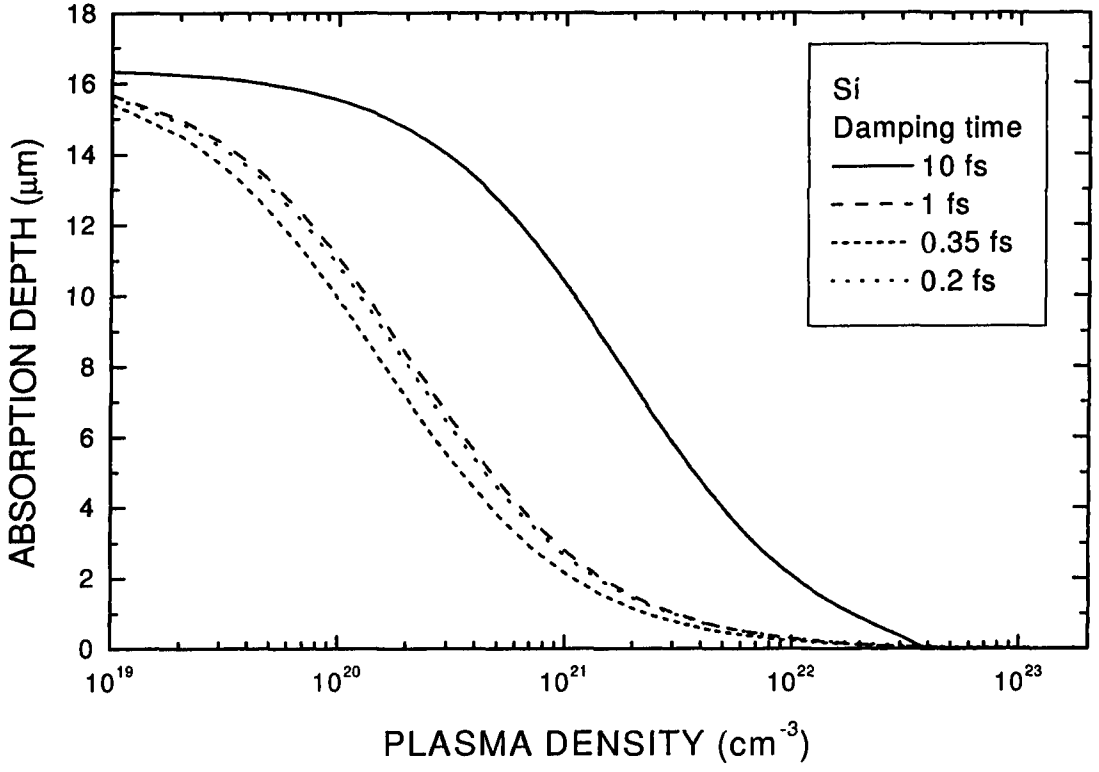

Fig 6.7: Theoretical expectation for absorption depth of silicon as a function of generated electron-hole plasma density at various damping times. λ = 800 nm, m_{opt} = 0.12 m_e [84], ε'_0 = 13.5, ε_0" = 0.028 [81]. Absorption depth = $\frac{\lambda}{4 \cdot \pi \cdot k}$.

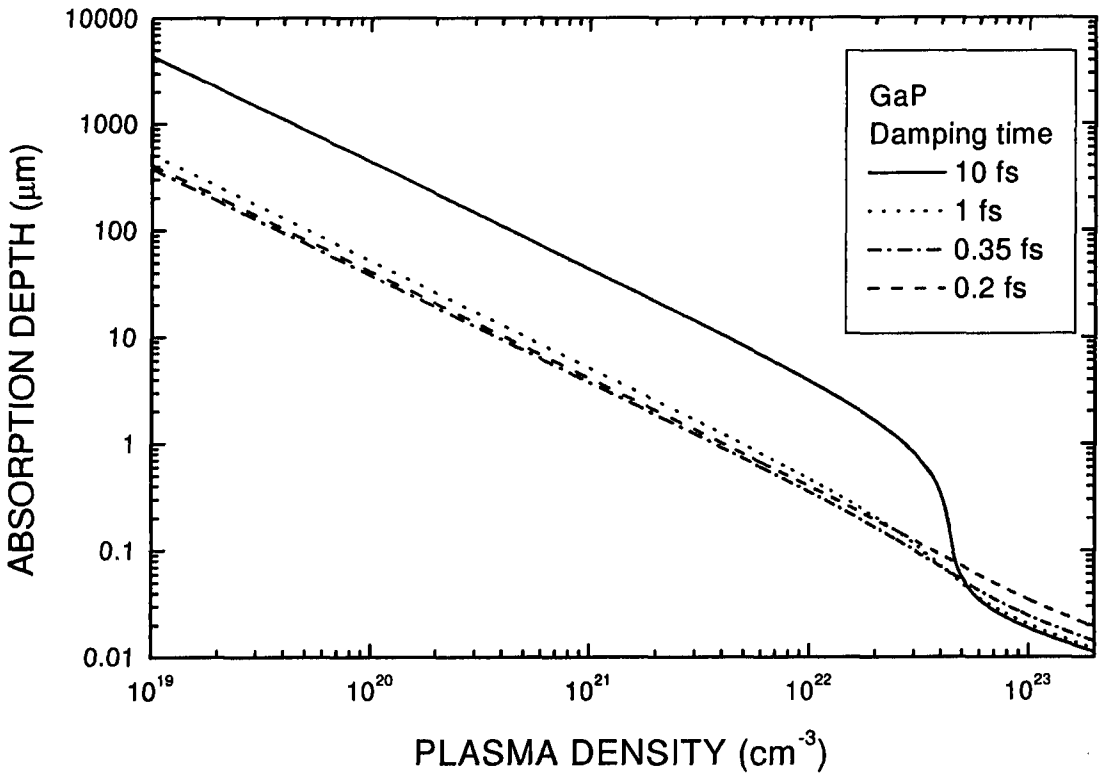

Fig 6.8: Theoretical expectation for absorption depth of gallium phosphate as a function of generated electron-hole plasma density at various damping times. $\lambda = 800$ nm, $m_{opt} = 0.22\ m_e$, $\varepsilon'_0 = 9.11$, $\varepsilon_0'' = 0$ [82]. Absorption depth $= \frac{\lambda}{4 \cdot \pi \cdot k}$.

matching with our experimentally obtained results for both silicon and gallium phosphate.

In another observation regarding the reflectivity results of silicon and gallium phosphate, it is shown that, higher reflectivity fluctuation was observed in the case of gallium phosphate than in the case of silicon, particularly in the saturation region. This fluctuation in the saturation region resulted from the probability of the non-linear excitation process of the gallium phosphate versus the linear excitation of the silicon samples. The reflectivity changed by factors of two from the steady region to the saturation region in both cases of silicon and gallium phosphate. The reflectivity jump from the steady region to the saturation region in case of silicon and gallium phosphate were matching with the increase of material reflectivity when its status changed from solid to liquid state.

6.2 PUMP AND PROBE MEASUREMENTS

The dynamics of induced absorption have been measured by a pump-probe technique. A gallium phosphate sample of 500 μm with an optically polished surface was used in the experiment. The ratio between the probe and pump beam energies were kept at 1:50 with pump intensity of 10^{11} *W*. Figure 6.9 shows the material response versus the delay time between pump and probe beams. The obtained curve can be divided into three designative regions; at the first region, a constant transmission followed by sharp decrease reaching to the minimum point at delay time equal zero then start to increase again then saturates at a delay time of about 150 femtosecond. The dots in Fig 6.9 represent the experimental data, while the solid line represents the theoretical response

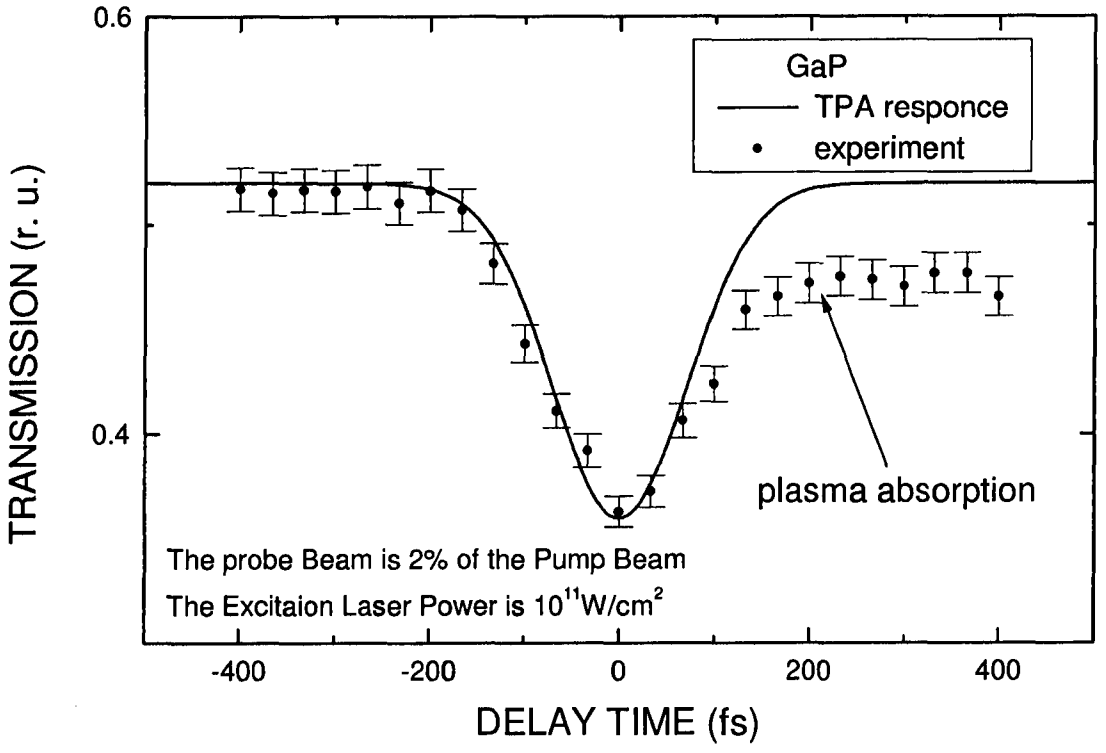

Fig 6.9: Transmission of gallium phosphate as a function of delay time, λ = 800 nm, pulse width = 110 fs, incident angle = 5 deg. The solid circles are the experimental data, while the solid curve represents the theoretical response of the two-photon absorption.

of the two-photon absorption.

As it is seen the results of transmission measurements corresponds exactly to correlation function of pump and probe pulses

$$T(\tau) \sim \int_{-\infty}^{\infty} I_{pump}(t) I_{probe}(t-\tau) dt \qquad (6.12)$$

with intensity profile $I \sim I_0 \cdot \mathrm{sech}^2 (1.8t/\tau_p)$, τ_p pulse duration at FWHM.

This means that the induced absorption results from instant absorption process which in the experimental conditions ($E_g/2 < \hbar\omega < E_g$) is solely two-photon absorption. One feature can be seen at the tail of the nonlinear response (positive delay time region) which is the slow decaying absorption. Evidently the absorption of free carriers (electrons and holes) account for slow response. Therefore, the main conclusion is that the fs-pulse excitation of GaP is achieved due to two-photon absorption process.

6.3 TWO-PHOTON ABSORPTION MEASUREMENTS

To further identify the absorption process and to determine the its numerical characteristics, the self-absorption measurements were performed. The experimental setup is shown in Fig 5.3. The purpose of the experiment was to describe the transmission dependence of fs-pulse as a function of pulse intensity and to compare the dependence with that found theoretically:

$$T(I_0) = \frac{2(1-R)}{d_0 \beta I_0 \pi^{1/2}} \int_0^{\infty} \ln(1+\beta I_0 (1-R) d_0 \exp(-x^2)) dx \qquad (6.13)$$

where, R =0.27 is the reflectivity coefficient $d0$ = 0.5 mm is the sample thickness β is the coefficient of two-photon absorption

Figure 6.10 illustrated the material response in terms of optical transmission function of laser peak intensities. The material response could be divided into three stages. The first stage presented constant transmission value, the second was a linear region and the third represented a deviation of the experimental results from the expected theoretical calculations. An agreement between experimental and theoretical results in Fig. 6.10 took place up to a point at which the peak intensity equal to $1GW/cm^2$. The most adequate numerical fit is presented in Fig 6.10 for two-photon absorption coefficient of $\beta = 0.2\ GW/cm^2$. It is worth to notice good correspondence between the value obtained and that found in independent studies [79]. Meanwhile the departure of the data obtained from theoretical dependence is clearly seen in Fig 6.10. Two reasons can be assigned to be responsible for the deviation. First, it is self-defocusing of fs-pulse due to negative contribution of plasma-induced refractive index. Second, it is free carrier absorption which contribution to induce absorption was neglected in theoretical analysis.

6.4 BEAM SPATIAL PROFILE CHANGE

As the spatial beam profile represented an important factor in the micromachining process, a set of experiments was performed to clean up the laser beam. The output laser beam usually experience deformation in its intensity profile due to many reasons. Some of these reasons are defects in optical elements inside the laser system, dust and particles in air. This results in scattering, picking up higher modes as well as spatial noise [63]. Suppressing the noise and maintaining smooth beam profile can be done either by spatially filtering the beam or by modifying the profile to get a step like profile (top hut) with minimal fluctuations. Figure 6.11 illustrates the intensity cross-section of the laser

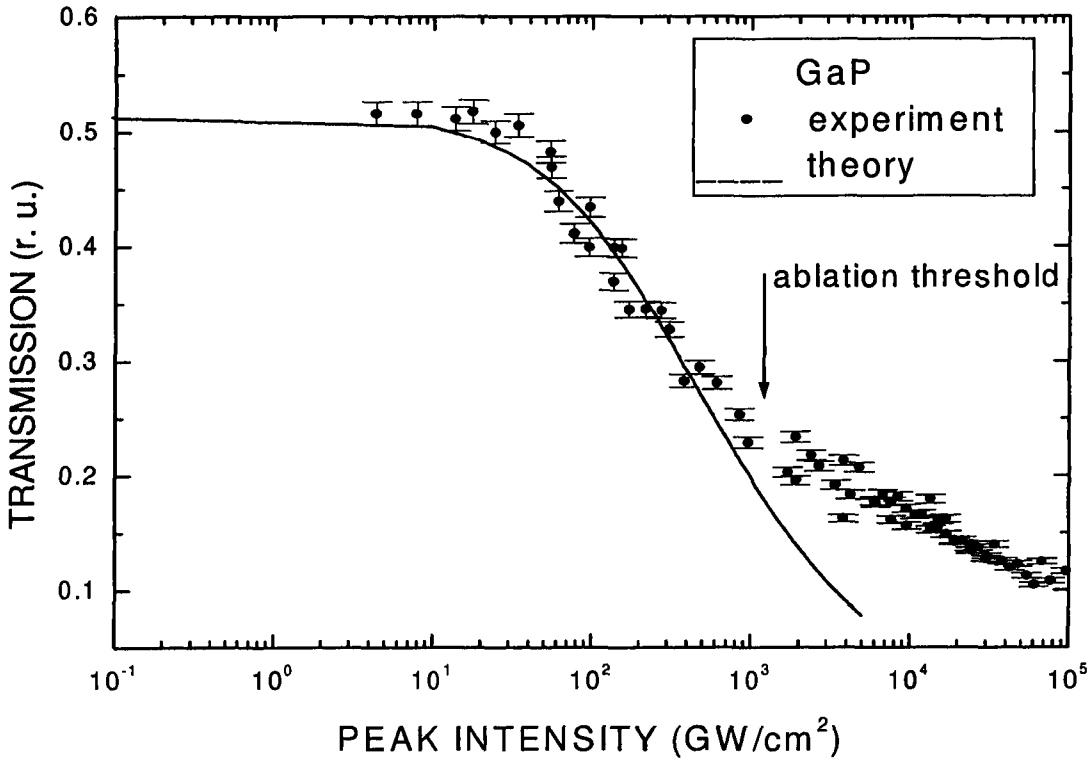

Fig 6.10: Transition of gallium phosphate as a function of peak intensity laser energy density. Single pulse measurements with no delay time, pulse width = 110 fs, λ = 800 nm wavelength. Solid dots are the experimental data, while the solid curve is the theoretical response as obtained from numerical integration of equation (6.6). The calculation parameters are R =0.27, d_0 = 0.5 mm.

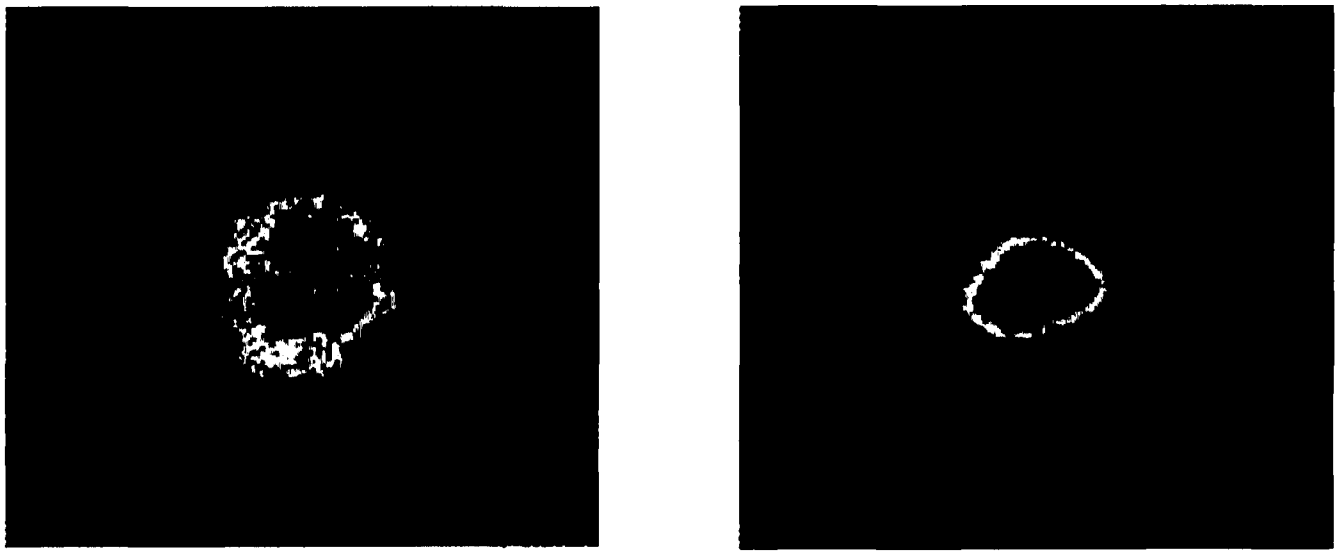

(a) (b)

Fig 6.11: Femtosecond laser beam profiles a and b before and after spatial filtering, respectively. The spatial filter consists of two identical convex lenses of 40 cm focal lens and 100 μm copper pinhole. The beam profile is recorded using a spricon beam profiler with a Cohu 6415 CCD camera and neutral density filters. Beam diameter at $1/e^2$ = 8 mm, energy density = 0.22 J/cm^2, λ = 400 nm, pulse width = 160 fs, and repetition rate = 1 kHz. The spatial filtering was performed in the atmospheric air pressure.

beam before and after being subjected to a spatial filter. A well-defined, clean Gaussian profile with no hot spots was obtained with a filter of 100 μm pinhole. The technique has a major drawback as with very fast damage occurring to the pinhole.

An alternative cleaning-up technique was done by subjecting the beam to a 10X expander, then selecting a homogeneous intensity area as an input beam for micromachining. The output of expansion cleaning-up technique gave rise to a flattop profile, as shown in Fig. 6.12. Although the two cleaning-up techniques greatly improved the beam intensity profile and, consequently, the micromachined samples' quality, the laser output power was greatly reduced.

6.5 SINGLE PULSE ABLATION

The single-pulse ablation experiment was performed for two objectives. The first was to study the surface morphology change after the ablation process, and secondly, was to investigate the possible formation nano-structure self-assembled material. Figures 6.13-a, b illustrate the optical micrographs of single-pulse ablation of Si and GaP, respectively, at various laser energy densities. At an energy density 20 times the ablation threshold, silicon showed exploded molten droplets and wires far from ablation central spot by tens of microns away from the ablated zone. At this energy density level, detailed features corresponded with the ablation process, such that laser induced ripples and self-assembled filaments could not be seen. Decreasing the energy density to about 10 times the ablation threshold only decreased the kinetic and the amount of the spilled material. Nevertheless, the above-mentioned ablation-related features could not be seen. However, long-period ripples by the outer ring of the exposed area were seen at those two laser

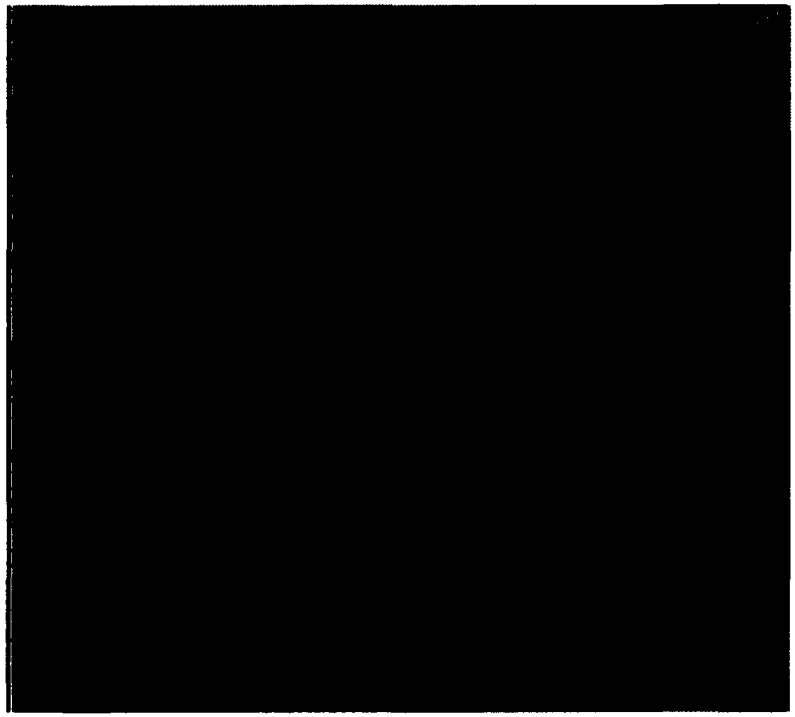

Fig 6.12: Femtosecond laser beam profile after subjected to a 10X beam expander then selecting a top hut profile area using a diaphragm. The beam profile is recorded using a spricon beam profiler with a Cohu 6415 CCD camera and neutral density filters. Beam diameter at $1/e^2 = 8$ mm, energy density = 0.22 J/cm^2, $\lambda = 400$ nm, pulse width = 160 fs, repetition rate = 1 kHz.

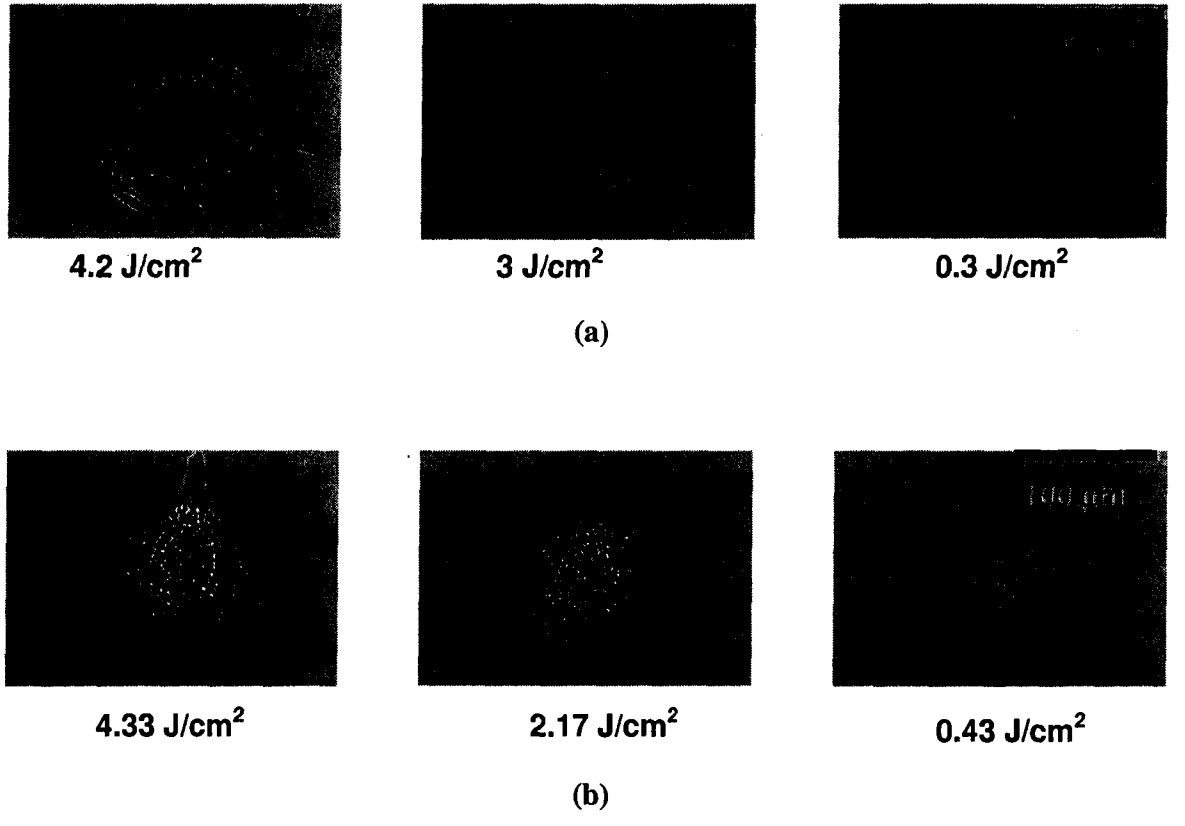

Fig 6.13: (a, b) Optical micrographs of single-femtosecond laser pulse ablation of Si and GaP, respectively, at various laser energy densities.

energy densities. In case of silicon sample, solidified ejected material was observed with sizes ranged from few tens of nanometers up to few tens of micrometers. In the case of the gallium phosphate, the molten material was confined inside the ablation zone. No resolidified ejected material was observed in this case. Very clear concentric contours were observed around the center of the ablation area. The observed counters drew well-defined boundaries for ablation, crystallization, and oxidation processes.

The exploded material observed at laser energy density of about 4.2 J/cm^2 in case of silicon suggested that the surface layer was saturated with the incoming photons then overheated and then a sequence of phase explosion, normal boiling including inhomogeneous nucleation of bubbles took place in the remaining melted layer. The picture is not far away in the case of gallium phosphate, however, the sharp ablation threshold associated with the nonlinear process seams to put clear boundaries between the different physical processes, which occur simultaneously in the concentric area of the focus spot.

6.6 NANOSCALE SELF-ASSEMBLED SURFACE STRUCTURES OF SILICON

Large varieties of ordered structures are reliably exhibited at different wavelengths and pulse durations from CW to femtoseconds. According to their shape and dimensions, these structures can be roughly divided into three groups. The first group of structures (ripples) results from the interference between the incident radiation and the wave scattered by the surface. The period and orientation of the reciprocal grating vector relative to the light polarization corresponds well to the interference character of the excitation field [85-88]. The second group (2-D cellular structures with 5-15 μm

diameters) was found in [89], which seems to occur due to the instability of capillary waves as a result of thermal–capillary effects in a laser-melted film [90]. Same type of ripples was observed in our case shown in Fig. 6.14-a. Finally, the third group, first obtained in [91] using single picosecond pulse excitation of silicon, is comprised of a structure consisting of a large number of partly intertwined filaments with diameters of approximately 120 *nm*. Recently these results [91] were reproduced on dielectric BaF_2 using multi-shot femtosecond excitation [92]. The distinguished feature of these structures is that they do not obey theoretical predictions in parts concerning the period of structures, the shape of ordering, and structure orientation relative to electromagnetic vector of laser pulse. The mechanism causing formation of nano-scale filament structures is still far from being understood and the phenomenon requires further experimental study. That calls the necessity of thorough experimental studies of the phenomenon described. In this Dissertation, detailed description was given for an ordered filament structure obtained by irradiating a silicon surface with a single femtosecond pulse. It is also found that the resulting 200 *nm* filament structure contains a substructure with periods as small as 60 *nm*.

The experiment was conducted with utilization of femtosecond laser system with specification previously described in chapter 5 along with a mode-locked YAG:Nd^{3+} oscillator with an amplifier that provided a 27 *ps* laser pulse with energy of 7 mJ at a wavelength of 1060 *nm*. The resulting images are shown in Fig. 6.14 and were obtained using an energy range of approximately from 2.5 to 3.5 J/cm^2. Outside of this energy range, no filament structures were observed.

A number of salient features in the nano-scale filament structure are clearly seen

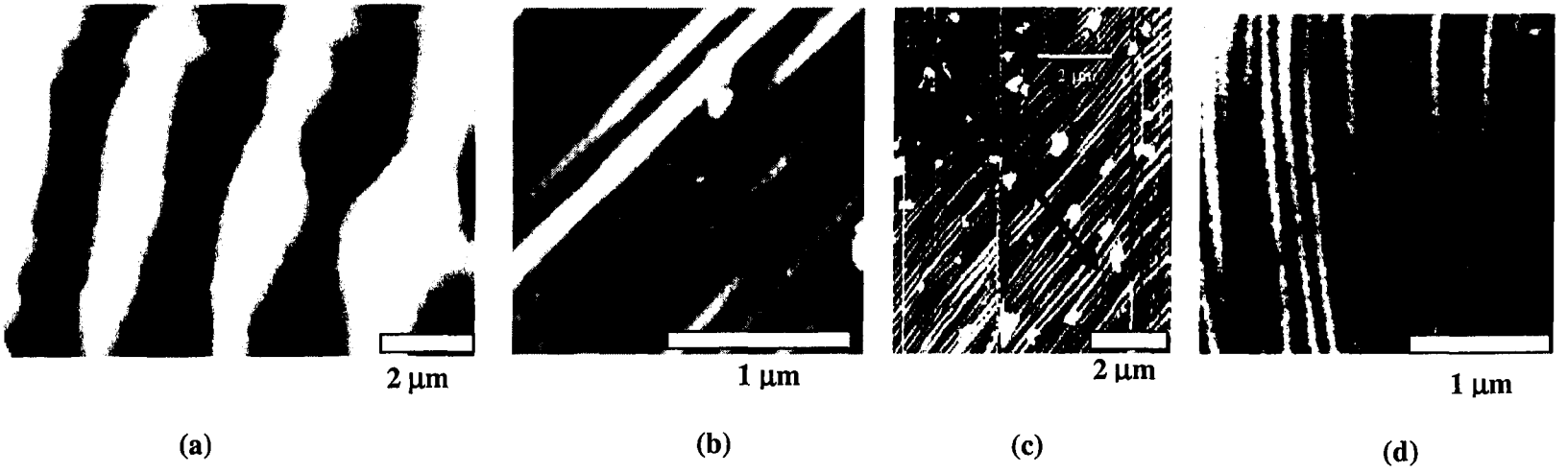

Fig 6.14: AFM micrograph (a) of a single shot ablation on silicon. Energy density = 0.75 J/cm^2. The large ripples have periods along the perpendicular to the laser polarization orientation. The AFM (b, c) and SEM (d) are images of silicon filament structures. Filament in (b, and c) under exposure condition: single pulse, pulse width = 110 fs, λ = 800 nm, energy density ~ 3 J/cm^2. The arrow in (c) shows the direction to ablation zone center. Filaments in (d) obtained under exposure condition: single pulse, pulse width = 27 ps, λ = 1064 nm, energy density 3 J/cm^2. Filaments widths obtained in (b, c) are ~λ/8; while in (d) are ~ λ/10.

in Fig. 6.14. Four key observations were made.

1) The filament structure is localized to an area surrounding the ablation zone. The filaments are predominantly oriented along the circumference. It was found that filament diameters became smaller the further they were from the center of ablation zone. The average ratio between the wavelengths applied (0.8 and 1.06 μm) and the filament diameter was found to be 1: (4 or 8).

2) No dependence was found between filament orientation and the polarization state of the irradiance (linear/circular).

3) The intertwinement of the separate filaments can be seen in Fig. 6.14 b, c, d where filaments can be seen both entering and exiting the structure.

4) An ultrafine surface substructure with a period and amplitude of 60 *nm* and 10 *nm*, respectively, was observed between the filaments. The scanned surface profile (height as a function of spatial coordinate) of the substructure received along the line between two filaments is shown in Fig. 6.15.

It should be noted that the mechanism for the creation of ripple and the mechanism for the creation of filament structures seem to be quite different. The ripple structure results from spatial periodical modulation of the pump field due to interference between the incident and scattered waves [88]. Under these circumstances, the interference pattern is directly printed on the surface of the solid. The filament structure in Fig. 6.14 can not be explained by interference phenomenon because both the period (less than the wavelength by a factor 4 (for λ = 800 *nm*) or 8 (for λ = 1060 *nm*)) and the orientation (mostly along the circumference of the ablated area) contradict what would be expected from interference theory. To a certain extent, one can apply the theory of

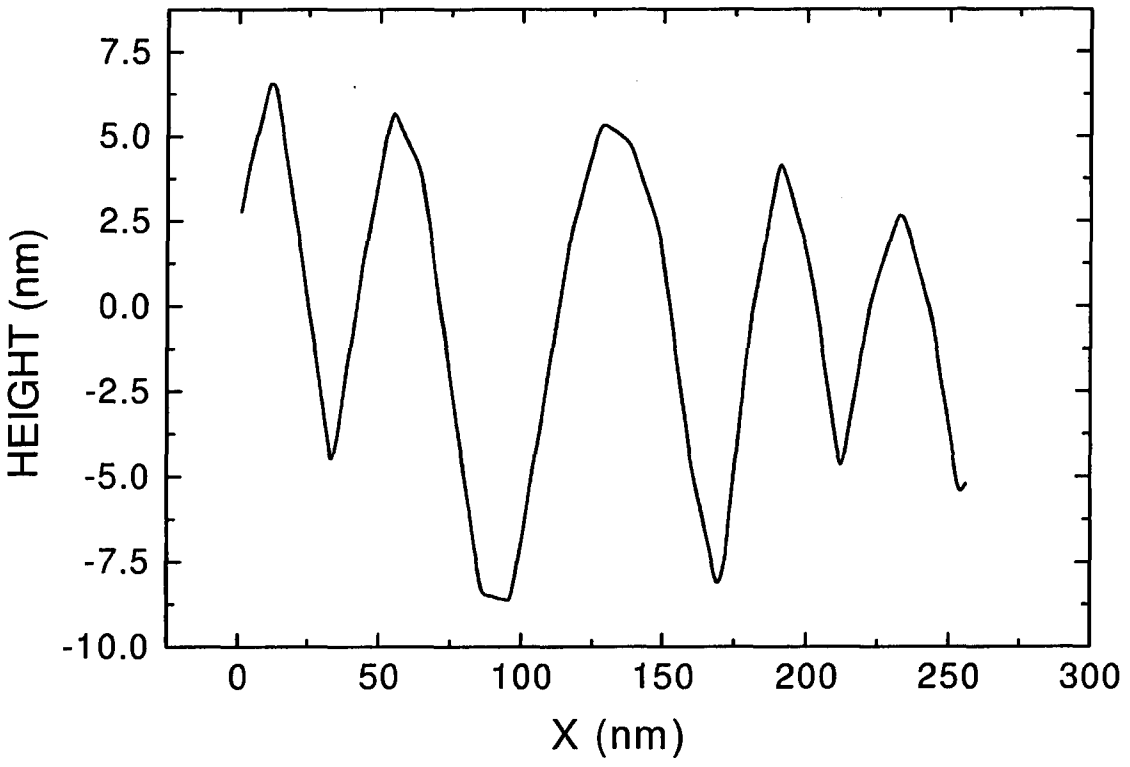

Fig 6.15: The profile of the substructure in fig 6.10-c. Data was plotted using micro lab origin software after being transferred from AFM associated data file. The line scan is along the interconnection between the filaments.

capillary wave instability that results from positive feedback between capillary waves and the pump field [93]. This theory holds that excitation with positive feedback can result in a continuum of dominant structures with wave vectors q, which satisfy the inequality $k_0 << q \leq k_0 m$ or $\lambda / m \leq d << \lambda$ (where k_0 is a light wave vector, q is a wave vector of the periodical structure, m is the extinction coefficient, and λ is the laser wavelength). Using optical constants for liquid silicon $n = 4$, $m = 6$ ($\lambda = 800$ *nm*) and $n = 5$, $m = 7$ ($\lambda = 1060$ *nm*) [94], one can find the lower limit of the continuum of dominant filament structures, which is equal to 133 and 151 *nm*, respectively. The values that result correspond reasonably with the experimental data (200 and 120 *nm*). The theory of instability [93] is based on the interaction of the light field with capillary waves of the melted phase of a solid. This means that melting has to take place within the duration of the exciting laser pulse. It first appears that there is no possibility for melting during a 120 *fs* laser pulse since experiments [74] have found that a delay time of about 700 *fs* is necessary for melting to occur at a fluence of 0.4 J/cm^2. On the other hand, ultrafast lattice rearrangements that occur at the semiconductor to metal phase transition in VO_2 were found to be as fast as 75 *fs* [95]. Assuming that the delay time shown in [74] depends on the fluence, one can theorize that at fluence ten times more than the melting threshold, melting can take place at least near the end of a 120 *fs* exciting laser pulse. If so, capillary wave instability may, in part, explain the results of our experiments. In addition to capillary wave instability, another possible mechanism that may be present during the interaction is spatial perturbation in the high density electron-hole plasma where concentrations can reach 10^{21} cm^{-3} during femtosecond excitation. As for the ultrafine 60 *nm* periodical substructure seen in Fig. 6.14 -c, we have been unable to

determine the mechanism responsible for the creation of such a substructure when irradiated with single femtosecond pulse excitation. At the present time, it is still unknown if there is an interconnection between filament structure (200 *nm*) and substructure (60 *nm*). Further study is required to clarify the processes involved in femtosecond laser ablation of semiconductors. The fine structure had periods of about 60 *nm*. The nano-tube's self-assembled structure, along with the small periods of fine structure, are shown in Fig. 6.14-b and c. The self-assembled nano-structure was also observed with a picosecond laser pulse, as shown in Figs. 6.14-d. and 6.15 shows the spatial distribution of the nanometer's fine structure. The structures illustrated in Fig. 6.14-b and c were only observed with the silicon target and showed no evidence of their existence in the case of gallium phosphate target.

6.7 MULTIPLE PULSES ABLATION

An experiment was performed to investigate the effect of the multiple-pulse exposure using a cylindrical lens at an energy density about three times the ablation threshold. Figures 6.16 and 6.17 illustrated ESM photographs of silicon and gallium phosphate targets, respectively, after being irradiated with a variable number of pulses ranging between 2 and 1000 pulses. For the silicon case, the first photograph showed an ablated surface with a resolidified molten material attached to it. Not much change was observed in the ablated area by increasing the number of pulses up to 100 pulses with the exception that the ablated area was getting wider. Starting from 200 pulses and up, a well-organized periodical structure with a period less than 10 μm was observed and pronounced the increase of the number of pulses. The periodical structure consisted of

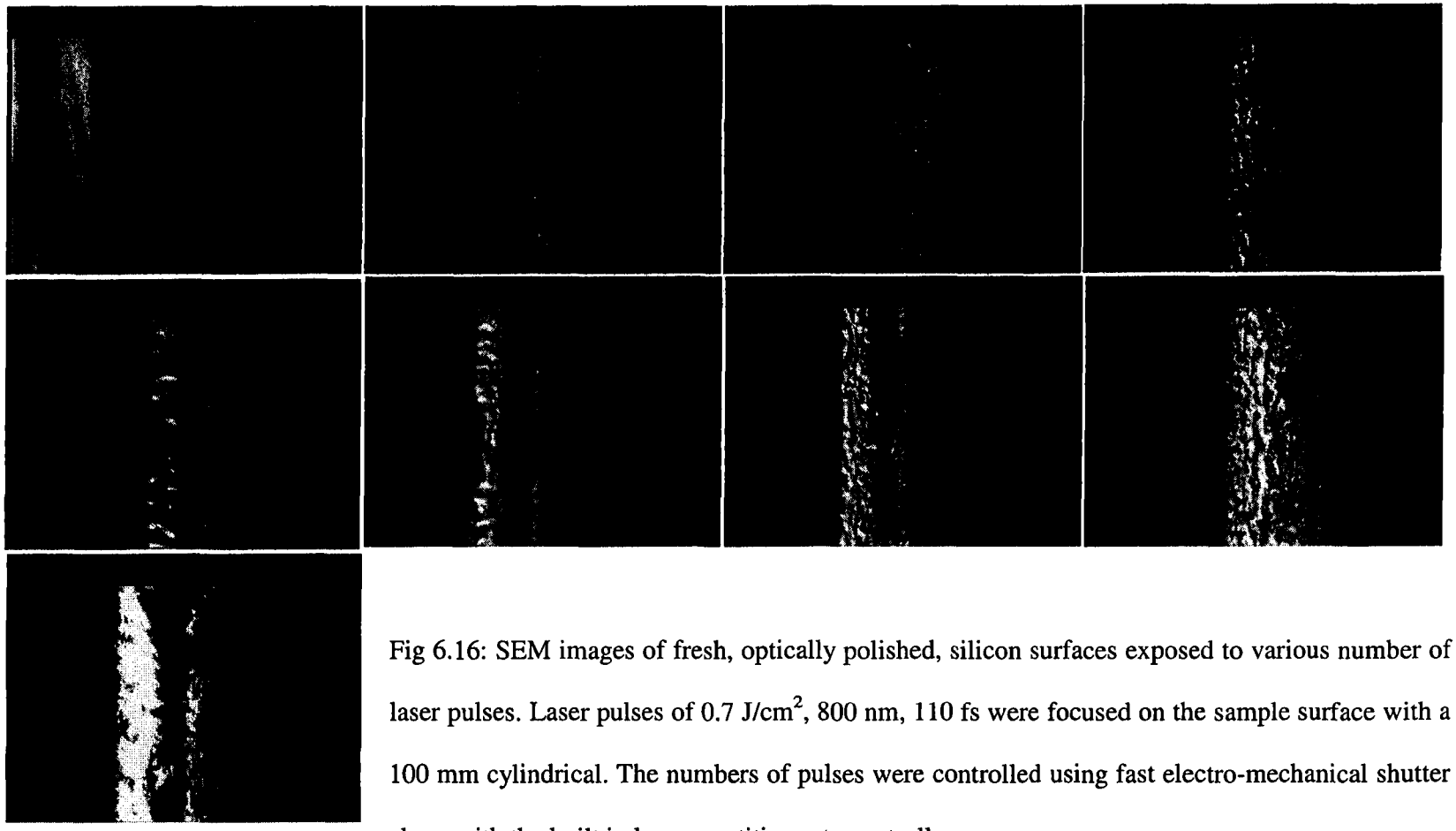

Fig 6.16: SEM images of fresh, optically polished, silicon surfaces exposed to various number of laser pulses. Laser pulses of 0.7 J/cm^2, 800 nm, 110 fs were focused on the sample surface with a 100 mm cylindrical. The numbers of pulses were controlled using fast electro-mechanical shutter along with the built in laser repetition rate controller.

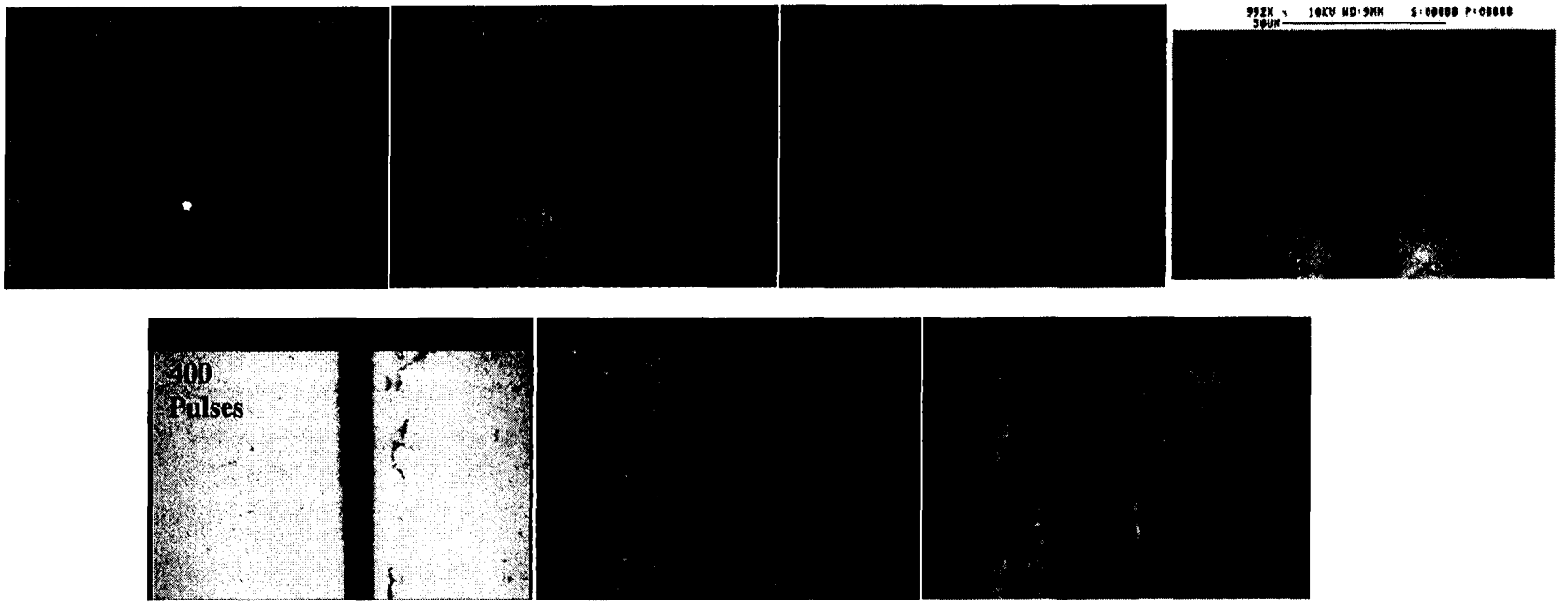

Fig 6.17: SEM images of fresh, optically polished, gallium phosphate surfaces exposed to various number of laser pulses. Laser pulses of 0.7 J/cm^2, 800 nm, 110 fs were focused on the sample surface with a 100 mm cylindrical. The numbers of pulses were controlled using fast electro-mechanical shutter along with the built in laser repetition rate controller.

ablated spots in the bottom of the irradiated area. The ablated spots started with sizes of a few tens of nanometers, reaching to few micrometers with the increase of the number of pulses. A similar response of gallium phosphate was obtained, except that the periodical structure appeared within certain window irradiating pulses (200-400) and then disappeared. The structures were more defined with accurate periods in the case of gallium phosphate than in the case of silicon. The sharp ablation threshold of the non-linear process in the case of gallium phosphate is assigned responsible for the cleaner structure obtained, however, the theory of formation of such well-organized pattern still unknown and needs more experimental investigation order to be fully characterized.

6.8 SILICON MICROMACHINING

6.8.1 EFFECT OF LASER MICROMACHINING POWER

Micromachined line width as a function of laser power was also studied. The sample surface was irradiated with different laser powers. Figure 6.18 shows the variation of line width as a function of laser power. The result could be considered in two regions. The first region was from ~ 0.18 J/cm^2 to 0.4 J/cm^2 energy densities with a micromachined line width ranging from 500 nm to ~ 4 μm. The second region was from 0.2 to 0.4 J/cm^2 to 2 J/cm^2. As shown in Fig. 6.18, in the first region of the curve, micromachining occurred only at the center of the focus spot where the energy density slightly exceeded the material's ablation threshold. This explains why line width increased rapidly with respect to laser power. In the second region of the curve, the corresponding line width increased less rapidly with respect to laser power than what occurred in the first region. This is because within this power range, the micromachined

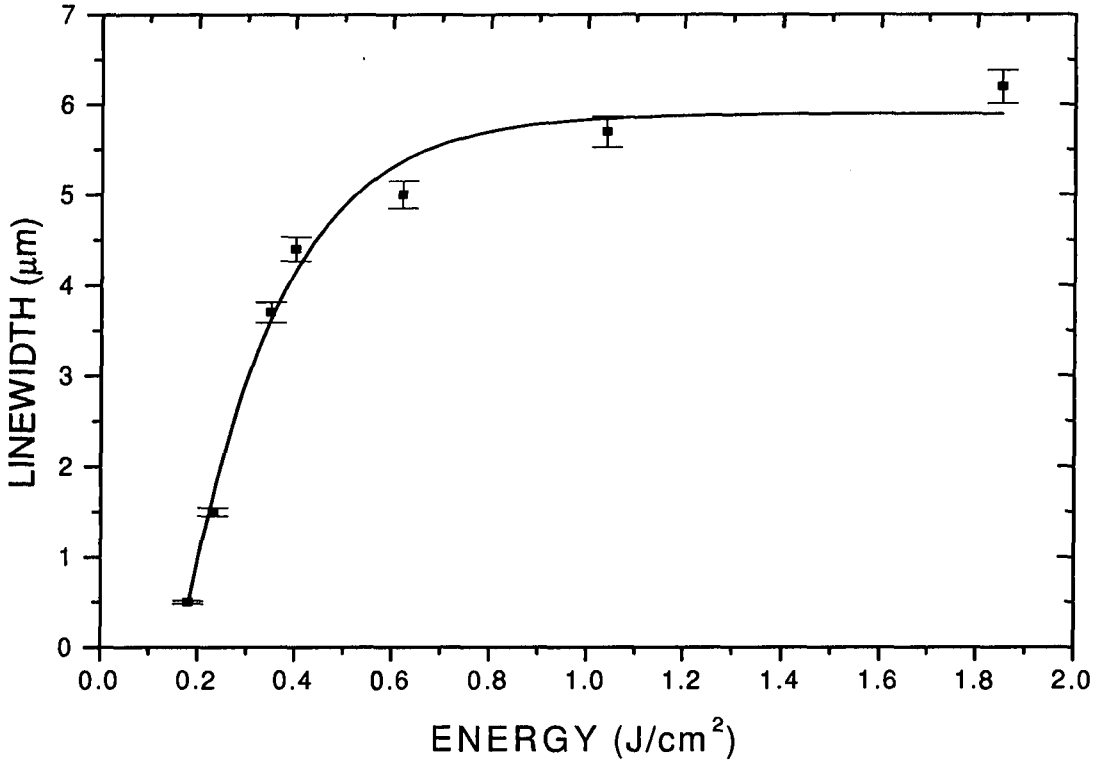

Fig 6.18: Ablated line width of optically polished silicon surface as a function of the laser energy density. The solid squares are the experimental data while the solid line is sigmodial fit. The laser was focused with an objective lens of 0.65 numerical aperture, while the sample was moved at 100 μm/sec using a stage of 1 μm accuracy and 10nm resolution. λ=400 nm, repetition rate = 1 kHz. The line widths were measured with 500 X optical microscope.

area approached the size of the focus spot. Operating at the material's ablation threshold value appeared to produce the smallest line width; however, discontinuous lines may have resulted from fluctuations in laser power. An experimental solution would be to work with powers slightly above the ablation threshold (i.e., in the range of 0.18 - 0.3 J/cm^2) to ensure continuous submicron line widths.

6.8.2 EFFECT OF GAS ENVIRONMENT ON MACHINING QUALITY

Two identical samples were micromachined: one in air at atmospheric pressure and the other in flowing helium gas at a pressure of 20 Torr in a chamber. At low laser power (< 500 nJ), the surface quality did not improve when micromachined under helium assist gas (see Fig. 6.19).

Chen et. al. [65] reported an improvement in machining quality when a shield gas was introduced to the experiment. However, their machining experiment was done under energy density of several J/cm^2. It is expected that by using shield gas in the micromachining application, material oxidation should go down, cooling rate should go up, and the plasma formation along with air breakdown should be minimized. However, in a power regime less than $2J/cm^2$, no significant difference between machining samples in atmospheric air pressure and pressured noble gas such as He. The reason is that for high power laser pulses, the incident energy is enough to create air breakdown that plays a major role in distort the pulse spatial profile.

6.8.3 EFFECT OF POLARIZATION

Laser pulses of 130 nJ were used to micromachine two sets of identical samples at

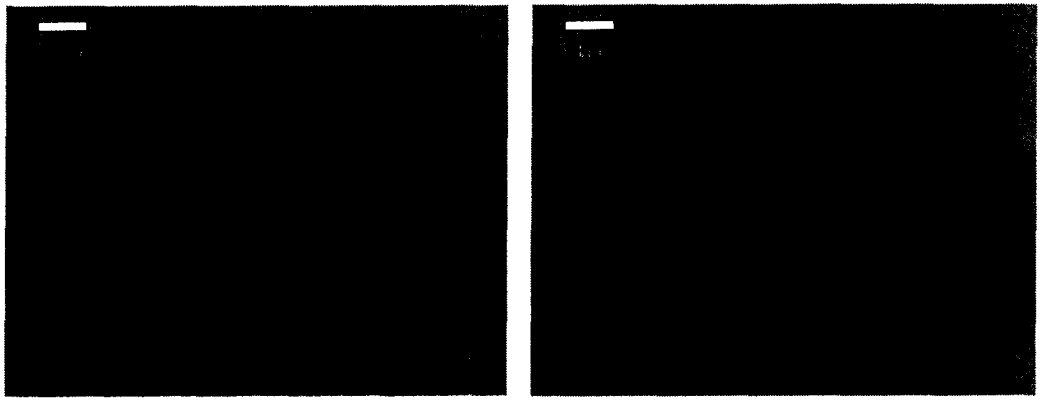

(a) (b)

Fig. 6.19: An optical microscope photograph of micromachined samples (a) in air at atmospheric pressure and (b) under 20 torr of He as an assist gas. Micromachining parameters: λ = 400 nm, pulse width = 160 fs, energy density = 0.22 J/cm^2, repetition rate = 1 kHz, and scan speed = 100 μm/sec.

the same focus position at a calculated spot size of 0.75 μm (Spot size = 1.22 λ /NA where λ is the wave length and NA is the numerical aperture). The first set was micromachined with a laser beam polarization parallel to the sample scan direction while the other sample was micromachined with a laser beam of polarization orientation perpendicular to the sample scan direction. Samples micromachined with a parallel polarization direction had lines 700 *nm* wide and 600 *nm* deep, while samples micromachined with a perpendicular polarization direction had lines 1.5μm wide and 130 *nm* deep. Parallel polarization machined samples produced smooth lines with minimal recast layers on the edges while the perpendicular polarization machined samples gave shallow, irregular floors, as shown in Fig. 6.20 and 6.21.

The optical diffraction efficiency for the 1-D micromachined samples was measured. The parallel polarization micromachined samples had 15% higher efficiency when tested with perpendicular laser polarization to the structure lines than that when tested with parallel laser polarization. No significant difference in diffraction efficiency of the perpendicular polarization machined samples as a function of incident He-Ne laser polarization orientation was observed.

The difference in the ablated line width was due to the variation in optical absorption between the two polarization orientations. The absorption was higher for the parallel polarization direction, twice as much than for the perpendicular direction [13]. Parallel polarization produced smoother, deeper ablated lines (0.7 *μm* wide and 600 *nm* deep), while perpendicular polarization resulted in higher reflection over the edges, producing lines that were shallower and wider (1.5 *μm* wide and 200 *nm* deep). At a 1 kHz laser frequency, 100 μm /sec scan speed and a calculated focus spot size of 0.75 μm,

Fig 6.20: AFM photograph of 700 *nm* wide and 600 *nm* deep micromachined lines. . Laser polarization orientation was parallel to the laser scan direction. λ = 400 nm, pulse width = 160 fs, energy density = 0.22 J/cm^2, repetition rate = 1 kHz, scan speed = 100 μm/sec.

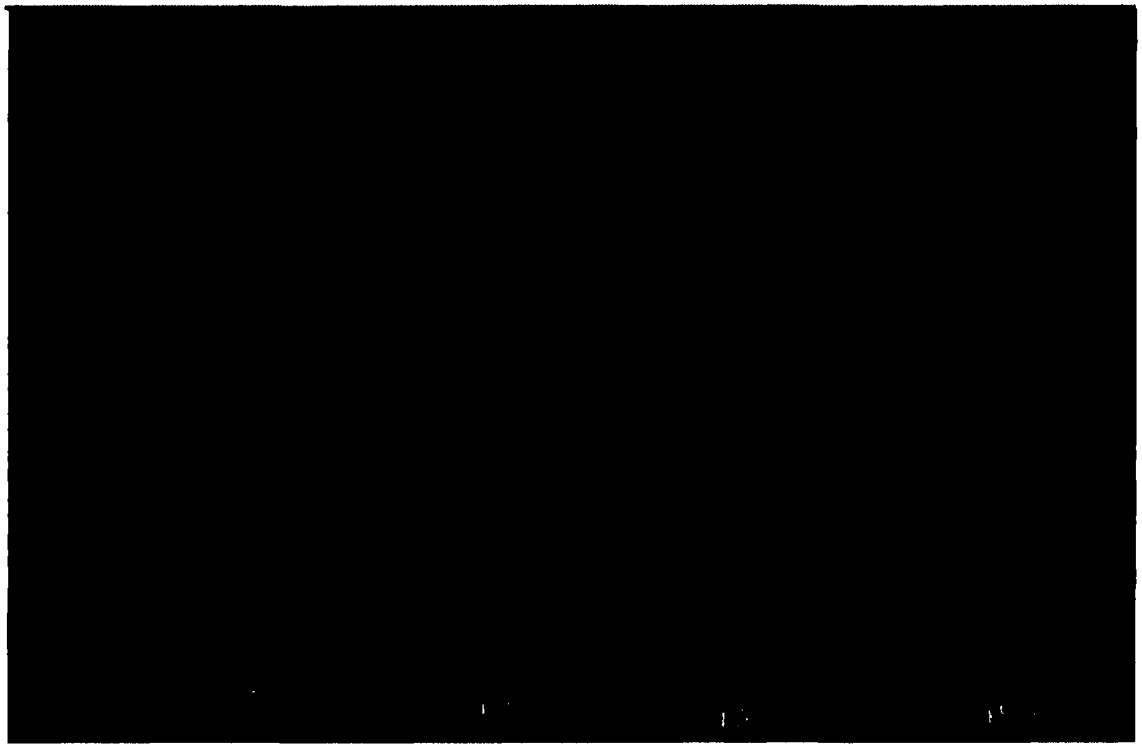

Fig. 6.21: AFM photograph of 1.5 *μm* wide x 200 *nm* deep micromachined lines. Laser polarization orientation was perpendicular to the laser scan direction. λ = 400 nm, pulse width = 160 fs, energy density = 0.22 J/cm^2, repetition rate = 1 kHz, scan speed 100 μm/sec.

about 8 pulses were needed in order to have a complete overlapping over the focus spot area. The first pulse ablated a thin surface layer in the order of a few nanometers for perpendicular polarization to few tens of nanometers for parallel polarization. In the case of the perpendicular polarizations, the proceeding pulses impended on the morphology changes of the surface without a longer perpendicular incident angle. This decreased the light coupling and increased the reflection over the edges. The increase in the reflection resulted in a widening of the ablated lines. On the other hand, with a parallel polarization pulse train, a flat ablated floor existed, keeping the incident angle at normal incident.

6.8.4 1-D AND 2-D PERIODICAL STRUCTURE FABRICATION

Using an optimal focus position and 0.26 J/cm^2 energy density, two sets of samples with lines parallel and perpendicular to the incident polarization orientation were micromachined. A 1-D periodical structure was micromachined with a period of 5 μm. A 2-D periodical structure was produced by micromachining the sample in one direction and then again in the perpendicular direction. We examined the 2-D pattern structure using AFM and results are shown in Fig. 6.22. The diffraction characteristics were examined using a linearly polarized 632 *nm* He-Ne laser. For 1-D periodical structures, the parallel polarization direction-micromachined sample produced a 1-D diffraction pattern, while the perpendicular polarization-micromachined sample produced a 2-D diffraction pattern of discreet orders. The diffraction pattern obtained in all micromachined samples satisfied the following equation:

$$\theta_{mn} = tan^{-1}\left[\lambda \sqrt{\frac{m^2}{d_1^2 - m^2\lambda^2} + \frac{n^2}{d_2^2 - n^2\lambda^2}}\right] \qquad (6.14)$$

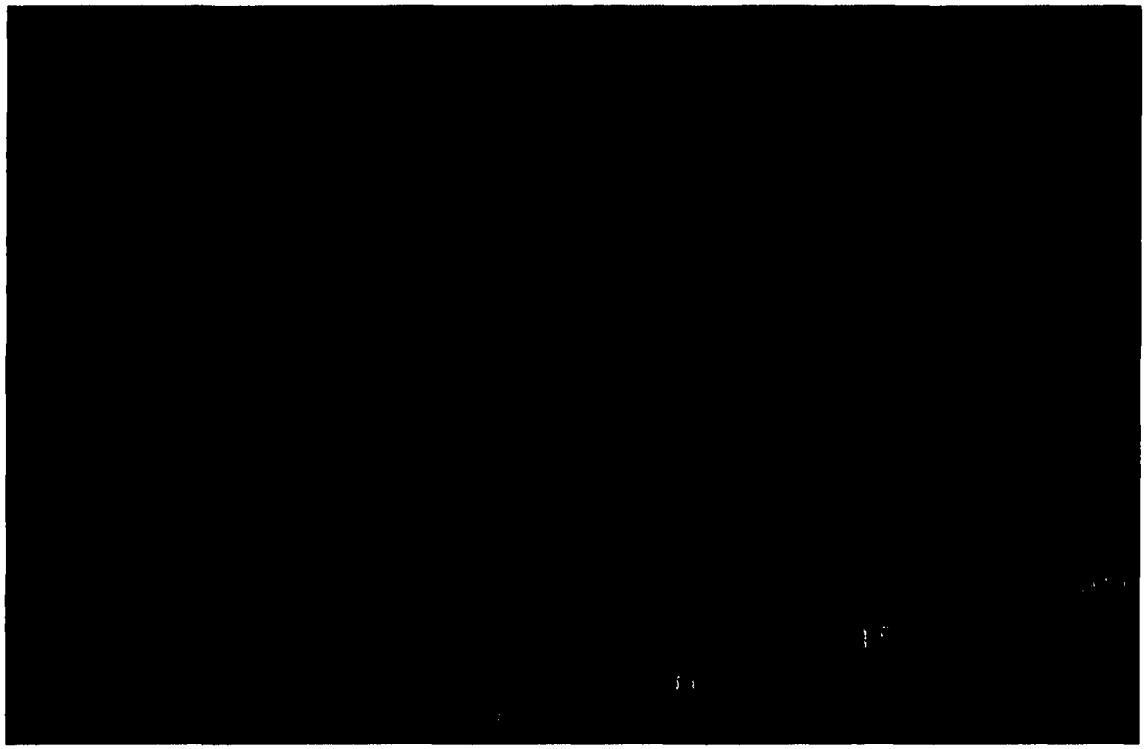

Fig. 6.22: AFM photograph of a micromachined 2-D Micromachined periodical structure. λ = 400 nm, pulse width = 160 fs, energy density = 0.22 J/cm^2, repletion rate = 1 kHz, scan speed = 100 μm/sec. Sample was first scanned in one direction (parallel to the incident polarization orientation), then scanned in the perpendicular direction (perpendicular to the incident polarization).

where λ is the He-Ne wavelength, θ_{mn} is the diffraction angle, m and n are the diffraction orders, (m, n =0, ±1, ±2, ±3, ...) and d_1 and d_2 are the periods of the structure. The equation was satisfied for diffraction pattern formation of the 2-D periodical structure and, with $d_2 = 0$ and $n = 0$, was also satisfied for 1-D periodical structures.

Figures 6.23 through 6.25 show the observed diffraction patterns for 1-D (Polarization parallel and perpendicular to scan direction) and 2-D micromachined samples.

6.8.5 EFFECT OF LASER POWER ON OBSERVED DIFFRACTION PATTERN

At a laser energy density that ranged from 0.22 J/cm^2 to 1.2 J/cm^2, we micromachined periodical structures with periods of 5 μm. The laser polarization orientation was perpendicular to scan direction. The relationship between the laser power used for micromachining and the intensity of the observed 2-D diffraction pattern was studied. Figure 6.26 presented diffraction patterns of micromachined samples at different laser powers after etching with HF for 1 minute to remove re-solidified molten material. 2-D diffraction patterns from the samples micromachined with a laser energy density between 0.22 J/cm^2 and 0.6 J/cm^2 for polarization perpendicular to scan direction were observed. At 1.2 J/cm^2, the 2D patterns disappear and only 1D diffraction patterns are visible.

AFM micrograph of 2D machined sample showed a superimposed grating vertical to the machined lines, as illustrated in Fig. 6.27-a and b. The period of the superimposed grating was in the order of 5 μm. AFM micrograph showed a smoothed machined line floor at energy density higher than 3 times of the ablation threshold (see Fig. 6.28).

Fig. 6.23: Diffraction pattern obtained from a 5μm periodical structure machined in a parallel direction to the laser polarization. The sample was micromachined at same micromachining parameters of the sample illustrated in Fig 6.20. The diffraction characteristics were tested using a linearly polarized He-Ne laser of 1 mW @632 nm.

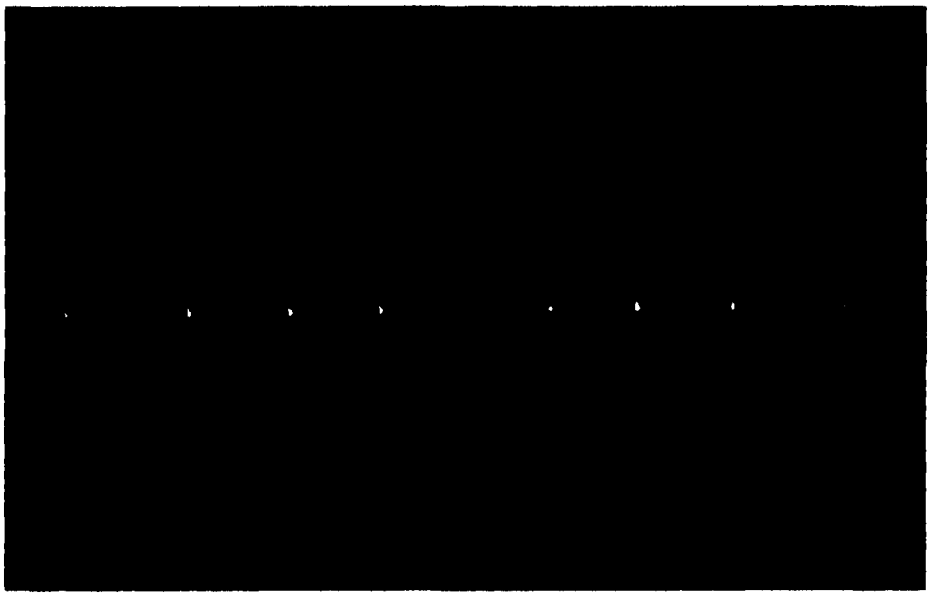

Fig. 6.24: Diffraction pattern obtained from a 5μm periodical structure machined in a perpendicular direction to the laser polarization orientation. The sample was micromachined at same micromachining parameters of the sample that illustrated in Fig 6.21. The diffraction characteristics were tested using a linearly polarized He-Ne laser of 1 mW @632 nm.

Fig 6.25: Diffraction pattern obtained from a 2D 5x5 μm periodical structure. The sample was micromachined at same micromachining parameters of the sample that illustrated in Fig 6.22. The diffraction characteristics were tested using a linearly polarized He-Ne laser of 1 mW @632 nm.

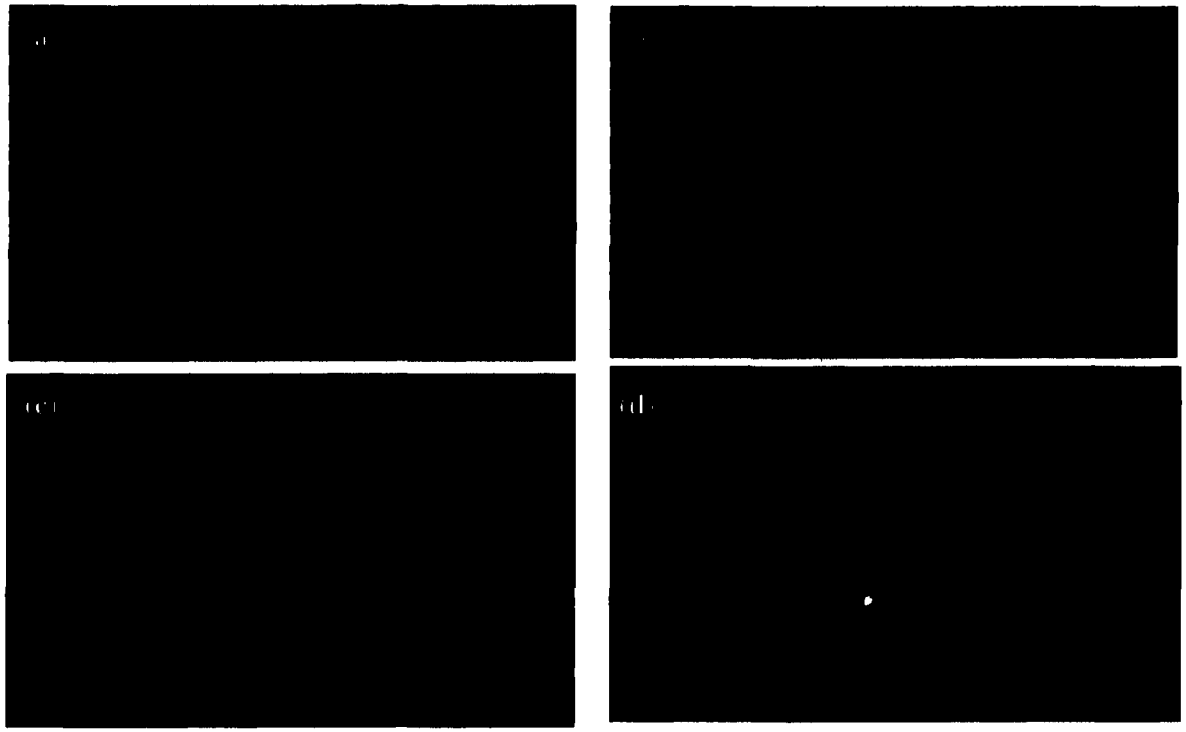

Fig. 6.26: Effect of laser power on the diffraction properties of the micromachined grating. The micromachining direction was perpendicular to the laser polarization orientation. Laser machining energy densities were a) 0.3 b) 0.44 c) 0.6 and d) 1.2 J/cm^2, λ = 400 nm, repetition rate = 1 kHz, scan speed = 100 μm/sec. The diffraction characteristics were tested using a linearly polarized He-Ne laser of 1 mW @ 632 nm.

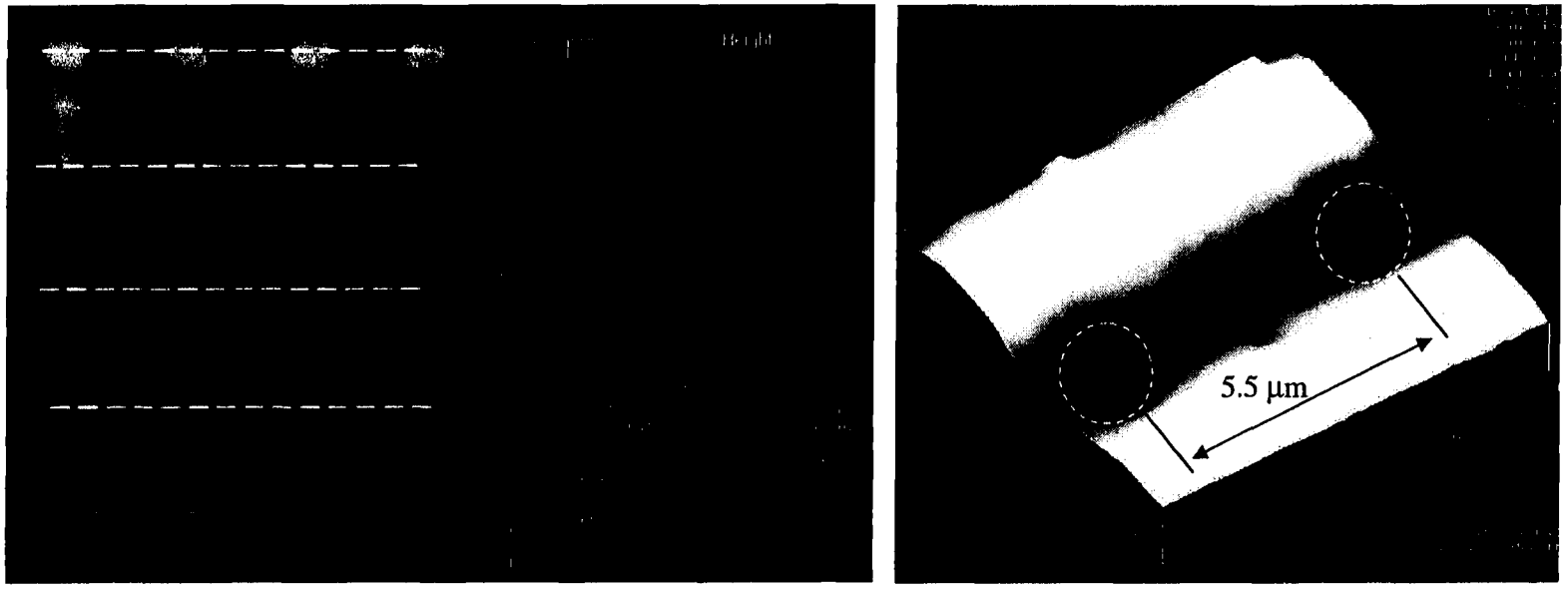

(a) (b)

Fig. 6.27: a, b are low and high magnification AFM photographs of 1-D micromachined silicon sample under the following micromachining parameters: perpendicular laser scan direction to the incident laser polarization orientation, λ = 400 nm, energy density = 0.3 J/cm^2, repetition rate = 1 kHz, scan speed = 100 μm/sec (The sample presented in fig 6.27-a). The graphs show two super-imposed gratings in the order of 5 μm.

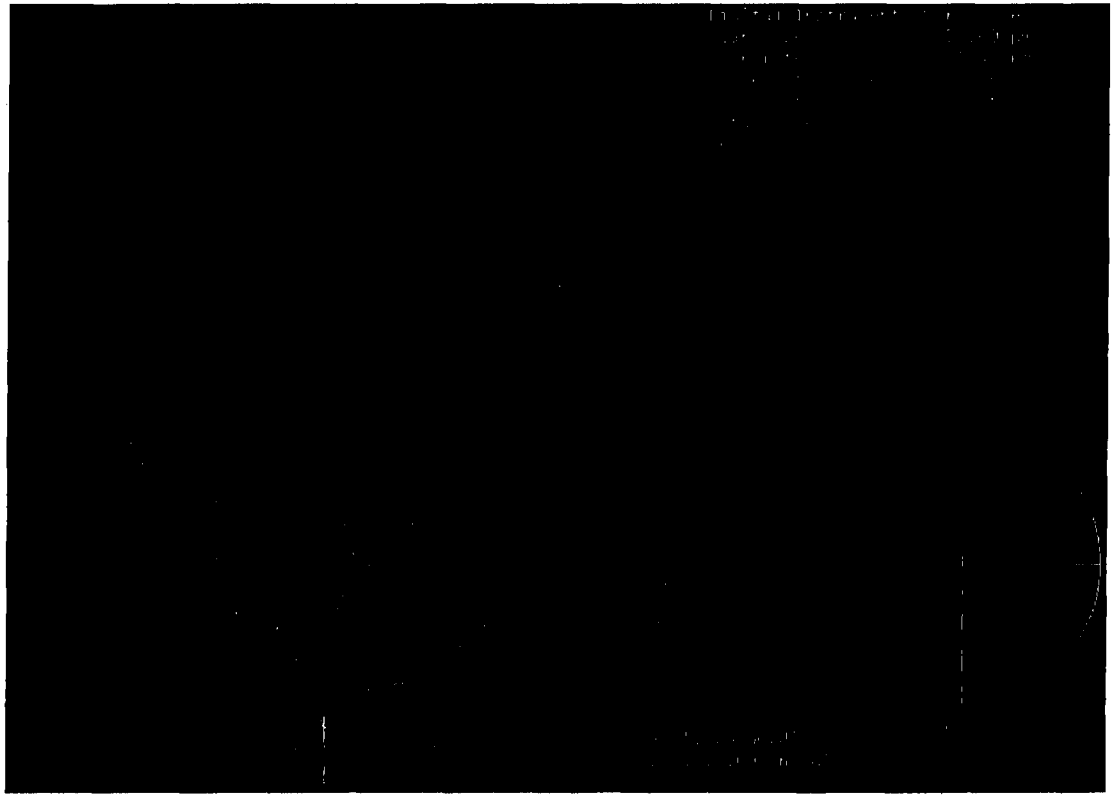

Fig. 6.28: AFM photographs of a smoothed machined grating bottom as a result of increasing the laser energy density to 1 J/cm^2, λ = 400 nm, repetition rate = 1 kHz, and scan speed = 100 μm/sec. Laser scan direction was perpendicular to the laser polarization orientation.

The 2-D diffraction patterns were a result of secondary superimposed periodical ripples having period along the polarization direction. During parallel writing direction, these ripples were smoothed out, but in perpendicular direction, they remained and gave rise to 2-D diffraction patterns. These ripples had large periods (3-5 μm in our case) and were perpendicular to the small periodical that had been reported in past literature.

Figure. 6.14-a shows, the formation of small and large ripples on the silicon surface when polarization direction was from bottom to top. These ripples were obtained as a result of single-pulse exposure using laser energy density ~ 0.75 J/cm^2; however, for consecutive pulses, increasing the laser energy density beyond 0.6 J/cm^2 smoothed the floor of the machined lines and consequently the 2-D diffraction patterns disappeared.

6.8.6 EFFECT OF MICROMACHINING SCHEME ON DIFFRACTION PROPERTIES

Two sets of samples were micromachined with polarization parallel to scan direction and the laser energy density of 0.26 J/cm^2. Two different scanning schemes were used and the samples were optically characterized. Figure 6.29 shows the scanning schemes and the corresponding diffraction patterns. The scanning of the sample in one direction produced a diffraction pattern that satisfied the 1-D grating equation. Scanning of the sample in alternative direction produced extra diffraction orders with lower intensities between the original diffraction orders.

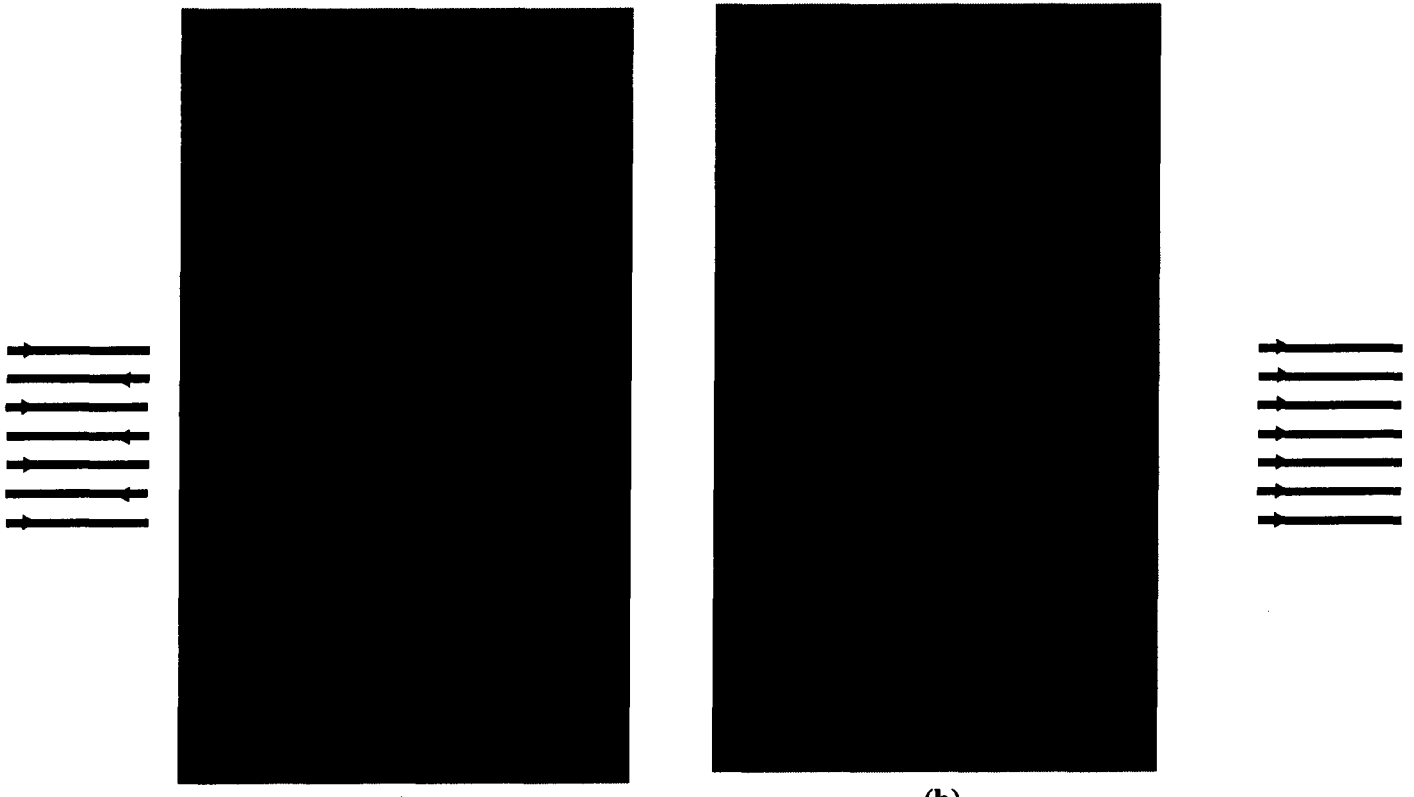

Fig. 6.29: Micromachining schemes and the corresponding diffraction pattern.

(a) Laser scanning along one direction. (b) Laser scanning with alternate direction.

λ = 400 nm, energy density = 0.22 J/cm^2, repetition rate = 1 kHz, scan speed = 100 μm/sec. Diffraction characteristics are tested using a linearly polarized He-Ne laser of 1 mW @ 632 nm.

CHAPTER 7

CONCLUSIONS

The presented work in this Dissertation contributes to the field of femtosecond laser interaction with semiconductors in general and to the field of laser micromachining of micro-electro-mechanical systems in particular. The understanding of the basic laser interaction process in single and multi-pulse modes would benefit the general understanding of ultrashort pulse laser interaction with semiconductors. That understanding would also help in achieving the best utilization of the unique characteristics of the femtosecond. New nano-scale features were observed for the first time with single-pulse ablations of silicon. Self-organized periodical structures with periods ranging from a few nano- to micron-sized periods were observed for the first time with the multiple-pulse exposure.

The two indirect materials that were selected to conduct the investigations in this Dissertation represented two excitation modes: namely, single and two-photon excitation. The interactions of single-pulse lasers with silicon and gallium phosphate were studied using a novel self-imaging technique. The material properties were studied during and after the interaction. The two-photon absorption process was investigated and the coefficient of absorption was determined. The temporal development of the interaction process was studied by applying a classical pump and probe technique. The obtained information from the previously mentioned experiments was utilized while running more detailed process characterizations experiments for MEMS fabrication. The material statuses during the interaction of single-pulse interaction with silicon and gallium

phosphate were investigated. The observed increase of the reflectivity in both cases could be assigned to the high electronic excitation of the materials. This high-density electron-hole pair generation might contribute to the destabilization of the material covalent bonds and consequently to structural change of the material. The results confirmed the previously reported structural instability during the interaction of single femtosecond pulse with semiconductors. However, the presented results in this Dissertation dealt with a much higher energy density regime [24, 29, 32]. The fitting of the experimental results defined Drude damping time to be in the order of 0.35 fs for Si and 0.27 fs for GaP.

The sharp ablation threshold of the non-linear process in case of gallium phosphate makes it a good candidate for practical applications such as femtosecond direct intensity detectors.

The two-photon absorption coefficient was determined from the numerical fitting of Fig. 6.5. The used optical arrangement provided a higher signal to noise ratio of the recorded data in addition to the sharp femtosecond ablation threshold. It was therefore possible to clear the doubt about the exact value of β [78].

Pump and probe measurements showed the temporal behavior of the two-photon absorption process. The probe pulse measured no changes in the optical properties of the material when the pump pulse was in the early energy deposition stages. When time passed and the pump pulse started depositing a considerable amount of energy, the non-linear process took place and absorption increased. The maximum absorption took place at the highest pulse energy. The pulse energy started to decrease after reaching the maximum point and the probability of the non-linear process became lower. The surface

plasma took place after ending the pulse. The free carriers' absorption was assigned to be responsible for the difference in the transmission values before and after the laser pulse.

The beam profile clean up had a big impact on the quality, accuracy, and repeatability of the micromachining process. The disadvantage of the process was the big loss in laser power due to the pinhole filtering in the first case and a small area selection in the second case. It is very reasonable for future work to investigate a filtering technique with a cooling system. This would help in extending the pinhole's lifetime. The other issue with the laser pulses was the contrast. The contrast of the laser pulses increased to 1:1000 after doubling the laser beam.

Self-assembled 200 *nm* filament structures were observed in experiments on picosecond and femtosecond single pulse ablation of silicon. For femtosecond pulse durations, a 60 *nm* periodical substructure was found in addition to a filament structure. It is shown that capillary wave instability resulting from positive feedback could explain, in part, the main features of the filament structure. The mechanism that creates the fine substructure is unknown at this time.

A multiple-pulse ablation process was investigated to serve in understanding the nature of the micromachining process. The use of 100 mm cylindrical lens in this experiment was initially to confirm the results obtained with the laser scanning experiment with high-pulse overlapping (~85%). Second, the experiment enabled a large exposure area that could easily show the formed structure in a long-range order (few millimeters). A well-organized periodical structure was observed as a function of the number of pulses in cases of silicon and gallium phosphate. The periodical structure started at a threshold number of pulses (200 pulses in our case). In the case of the silicon,

the periodical structure could still seen up to 1000 pulses, while it disappeared in the case of the gallium phosphate after 400 pulses. Due to the dissimilar excitation mechanism in silicon (one-photon) than in gallium phosphate (two-photon), the structural formation with the latter had a sharper threshold and was consequently cleaner and more sensitive to the incident number of pulses. It also exhibited more precise periods in the order of 5 μm. The periods were getting smaller with the increase of the number of shots. The theory behind this structural formation is still unknown and needs more experimental work in order to be fully characterized.

The micromachining parameters were optimized for 0.7 and 1.5 μm wide lines using polarization orientations that were parallel and perpendicular to the laser scanning direction. Operating slightly above the ablation threshold allowed us to control line width and to increase resolution.

Running the experiment at low power in a He gas environment did not improve the micromachining quality but gave results similar to that obtained in an air environment. Operating at low laser energy density $< 2J/cm^2$ minimized the plasma formation in air and the corresponding damage to the sample surface. This finding does not contradict with the reported improvement of the machining quality in [65] as a result of machining under He gas environment because their experiment was performed at much higher laser power.

The ablated line width and quality of the periodical structure was found to be a function of laser polarization orientation with respect to laser scanning direction. The difference in the ablated line width was due to the variation in optical absorption between the two polarization orientations. The absorption was higher for the parallel polarization

direction twice as much than for the perpendicular direction [13]. Parallel polarization produced smoother, deeper ablated lines (0.7 μm wide and 600 nm deep), while perpendicular polarization resulted in higher reflection over the edges, producing lines that were shallower and wider (1.5 μm wide and 200 nm deep). At a 1 kHz laser frequency, 100 μm /sec scan speed and a calculated focus spot size of 0.75 μm, about 8 pulses were needed in order to have a complete overlapping over the focus spot area. The first pulse ablated a thin surface layer in the order of a few nanometers for perpendicular polarization to few tens of nanometers for parallel polarization. In the case of the perpendicular polarizations, the proceeding pulses impended on the morphology changes of the surface without a longer perpendicular incident angle. This decreased the light coupling and increased the reflection over the edges. The increase in the reflection resulted in a widening of the ablated lines. On the other hand, with a parallel polarization pulse train, a flat ablated floor existed, keeping the incident angle at normal incident.

The diffraction patterns of 1-D and 2-D micromachined samples were found to be functions of the micromachining laser energy density and polarization orientations. 1-D diffraction patterns were obtained from parallel-machined samples, while 2-D diffraction patterns were obtained from a perpendicular machined sample at laser energy density < 0.6 J/cm^2. The 2-D diffraction patterns were a result of secondary periodical ripples having period along the polarization direction. During parallel writing direction, these ripples were smoothed out, but in perpendicular direction, they remained and gave rise to 2-D diffraction patterns. These ripples had large periods (3-5 μm in our case) and were perpendicular to the small periodical that had been reported in past literature. As Fig. 6.10-a shows, the formation of small and large ripples on the silicon surface when

polarization direction was from bottom to top. These ripples were obtained as a result of single-pulse exposure using laser energy density ~ 0.75 J/cm^2.

For consecutive pulses, increasing the laser energy density beyond 0.6 J/cm^2 smoothed the floor of the machined lines and consequently the 2-D diffraction patterns disappeared.

Different scanning schemes yielded different diffraction patterns. Scanning in only one direction produced periodical structures of identical engraved lines and a typical 1-D diffraction pattern was observed. The laser beam was affecting the material as a vector function that depended on the scanning direction. The alternative scan scheme produced two micromachined periodical structures with associated diffraction pattern of alternating intensities.

LITERATURE CITED

1. S. Preuss, A. Demchuk, and M. Stuke, "Subpicosecond uv laser ablation of metals," Appl. Phys. A, **61**, 1, 33-37, (1995).
2. P. Simon and J. Ihlemann, "Machining of submicron structures on metals and semiconductors by ultrashort UV-laser pulses," Appl. Phys. B, **63**, 5, 505-08, (1995).
3. T. Götz and M. Stuke, "Short-pulse UV laser ablation of solid and liquid metals: indium," Appl. Phys. A, **64**, 6, 539-43, (1997).
4. M. Feuerhake, J.H. Klein-Wiele, G. Marowsky, and P. Simon, "Dynamic ablation studies of submicron gratings on metals with sub-picosecond time resolution," Appl. Phys. A, **67**, 5, 603-06, (1998).
5. K. Furusawa, K. Takahashi, H. Kumagai, K. Midorikawa, and M. Obara, "Ablation characteristics of Au, Ag, and Cu metals using a femtosecond Ti: sapphire laser," Appl. Phys. A, **69**, 7, S359-66, (1999).
6. F. Korte, J. Koch, S. Nolte, C. Fallnich, A. Ostendorf, and B.N. Chichkov, "Nanostructuring of metal layers and transparent materials with femtosecond laser pulses," ICALEO, 14-17, Scottsdale, Arizona, Oct. (2002).
7. P. Mannion, J. Magee, E. Coyne, and G. O'Connor, "Ablation thresholds in ultrafast laser micro-machining of common metals in air," Proceedings of SPIE, **4876**, 470-78, (2003).
8. S. Küper and M. Stuke, "Ablation of polytetrafluoroethylene (Teflon) with femtosecond UV excimer laser pulses," Appl. Phys. Lett., **54**, 1, 4-6, (1989).

9. A. C. J. Glover, E.K. Illy and J. A. Piper, "High speed uv micromachining of polymers with frequency-doubled copper vapor lasers," IEEE J. Sel. Topics in Quantum Electron., **1**, 830-35, (1995).

10. S. Lazare, J. Lopez and F. Weisbuch, "High-aspect-ratio microdrilling in polymeric materials with KrF laser radiation," Appl. Phys. A, **69**, Suppl. S1-S6, (1999).

11. S. Baudach, J. Bonse, and W. Kautek, "Ablation experiments on polyimide with femtosecond laser pulses," Appl. Phys. A, **69**, 7, S395- 98, (1999).

12. G. Herbst, M. Steiner, G. Marowsky, and E. Matthias, "Ablation of Si and Ge using UV femtosecond laser pulses," Mater. Res. Soc. Symp. Proc, **397**, 69-74, (1996).

13. B. K. A .Ngoi, K. Venkatakrishnan, L.E.N. Lim and B. Tan, "Submicron Micromachining on Silicon Wafer Using Femtosecond Pulse Laser," J. Laser Applications, **13**, 1, 41-43, (2001).

14. J. Bonse, Sbaudach, J. Kruger, W Kautek, and M. Lenzer, "Femtosecond laser ablation of silicon-modification threshold and morphology," Appl. Phys. A, **74**, 19-25, (2002).

15. M. Elbandrawy and M. Gupta, "Femtosecond Laser Micromachining of Silicon for MEMS," Proceedings of SPIE, **4977**, 219-25, (2003).

16. J. A. Neev, L. D. Silva, M. D Feit, M. D. Perry, A. M. Rubenchik and B. C. Stuart, "Ultrashort pulse lasers for hard tissue ablation," IEEE J. Sel. Topics in Quantum Electron., **2**, 4, 790-800, (1996).

17. K. Chen, J. Ihlemann, P. Simon, I. Baumann, and W. Sohler, "Generation of submicron surface gratings on LiNbO3 by ultrashort uv laser pulses," Appl. Phys. A, **65**, 4-5, 517-18, (1997).

18. K. Kawamura, T. Ogawa, N. Sarukura, M. Hirano, and H. Hosono, "Fabrication of surface relief gratings on transparent dielectric materials by two-beam holographic method using infrared femtosecond laser pulses," Appl. Phys. B, **71**, 1, 119-21, (2000).

19. G. Dumitru, V. Romano, H. P. Weber, M. Sentis, and W. Marine, "Femtosecond ablation of ultrahard materials," Appl. Phys. A, **74**, 6, 729-39, (2001).

20. J. F. Ready, "Effect of high power laser radiation," Academic, London, UK, (1971).

21. M. Von Allmen, "Laser drilling velocity in metals," J. Appl. Phys., **47**, 5460-63, (1976).

22. S. I. Anisimov and V. A. Khokhlov, "Instabilities in laser-matter interaction," CRC, Boca Raton, FL, (1995).

23. B. R. Finke, P. D. Kapadia, and J. M. Dowden, "A fundamental plasma based model for energy transfer in laser material processing," J. Phys. D: Appl. Phys., **23**, 643-54, (1990).

24. C. V. Shang, R. Yen, and C. Hirlimann, "Time resolved reflectivity measurements of femtosecond-optical-pulse-induced phase transition in silicon," Phy. Rev. Lett. **50**, 6, 454-57, (1983).

25. A. Miotello, and R. Kelly, "Critical assessment of thermal models for laser sputtering at high fluences," Appl. Phys. Lett., **67**, 24, 3535-37, (1995).

26. B. N. Chichov, C. Mouma, S. Notle, F. V. Alvensleben, and A. Tunnermann, "Femtosecond, picosecond and nanosecond laser ablation of solids," Appl. Phys. A, **63**, 109-15, (1996).

27. X. Liu, D. Du, and G. Mourou, "Laser ablation and micromachining with ultrashort laser pulses," IEEE J. Quantum Electron., **33**, 10, 1706-16, (1997).

28. S. S Wellershoff, J. Hohfeld, J Cudde, and E. Matthias, "The role of electron-phonon coupling in femtosecond laser damage of metals," Appl. Phys. A, **69** [Suppl.], S99-07, (1999).

29. D. von der Linde, K. Sokolowski-Tinten, and J. Bilkowski, "Laser-solid interaction in the femtosecond time regime," Appl. Surf. Sci, **109-10**, 1-10, (1997).

30. K. Sokolowski-Tinten, , J Bialkowsjki, M. Boing, A. Cavalleri, A. Oparin, J. meyer, S. I. Anisimo, and D. von der Linde, "Transient state of matter during short pulse laser ablation," Phys. Rev. Lett., **6**, 224-27, (1998).

31. K. Sokolowski-Tinten, J Bialkowsjki, M. Boing, A. Cavalleri, and D. von der Linde, "Thermal and non thermal melting of gallium arsenide after femtosecond laser excitation," Phys. Rev. B, **58**, 11805-08, (1998).

32. D. von der Linde and K. Sokolowski-Tinten, "The physical mechanism of short-pulse laser ablation," Appl. Surf. Sci, **154-155**, 1-10, (2000).

33. B. Rethfeld, A. Kaiser, M. vicanek, and G. Simon, "Ultrafast dynamics of nonequilibrium electrons in metals under femtosecond laser irradiation," Phys. Rev. B, **65**, 214303, (2002).

34. B. Rethfeld, V. V Temnov, K. Sokolowski-Tinten, P. Tsu, S. I Anstikov, M. B. Agrant, and D. von der Linde, "Superfast thermal melting of solids under the action of femtosecond laser pulses," J. Opt. Technol., **71**, 6, 348-52, (2004).

35. K. Hungson and J. Mazumder, "Numerical simulation of femtosecond laser interaction with silicon," J. Laser Applications, **17**, 2, 110-17, (2005).

36. R. Yen, J. M. Liu, H. Kurz and N. Bloembergen, "Space-time resolved reflectivity measurements of picosecond laser-pulse induced phase transitions in (111) silicon surface layers," Appl. Phys. Lett., **27**, 3, 153-60, (1982).

37. D. H. Auston, J. A. Golovchenko, P. R. Smith, C. M. Surko, and T. N. C. Venkatesan, "Cw argon laser annealing of ion-implanted silicon," Appl. Phys. Lett., **33**, 6, 539-41, (1979).

38. J. M. Liu, H. Kurz, and N. Bloembergen, "Picosecond time-resolved plasma and temperature-induced changes of reflectivity and transmission in silicon," Appl. Phys. Lett., **41**, 7, 643-46, (1982).

39. D. von der Linde and N. Fabricius, "Observation of an electronic plasma in picosecond laser annealing of silicon," Appl. Phys. Lett., **41**, 10, 991-93, (1982).

40. J. A. Van Vechten and R. Tsu, F. W. Saris, "Nonthermal pulsed laser annealing of Si; plasma annealing," Phys. Lett. A, **74**, 6, 422-26, (1979).

41. H. M. van Driel, "Kinetics of high-density plasmas generated in Si by 1.06- and 0.53-μm picosecond laser pulses," Phys. Rev. B, **35**, 8166–76, (1987).

42. J. A. Kash, J. C. Tsang, and J. M. Hvam, "Subpicosecond Time-Resolved Raman Spectroscopy of LO Phonons in GaAs," Phys. Rev. Lett., **54**, 2151–54, (1985).

43. P. Saeta, J. K. Wang, Y. Siegal, N. Bloembergen, and E. Mazur, "Ultrafast electronic disordering during femtosecond laser melting of GaAs," Phys. Rev. Lett., **67**, 1023–26, (1991).

44. N. Fabricius, P. Hermes, D. von der Linde, A. Pospieszozyk, and B. Stritzker, "Observation of Superheating During Picosecond Laser Melting," Solid State Communications, **58**, 4, 239-42, (1986).

45. N. Bloembergen, R. K. Chang, S. S. Jha, and C. H. Lee, "Optical Second-Harmonic Generation in Reflection from Media with Inversion Symmetry," Phys. Rev., **174**, 813–22, 1968.

46. H. W. K. Tom, G. D. Aumiller, and C. H. Brito-Cruz, "Time-resolved study of laser-induced disorder of Si surfaces," Phys. Rev. Lett., **60**, 1438–41, (1988).

47. P. Stampfli and K. H. Bennemann, "Dynamical theory of the laser-induced lattice instability of silicon," Phys. Rev. B, **46**, 10686–92, (1992).

48. P. Stampfli and K. H. Bennemann, "Time dependence of the laser-induced femtosecond lattice instability of Si and GaAs: Role of longitudinal optical distortions," Phys. Rev. B, **49**, 7299–05, (1994).

49. S. V. Govorkov, I. L. Shumay, W. Rudolph, and T. Schroder, "Time-resolved second-harmonic study of femtosecond laser-induced disordering of GaAs surfaces," Opt. Lett., **16**,13,1013-15, (1991).

50. K. Sokolowski-Tinten, H. Schulz, J. Bialkowski, and D. von der Linde, "Two distinct transitions in ultrafast solid-liquid phase transformations of GaAs," Appl. Phys. A, **53**, 3, 227-34, (1991).

51. K. Sokolowski-Tinten, J. Bialkowski, and D. von der Linde, "Ultrafast laser-induced order-disorder transitions in semiconductors," Phys. Rev. B, **51**, 14186–98, (1995).

52. P. L. Silvestrelli, A. Alavi, M. Parrinello, and D.00 Frenkel, "Ab initio Molecular Dynamics Simulation of Laser Melting of Silicon," Phys. Rev. Lett., **77**, 3149–52, (1996).

53. D. von der Linde and H. Schuler, "Breakdown and plasma formation in femtosecond laser-solid interaction," J. Opt. Soc. Am B, **13**, 1, 216-222, (1996).

54. K. Sokolowski-Tinten, J. Bialkowski, A. Cavalleri, D. von der Linde, A. Oparin, J. Meyer-ter-Vehn , and S. I. Anisimov, "Transient States of Matter during Short Pulse Laser Ablation," Phys. Rev. Lett., **81**, 224–27, (1998).

55. A. Cavalleri, K. Sokolowski-Tinten, J. Bialkowski, M. Schreiner, and D. von der Linde, "Femtosecond melting and ablation of semiconductors studied with time of flight mass spectroscopy," J. Appl. Phys., **85**, 6, 3301-09, (1999).

56. D. Perez and L. J. Lewis, "Ablation of solids under femtosecond laser pulses," Phys. Rev. Lett., **89**, 2555041-4, (2002).

57. W. T. Ashurst, and B. L. Holian, "Droplet formation by rapid expansion of a liquid," Phys. Rev. E, **59**, 6742–52, (1999).

58. B. Rethfeld, K. Sokolowski-Tinten, D. von der Linde, and S. I. Anisimov, "Ultrafast thermal melting of laser-excited solids by homogeneous nucleation," Phys. Rev. B, **65**, 092103-1-4, (2002).

59. C. Chao, C. Chen, C. Liu, Y. Chang and C.C. Yang, "Direct writing of silicon with high coherent ultraviolet laser," Appl. Phys. Lett., **71**, 2241-43, (1997).

60. B. K. A. Ngoi, K. Venkatakrishnan, E. N. L. Lim, B. Tan, and L. H. K. Koh, " Effect of energy above laser-induced damage threshold in the micromachining of silicon by femtosecond pulse laser," Optics and Lasers in Engineering, **35**, 361-69, (2001).

61. T. Her, R. J. Finalay, C. Wu, S. Deliwala and E. Mazur, " Microstructure of silicon with femtosecond laser pulses," Appl. Phys. Lett., **73**, 12, 1673-75, (1998).

62. D. Kapitan, D. W. Coutts, and C. E. Webb, "Efficient generation of near diffraction limited beam-quality output from medium scale copper vapor laser oscillator," J. Quantum Electron., **34**, 3, 419-26, (1998).

63. K. Venkatakrishnan, B Tan, L. H. K. Koh, and B. K. A. Ngoi, "Femtosecond pulsed laser ablation with spatial filtering," Optics and Lasers in Engineering, **38**, 425-32, (2002).

64. S. Juodkazis, H. Okuno, N. Kujime, S. Matsuo, and H. Misawa, "Hole drilling in stainless steel and silicon by femtosecond laser pulses at low pressure," Appl. Phys. A, **79**, 1555-1559, (2004).

65. H. Chien and M. C. Gupta "Pulse width effect in ultrafast laser processing of materials," Appl. Phys. A, **81**, 1257 (2005).

66. E. Coyne, J. P. Magee, P. Mnnion, G. M. O'connor, and T. J. Glynn, "STEM (scanning transmission electron microscopy) analysis of femtosecond laser pulse induced damage to bulk silicon," Appl. Phys. A, **81**, 371-378, (2005).

67. M. von Allmen and A. Blatter, "Laser-Beam Interactions with Materials: Physical Principles and Applications" 2nd ed. Springer, NewYork, (1995).

68. W. Z. Lin, R. W. Schoenlein, J.G. Fujimoto, E. P. Ippen, "Femtosecond absorption saturation studies of hot carriers in GaAs and AlGaAs," IEEE J. Quantum Electron., **24**, 2, 267–75, (1988).

69. C. V. Shank, R. L. Fork, R. F. Leheny and J. Shah, "Initial thermalization of photo excited carriers in GaAs studied by femtosecond luminescence spectroscopy," Phys. Rev. Lett., **66**, 1757–60, (1991).

70. M. L. Cohen and J. R. Chelikowski, "Electronic structure and optical properties of semiconductors," Springer, Berlin, (1989).

71. L. Oudar, D. Hulin, A. Migus, A. Antonetti, and F. Alexandre, "Subpicosecond spectral hole burning due to non-thermalized photo excited carriers in GaAs," Phys. Rev. Lett., **55**, 2074–77, (1985).

72. J. Shah, R. F. Leheny, and C. Lin, "Dynamic Burstein shift in GaAs," Solid State Communications, **18**, 8, 1035-37, (1976).

73. P. A. Wolff, "Theory of the band structure of very degenerate semiconductors," Phys. Rev., **126**, 405–12, (1962).

74. K. Sokolowiski-Tinten and D. von der Linde, "Generation of dense electron-hole plasmas in silicon," Phys. Rev. B, **61**, 4, 2643-50, (2000).

75. R. A. Abraham, G. N. Childs, and P. A. Sanderson, "Band gap narrowing due to many-body effects in silicon and gallium arsenide," J. Phys. C, **17**, 6105-25, (1984).

76. A. Oschlies, R. W. Godby, and R. J. Needs, "First-principles self-energy calculations of carrier-induced band-gap narrowing in silicon," Phys. Rev. B, **45**, 13741–44, (1992).

77. D. H. Reitze, T. R. Zhang, W. M. Wood, and M. C. Downer, "Two-photon spectroscopy of silicon using femtosecond pulses at above-gap frequencies," J. Opt. Soc. Am. B, **7**, 84-89,(1990).

78. D. Hulin, M. Combescot, J. Bok, A. Migus, J. Y. Vinet, and A. Antonetti, "Energy transfer during silicon irradiation by femtosecond laser pulse," Phys. Rev. Lett., **52**, 22, 1998-2001, (1984).

79. J. H. Bechtel and W. L. Smith, "Two photon absorption in semiconductors with picosecond laser pulses," Phys. Rev. B, **13**, 8, 3515-22, (1976).

80. K. Seeger, "Semiconductor Physics," Springer Verlag, Berlin; New York, (1991).

81. J. Marvin Weber, "Handbook of Optical Materials, Series: Laser & Optical Science & Technology," Vol. **19**, CRC press, (2002).

82. Yu. A. Goldbery, "Handbook Series on Semiconductor Parameters," Vol. **1**, M. Levinshtein, S. Rumyantsev and M. Shur, ed., World Scientific, London, (1996).

83. D. B. Laks, G. F. Neumark, A.Hangleiter and S. T. Pantelides, "Theory of interband auger recombination in n-type silicon," Phys. Rev. Lett., **61**, 10, 1229-32, (1988).

84. M. Combescot and J. Bok, "Electron-hole plasma generation and evolution in semiconductors," J. of Luminescence, **30**, 1-17, (1985).

85. H. M van Driel, J. E. Sipe, and J. F.Young, "Laser-induced periodic surface structure on solids: a universal phenomenon," Phys. Rev. Lett., **49**, 1955-58, (1982).

86. F. Keilmann, and Y. H. Bai, "Periodic surface structures frozen into CO_2 Laser-melted quartz," Appl. Phys. A, **29**, 9-18, (1982).

87. P. M. Fauchet, and A. E. Siegman, "Observations of Higher-order laser-induced surface ripples on (111) germanium," Appl. Phys. A, **32**, 135-40, (1983).

88. J. E. Sipe, J. F. Young, J. S. Preston, and H. M. van Driel, "Laser-induced periodic surface structure. I. Theory," Phys. Rev. B, **27**, 1141-54, (1983).

89. A. A. Bugayev, B. P. Zakharchenya, M. G. Ivanov, and I. A. Merkulov, "Cellular structure in the surface relief on silicon melted by a picosecond pulse," Pisma Zh. Tekh. Fiz., **12**, 46-48, (1986). [Sov. Tech. Phys. Lett., **12**, 91-92, (1986).]

90. A. A. Bugayev, V. A. Lukoshkin, V. A. Urpin, and D. G. Yakovlev, "Thermal-capillary effects and the formation of surface relief under picosecond laser pulses," Zh. Tekh. Piz., **58**, 908–14, (1988). [Sov. Phys. Tech. Phys., **33**, 550–53, (1988).]

91. A. A. Bugayev, B. P. Zakharchenya, and V. A Lukoshkin, "Generation of small-scale structural relief in a silicon surface by picosecond radiation pulses," Pisma Zh. Tekh. Fiz., **12**, 710-13, (1987). [Sov. Tech.Phys.Lett., **12**, 292-93, (1987).]

92. J Reif, F Costache, M Henyk, S Pandelov, "Ripples revisited: non-classical morphology at the bottom of femtosecond laser ablation craters in transparent dielectrics," Appl. Surface Science, **197-98**, 891-95, (2002).

93. S. A Akhmanov, V. I. Emel'yanov, N. I. Koroteev, and V. N. Seminogov, "Interaction of powerful laser radiation with the surfaces of semiconductors and metals: nonlinear optical effects and nonlinear optical diagnostics," Uspekhi Fizich. Nauk, **47**, 675-745, (1985). [Sov. Physics Uspekhi, **28**, 1084-153, (1985).]

94. S. K. F. Monika, "Optical properties of liquid silicon: the integral equation approach," J. Phys., Condens. Matter, **12**, 4341–51, (2000).

95. A Cavalleri, T Dekorsy, H Chong, J. C. Kieffer, and R. W. Schoenlein, "Evidence for a structurally-driven insulator-to-metal transition in VO_2: A view from the ultrafast timescale," Phys. Rev. B, **70**: 161102/1-161102/4, (2004).

VITA

for

Mohamed A. Elbandrawy

Education

Doctorate of philosophy

2006 Old Dominion University, Norfolk, VA, USA

Dissertation Title: *Femtosecond Laser Ablation with Single and Two-Photon Excitation for MEMS*

Department of Electrical and Computer Engineering, Applied Research Center.

Master of Science

1997 Cairo University, Giza, Egypt.

Dissertation Title Optimization of Carbon Dioxide Laser

Faculty of Science, Department of Physics, National Institute of

Laser Enhanced Science Laboratories.

Bachelors of Science

1991 Cairo University, Giza, Egypt.

Faculty of Science, Department of Physics.

Major: Physics.

Professional Experience

Old Dominion University, Applied Research Center, Newport News, VA, USA (1999-2006) Research assistant

- Studied self interaction of a single femtosecond pulse with Si and GaP.
- Achieved a submicron machined features and utilized the results in obtaining an OMEMS device.
- Studied and characterized laser micromachining of semiconductors and metal using ns, ps and fs lasers.
- Studied and characterized ns, ps and fs laser cutting, welding, texturing, and ablation of different materials.
- Assemble, optimize and maintain laser drilling setup for Siemens Automotive from scratch reaching to the mass production level. Introduce a novel technique to increase the cut quality of the orifice disks and to significantly reduce the machining time.
- Achieved excellent results in machining devices for industrial use.

Phillip Morris USA, New Technology Research Group, Richmond, VA, USA. (July-Oct. 2004) Internship

- Designed, assembled, characterized, and achieved a high-resolution absorption spectroscopic instrument.

Old Dominion University, Physical Electronics Research Institute,
(Feb 1998-May 1999) Research Assistant

- Achieved a high quality submicron drilled holes using ns laser for micro hollow cathode plasma jet.

National Institute of Laser Enhanced Science, Cairo University, Giza, Egypt. (1993-1998). Research Assistant

Publications

- Optical characteristics of femtosecond laser micromachining periodic structures, Applied Optics, Vol. 45, No. 27, 7137-43, 2006.
- Nanoscale self-assembled surface structures of silicon at femtosecond excitation, 2006. Accepted for publication in Journal of Laser Application.
- Effect of femtosecond laser beam reshaping on micromachining, 6th International Symposium on Laser Precision Microfabrication, Williamsburg, Virginia, 2005.
- Dynamics of laser hole drilling with nanosecond periodically pulsed laser, Optics and Lasers in Engineering, ISSN 0143-8166, 2005.
- Femtosecond laser micromachining of periodical structures, Mater. Res. Soc. Symp. Proc. 850, MM1.6.1-6, 2004.
- Copper vapor laser micromachining of 304 stainless steel, Journal of Laser Applications, 15, 2, 101-106, May 2003.
- Femtosecond Laser Micromachining of Silicon for MEMS, Proceedings of SPIE, Vol. 4977, pp 219-225, Jan 2003.
- Femtosecond laser micromachining of submicron features, SPIE, San José, California, 2003.
- Copper vapor micromachining of stainless Steel, ICLEO, Jacksonville, Florida, 2001.
- Fs laser micromachining of silicon, ICLEO, Jacksonville, Florida, 2001.
- Advanced Training Course on Laser Industrial Applications, May 27th –June 8th 2000, organized by Cairo University, Egypt, ICS (UNIDO) and TRIESTE, Italy.
- Optimization of Carbon Dioxide laser, International Laser Conference, NILES, Cairo University, 1997.

PUBLICATIONS AND ORAL PRESENTATIONS OUT OF THIS WORK

1. M. Elbandrawy, and M. C. Gupta, "Optical Characteristics of Femtosecond Laser Micromachining Periodic Structures," Applied Optics, **45**, No. 27, 7137-43, (2006).
2. M. Elbandrawy, and A. A. Bugayev, "Nanoscale Self-Assembled Surface Structures of Silicon at Femtosecond Excitation," Accepted for publication in J. Laser Application (2006).
3. M. Elbandrawy, "Effect of Femtosecond Laser Beam Reshaping on Micromachining," 6th International Symposium on Laser Precision Microfabrication, Williamsburg, Virginia, (Oral Presentation) (2005).
4. M. Elbandrawy, and M. C. Gupta, "Femtosecond Laser Micromachining of Periodical Structures," Mater. Res. Soc. Symp. Proc., **850**, MM1.6.1-6, (2004).
5. M. Elbandrawy, and M. C. Gupta, "Femtosecond Laser Micromachining of Silicon for MEMS," Proc. of SPIE, **4977**, 219-225, (2003).
6. M. Elbandrawy, "Femtosecond Laser Micromachining of Submicron Features," SPIE, San José, California, (Oral Presentation) (2003).
7. M. Elbandrawy, "Fs Laser Micromachining of Silicon," ICLEO, Jacksonville, Florida, (Oral Presentation) (2001).